

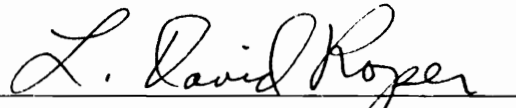
An Analysis of K^+ -Nucleon Scattering

by

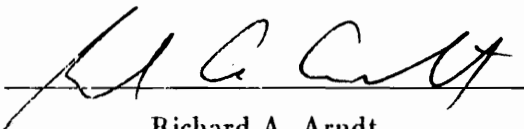
John S. Hyslop, III

Dissertation submitted to the Faculty of the
Virginia Polytechnic Institute and State University
in partial fulfillment of the requirements for the degree of
Doctor of Philosophy
in
Physics

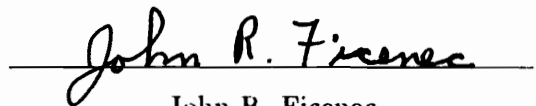
APPROVED:



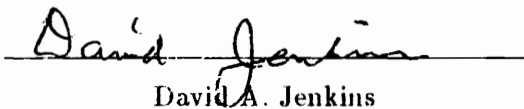
L. David Roper, Chairman



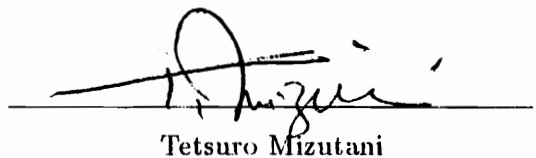
Richard A. Arndt



John R. Ficenec



David A. Jenkins



Tetsuro Mizutani

August, 1990

Blacksburg, Virginia

An Analysis of K^+ -Nucleon Scattering

by

John S. Hyslop, III

L. David Roper, Chairman

Physics

(ABSTRACT)

A partial-wave analysis of K^+ -nucleon scattering has been performed. Energy-dependent and energy-independent solutions for the isoscalar and isovector amplitudes are generated by fitting data with a chi-squared minimization technique. The isoscalar amplitudes extend to a K^+ incident lab kinetic energy of 1100 MeV; the isovector amplitudes extend to 2650 MeV. Due to the lack of a neutron target and scarcity of isoscalar data, K^+ -deuteron inelastic and elastic data are utilized in the analysis. The theories which incorporate the K^+ -deuteron data are fixed-scatterer, single-scattering impulse approximations.

Two different techniques are employed to find preliminary energy-dependent isoscalar solutions for the scattering amplitudes. The first technique involves initializing to two different single-energy solutions of previous studies. The second technique consists of utilizing the energy-dependent parametrization to fit successively larger bins of data, starting from zero energy, until the entire energy range is covered.

Two solutions result from these investigations since one of the solutions from the first technique agrees with the solution from the second technique. The partial-wave amplitudes are discussed. Resonance pole positions and scattering lengths are extracted from each solution and compared with predictions from theories and other analyses. Also, observables from each solution are compared and experiments are suggested to further refine the determination of the K^+N partial-wave amplitudes.

Acknowledgements

This doctorate is the culmination of the efforts of several. First of all, I thank Sam Bowen, currently of Argonne National Laboratories, for his assistance in studying for preliminary examinations. His review and comments on many problems greatly broadened my knowledge and interest in physics.

I also thank my major advisors, Dave Roper and Dick Arndt, for their guidance and patience in this doctoral research. Their continual support and role in the development of my research skills have been invaluable. I am grateful to Keiji Hashimoto for providing a detailed description of his K^+ -deuteron scattering theories and my examining committee for their comments on my dissertation.

My parents, John and Mary Blanche Hyslop, and aunt and uncle, Indie and Stanley Sheets, have always encouraged me to believe in my abilities. I will always be indebted to them.

Finally, I dedicate this dissertation to my loving wife, Margie, for her continual encouragement and support during this trying phase of our lives.

Contents

1	Introduction	1
1.1	Motivation	1
1.2	History	1
1.3	Structure of the Dissertation	3
2	Data Base	4
2.1	The K^+ -Nucleon Isoscalar Data Base	4
2.1.1	K^+d Breakup Reaction	5
2.1.2	K^+d Elastic Reaction	6
2.1.3	K_L^0 p Scattering	6
3	Two-Body Theory	13
3.1	Nuclear Amplitudes	13
3.2	Electromagnetic Effects	14

3.2.1	S-Matrix Product	14
3.2.2	Coulomb Barrier	15
3.3	Final Amplitudes	16
3.4	Observables	16
4	K^+d Theory	18
4.1	K^+d Breakup	18
4.1.1	Cutoffs on the Spectator Momentum	20
4.1.2	Scaling of Inelastic Form Factors	21
4.1.3	Electromagnetic Corrections	22
4.1.4	Cutoffs on Individual Experiments	22
4.2	K^+d Coherent Scattering	25
4.2.1	Electromagnetic Corrections	26
5	The Partial-Wave Analysis	34
5.1	χ^2 Determination	34
5.2	Energy-Dependent Parametrization	36
5.3	Energy-Independent Parametrization	39

6 The Solution	40
6.1 Isoscalar Solution	40
6.2 Combined Isoscalar and Isovector Solution	42
6.3 Resonances	45
6.4 Scattering Lengths	48
6.5 Comparison of observables from each solution	50
7 Conclusions and Recommendations	83
7.1 Conclusions	83
7.2 Recommendations	84
Bibliography	86
Vita	90

List of Figures

2-1	Data distribution for $\sigma(\theta)$ of $K^+d \rightarrow K^0pp$	10
2-2	Data distribution for $\sigma(\theta)$ of $K^+d \rightarrow K^+np$	10
2-3	Data distribution for $P(\theta)$ of $K^+n \rightarrow K^+n$	11
2-4	Data distribution for $P(\theta)$ of $K^+n \rightarrow K^0p$	11
2-5	Data distribution for $\sigma(\theta)$ of $K^+d \rightarrow K^+d$	12
2-6	Data distribution for $\sigma(\theta)$ of $K_L^0p \rightarrow K^+n$	12
4-1	K^+ deuteron breakup diagram.	28
4-2	Deuteron form factor for $K^+d \rightarrow K^0pp$ at an incident lab energy of 363 MeV.	29
4-3	Deuteron form factor for $K^+d \rightarrow K^0pp$ at an incident lab energy of 1085 MeV.	29
4-4	Deuteron form factor for $K^+d \rightarrow K^+np$ at an incident lab energy of 363 MeV.	30
4-5	Deuteron form factor for $K^+d \rightarrow K^+np$ at an incident lab energy of 1085 MeV.	30
4-6	Scaled $I_p(\theta)$ for $K^+d \rightarrow K^0pp$ at an incident lab energy of 363 MeV.	31

4-7	Breit frame dynamics.	32
4-8	Diagram for $K^+d \rightarrow K^+d$ scattering.	32
4-9	$K^+d \rightarrow K^+d$ form factors.	33
6-1	Initialization to Hashimoto's S_{01} single-energy solution and solution B versus T_{lab} . Triangles and diamonds represent the $\Re T$ and $\Im T$, respectively, of Hashimoto. The initialization is denoted by I and the B isoscalar solution is unmarked.	52
6-2	Initialization to Hashimoto's P_{01} single-energy solution and solution B versus T_{lab} . For further information, see the comments in the caption of Figure 6.1.	52
6-3	Initialization to Hashimoto's P_{03} single-energy solution and solution B versus T_{lab} . For further information, see the comments in the caption of Figure 6.1.	53
6-4	Initialization to Hashimoto's D_{03} single-energy solution and solution B versus T_{lab} . For further information, see the comments in the caption of Figure 6.1.	53
6-5	S_{01} T-matrix for solution A versus T_{lab}	54
6-6	P_{01} T-matrix for solution A versus T_{lab}	54
6-7	P_{03} T-matrix for solution A versus T_{lab}	55
6-8	D_{03} T-matrix for solution A versus T_{lab}	55
6-9	D_{05} T-matrix for solution A versus T_{lab}	56
6-10	F_{05} T-matrix for solution A versus T_{lab}	56
6-11	F_{07} T-matrix for solution A versus T_{lab}	57
6-12	G_{07} T-matrix for solution A versus T_{lab}	57

6-13	G_{09} T-matrix for solution A versus T_{lab} .	58
6-14	S_{01} T-matrix for solution C versus T_{lab} .	59
6-15	P_{01} T-matrix for solution C versus T_{lab} .	59
6-16	P_{03} T-matrix for solution C versus T_{lab} .	60
6-17	D_{03} T-matrix for solution C versus T_{lab} .	60
6-18	D_{05} T-matrix for solution C versus T_{lab} .	61
6-19	F_{05} T-matrix for solution C versus T_{lab} .	61
6-20	F_{07} T-matrix for solution C versus T_{lab} .	62
6-21	G_{07} T-matrix for solution C versus T_{lab} .	62
6-22	G_{09} T-matrix for solution C versus T_{lab} .	63
6-23	S_{11} T-matrix versus T_{lab} .	64
6-24	P_{11} T-matrix versus T_{lab} .	64
6-25	P_{13} T-matrix versus T_{lab} .	65
6-26	D_{13} T-matrix versus T_{lab} .	65
6-27	D_{15} T-matrix versus T_{lab} .	66
6-28	F_{15} T-matrix versus T_{lab} .	66
6-29	F_{17} T-matrix versus T_{lab} .	67
6-30	G_{17} T-matrix versus T_{lab} .	67
6-31	G_{19} T-matrix versus T_{lab} .	68

6-32 Argand diagrams of larger isoscalar partial-waves for solution A.	69
6-33 Argand diagrams of larger isovector partial-waves for solution A.	69
6-34 Argand diagrams of smaller isovector partial-waves for solution A.	70
6-35 Argand diagrams of larger isoscalar partial-waves for solution C.	70
6-36 Argand diagrams of larger isovector partial-waves for solution C.	71
6-37 Argand diagrams of smaller isovector partial-waves for solution C.	71
6-38 Isoscalar cross sections of solution A versus T_{lab}	72
6-39 Isovector cross sections of solution A versus T_{lab}	72
6-40 Isoscalar cross sections of solution C versus T_{lab}	73
6-41 Isovector cross sections of solution C versus T_{lab}	73
6-42 Complex plane contour plot of P_{01} for solution A versus W_{cm} . See Table 6.2 for the locations of poles and zeros in the complex plane.	74
6-43 Complex plane contour plot of D_{03} for solution A versus W_{cm} . The set of parallel lines indicates the branch cut. See Table 6.2 for the locations of poles and zeros in the complex plane.	74
6-44 Complex plane contour plot of P_{01} for solution C versus W_{cm} . See Table 6.2 for the locations of poles and zeros in the complex plane.	75
6-45 Complex plane contour plot of D_{03} for solution C versus W_{cm} . See Table 6.2 for the locations of poles and zeros in the complex plane.	75
6-46 Complex plane contour plot of P_{11} for solution C versus W_{cm} . See Table 6.2 for the locations of poles and zeros in the complex plane.	76

6-47	Complex plane contour plot of P_{13} for solution C versus W_{cm} . See Table 6.2 for the locations of poles and zeros in the complex plane.	76
6-48	Complex plane contour plot of D_{15} for solution C versus W_{cm} . See Table 6.2 for the locations of poles and zeros in the complex plane.	77
6-49	$\sigma(\theta)$ of $K^+n \rightarrow K^+n$ for solutions A and C. The solid line indicates $T_{lab} = 1000$ MeV; the longer dash in the dashed line indicates the higher energy. .	78
6-50	$P(\theta)$ of $K^+n \rightarrow K^+n$ for solutions A and C. The solid line indicates $T_{lab} = 1000$ MeV; the longer dash in the dashed line indicates the higher energy. .	78
6-51	$R(\theta)$ of $K^+n \rightarrow K^+n$ for solutions A and C. The solid line indicates $T_{lab} = 1000$ MeV; the longer dash in the dashed line indicates the higher energy. .	79
6-52	$\sigma(\theta)$ of $K_L^0p \rightarrow K^+n$ for solutions A and C. The solid line indicates $T_{lab} = 1000$ MeV; the longer dash in the dashed line indicates the higher energy. .	79
6-53	$P(\theta)$ of $K^+n \rightarrow K^0p$ for solutions A and C. The solid line indicates $T_{lab} = 1000$ MeV; the longer dash in the dashed line indicates the higher energy. .	80
6-54	$R(\theta)$ of $K^+n \rightarrow K^0p$ for solutions A and C. The solid line indicates $T_{lab} = 1000$ MeV; the longer dash in the dashed line indicates the higher energy. .	80
6-55	$\sigma(\theta)$ of $K^+d \rightarrow K^0pp$ with no momentum cuts for solutions A and C. The solid line indicates $T_{lab} = 1000$ MeV; the longer dash in the dashed line indicates the higher energy.	81
6-56	$\sigma(\theta)$ of $K^+d \rightarrow K^0p(p)$ with momentum cuts of 100 and 250 MeV/c for solutions A and C. The solid line indicates $T_{lab} = 1000$ MeV; the longer dash in the dashed line indicates the higher energy.	81

- 6-57 $\sigma(\theta)$ of $K^+d \rightarrow K^+np$ with no momentum cuts for solutions A and C. The solid line indicates $T_{lab} = 1000$ MeV; the longer dash in the dashed line indicates the higher energy. 82
- 6-58 $\sigma(\theta)$ of $K^+d \rightarrow K^+n(p)$ with momentum cuts of 100 and 250 MeV/c for solutions A and C. The solid line indicates $T_{lab} = 1000$ MeV; the longer dash in the dashed line indicates the higher energy. 82

List of Tables

2-1	Isoscalar K^+N data base ($T_{lab}=0$ to 1100 MeV).	8
2-1	Isoscalar K^+N data base (Continued)	9
4-1	Cutoffs.	24
5-1	Coupling Between K^+N and Inelastic Channels.	37
6-1	Progression of χ^2 per data point for each data base.	44
6-2	Poles and Zeroes.	47
6-3	Theoretical Poles.	49
6-4	Scattering Lengths.	51

Chapter 1

Introduction

1.1 Motivation

The K^+ -nucleon (K^+N) elastic reaction is interesting due to its characterization by Z^* resonances [AR85, Ha84] which may be $q^4\bar{q}$ configurations. One of the purposes of this work is to determine resonance pole positions of the isoscalar states of the K^+ -nucleon reaction. No one has previously determined resonance pole positions by analytical continuation as we are doing at VPI&SU. As a result, no resonance pole positions have been listed in the Particle Data Tables for the isoscalar states.

Secondly, a kaon factory has been proposed at TRIUMF. The K^+N amplitudes generated by this study are necessary for the examination of kaon-induced nuclear reactions. Also, through this work, experiments to further define the K^+N amplitudes will be suggested.

1.2 History

This work is one of few simultaneous isoscalar and isovector analyses [Ha84, Na82] of the K^+N scattering system since the measurements of all the polarizations [82K1, 80R1, 80W1]

in the 1980's. Hashimoto [Ha84] has done the most recent single-energy analysis of this system. Hashimoto calculated his own form factors and included all reactions except elastic K^+d data in his analysis from 0.6 to 1.5 GeV/c. The state P_{11} ($L_{I,2J}$) shows minimal counterclockwise motion in the Argand diagram, yet D_{03} and P_{13} show clearer counterclockwise motion. Counterclockwise motion in the argand diagram is suggestive of a resonance.

Nakajima et al. [Na82] have done the most recent energy-dependent analysis of this system. Utilizing Alberi's [Al72] form factors and Martin's [75M1] energy-dependent parametrization, they also omitted elastic K^+ -deuteron (K^+d) data to acquire their solution up to 1.6 GeV/c. They detected counterclockwise motion in the Argand diagrams of the P_{13} , P_{01} , and D_{03} states. However, they indicated that the structures may be due to either resonances or complex structures in the complex plane. The maxima of the speed plots do not coincide with the resonance mass from a Breit-Wigner fit.

Martin and Oades [MO80] performed the next most recent analysis. Their single-energy solution was kept smooth by imposing a fixed t-dispersion relation at different energies. They included one set of the 1980's polarization data [80R1], yet omitted the K^+d elastic also. They detected counterclockwise motion in the P_{13} and P_{01} waves, yet discounted the identification of these waves with resonances due to the speed plots. These waves are concluded to be complicated structures in the complex plane.

Martin [75M1] performed the oldest energy-dependent analysis which I wish to discuss. He parametrized the inverse of the amplitudes by center of momentum (c.m.) quantities, including the inelastic threshold and maximum c.m. momentum of the analysis. Unitarity and proper threshold behavior for the partial waves are guaranteed. He performed fits with and without the K^+d elastic data, yet reported only the solution without the K^+d elastic data. Counterclockwise motion in the argand diagram was found in the P_{13} , P_{01} , and D_{03} states.

Several studies of the isovector system alone exist. The energy-dependent analysis performed at VPI&SU extended up to 3 GeV/c [AR85]. The parametrization relied on the

two-channel coupled K-matrix. Proper threshold behavior for partial waves was generated in the parametrization. Elastic K^+N states were coupled to the inelastic $K^+\Delta(1232)$. Resonance poles were found in the P_{11} , P_{13} , and D_{15} states. The P_{13} has the strongest physical effect and is followed by the P_{11} and D_{15} in succession. The effects of the P_{11} and D_{15} states are reduced by zeros lying closer to the elastic cut than their resonances. Other analyses exist, but are older and will not be discussed.

1.3 Structure of the Dissertation

In this dissertation, I shall discuss the mechanics of the K^+N partial-wave analysis and the results. Since the data drive the selection of the theory, general characteristics of the data will be discussed in Chapter 2. Explanation of the necessary theories to describe the data will follow in Chapters 3 and 4. Detailed characteristics of the K^+d scattering data which are highlighted by the theory and necessary for the analysis will be indicated in Chapter 4. The χ^2 -minimization technique and parametrization for the scattering matrix will be reviewed in Chapter 5. The solutions will be examined in Chapter 6 with conclusions and recommendations following in Chapter 7.

An orderly presentation of the data and theory will be strived for; yet, with the interplay between the two, references from one to the other will be necessary.

Chapter 2

Data Base

2.1 The K^+ -Nucleon Isoscalar Data Base

The K^+N reaction consists of two isospin states, $I=0$ (isoscalar) and $I=1$ (isovector). The isovector states may be determined fully from the elastic K^+p reaction. In fact, an isovector analysis has been done up to 2650 MeV at VPI&SU [AR85]. The isoscalar states are determined from K^+d breakup and elastic reactions, and from K_L^0 , the long lived kaon, scattering from a target proton; actually, data acquired from these reactions contribute to both isoscalar and isovector states.

The deuteron is used as a target since a free neutron target is not available. The deuteron is bound weakly and lends itself well to the impulse approximation (see Chapter 4) which allows the neutron to be extracted as a target from the deuteron.

Table 2-1 shows a breakdown of the 1746 isoscalar data which have been considered in this analysis. The range of incident lab kinetic energies and number of data within the range are denoted according to each experiment. Each experiment is labelled according to a short identification, ID, which also serves as its reference. This ID is used to identify the

experiment in the Scattering Analysis Interactive Dial-In (SAID) computer program. The data will be discussed in the following sections. The isoscalar contribution of the data is only sufficient to 1100 MeV since the data are too sparse above this energy to define the amplitudes.

All data are specified in the K^+N center-of-momentum frame in the data base. The center-of-momentum is taken between the interaction kaon and nucleon in the final state of the K^+d inelastic reactions. Conversions from the lab or invariant momentum transfer frame (t) were made on [75M1, 76E2, 75S1, 77G1] $K^+d \rightarrow K^+d$, and [77G1] $K^+d \rightarrow K^+np$ data sets.

2.1.1 K^+d Breakup Reaction

The K^+d breakup reaction consists of $K^+d \rightarrow K^+np$ and $K^+d \rightarrow K^0pp$ reactions. It has produced the most data from which isoscalar determinations may be made. In addition to providing measurements of differential cross sections of $K^+d \rightarrow K^+np$ and $K^+d \rightarrow K^0pp$, observables for K^+n elastic, charge-exchange, and pure isoscalar have been extracted from this scattering. Most of the total (σ_{tot}), reaction (σ_{in}), and differential cross section ($\sigma(\theta)$) measurements have been made in deuterium bubble chambers, although a few have used scintillation counters and spark chambers.

Typically, statistical errors range from 10-25% for the breakup cross section data derived from bubble chambers and are generally less for the scintillator cross section data. The polarization data generally have higher statistical errors than the cross section data.

All charge-exchange breakup cross section data are consistent. Yet, of the non-charge exchange cross section data, several experiments disagree somewhat. First of all, the Giacomelli et al. [73G1, 73G2] experiments agree with one another. The Rutherford data [75D1] agree with Giacomelli et al.[73G1] at two of its energies, yet have larger values at three energies for angles $\cos\theta > 0.3$.

The data of Glasser et al.[77G1] agree with the other $K^+d \rightarrow K^+np$ data at the two lower energies, yet at 273 MeV a hump in the data rises well above the Rutherford values. Glasser et al.'s errors are smaller and the data exhibit a slight oscillatory behavior not seen in the other data. The Glasser data are valuable since they extend well into the backward angles.

75% of the data of Adams et al.[75A2] agree with Giacomelli's [73G1] 180° data acquired from Legendre fits. The two points which disagree are higher than Giacomelli's values.

Stenger et al.[64S1] measure a combination of $K^+d \rightarrow K^+np$ and $K^+d \rightarrow K^+d$ data. They indicate that the $K^+d \rightarrow K^+d$ contribution is small.

Figure 2-1-2-4 show the contribution of the K^+d breakup data to the data base. The graphs show that the largest concentration of data exists for the $K^+d \rightarrow K^0pp$ and is followed by the $K^+d \rightarrow K^+np$ data. For the $K^+d \rightarrow K^0pp$ reaction the entire energy range is covered except at the forward and backward directions. The $K^+d \rightarrow K^+np$ data base shows a lack of data at less forward angles and is much sparser where data exists. Only the data from Glasser et al.[77G1] extends into the backward range.

2.1.2 K^+d Elastic Reaction

The K^+d elastic data have errors typically in the upper range and higher than the breakup data. Only measurements of the differential cross section exist for this reaction. Elastic K^+d data are found only at forward angles except at low energies. These low-energy data extending into the backward angles are from Glasser et al. [77G1]. Figure 2-5 shows the distribution of these data.

2.1.3 K_L^0 p Scattering

Elastic total (σ_{el}) and differential cross section data are available for this reaction. The K_L^0 is the incident particle since the K_S^0 decays in the beam before reaching the target.

Figure 2-6 shows a distribution of these data.

Aside from the above described reactions, Martin [75M1] calculated the real portion of the forward scattering amplitude ($\Re f$) "data" from total cross section and dispersion relations.

Table 2-1: Isoscalar K^+N data base ($T_{lab}=0$ to 1100 MeV).

Forward Data			
Reaction	Observable	Energy (Data)	ID and Reference
$K^+n \rightarrow K^+n$	σ_{tot}	522-1078(13)	70C1
$K_L^0p \rightarrow K^+n$	σ_{el}	132(1)	71M1
I=0	σ_{tot}	149-680(19)	73C1
	σ_{in}	502-958(4)	71B2
		315-1095(13)	72G2
	Re f	39-1086(14)	75M1
Angular Data			
$K^+n \rightarrow K^+n$	$\sigma(\theta)$	621-1086(11)	75A2
	P(θ)	490-945(43)	80R1
		675-1076(34)	82K1
$K_L^0p \rightarrow K^+n$	$\sigma(\theta)$	303-555(9)	76E2
		322-1038(128)	77A1
$K^+n \rightarrow K^0p$	P(θ)	283(5)	69R1
		490-945(39)	80W1
		675-1076(30)	82K1
$K^+d \rightarrow K^0pp$	$\sigma(\theta)$	100-456(26)	61S2
		283(10)	69R1
		502-958(80)	71H1
		314-1095(260)	72G2
		379-1095(116)	73B5
		163-564(114)	75D1
		60-273(40)	77G1
		354-524(60)	77S1
$K^+d \rightarrow K^+p(n)$	$\sigma(\theta)$	127-231(10)	64S1
		314-1095(238)	73G1
		379-1010(75)	73G2
		163-564(99)	75D1
		107-273(29)	77G1

Table 2-1: Isoscalar K^+N data base (Continued)

Angular Data			
Reaction	Observable	Energy (Data)	ID and Reference
$K^+d \rightarrow K^+d$	$\sigma(\theta)$	314-1095(141)	74G1
		283-524(59)	75S1
		107-273(26)	77G1

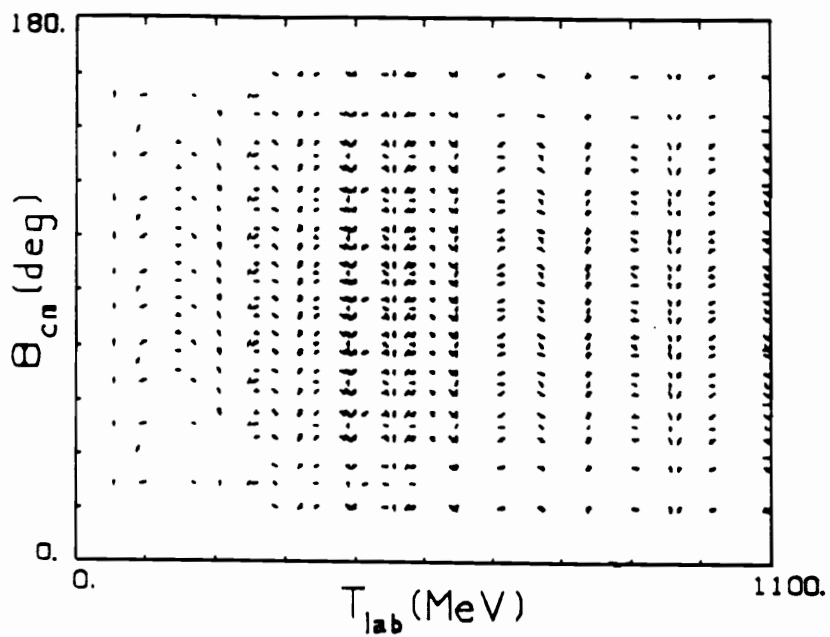


Figure 2-1: Data distribution for $\sigma(\theta)$ of $K^+d \rightarrow K^0pp$.

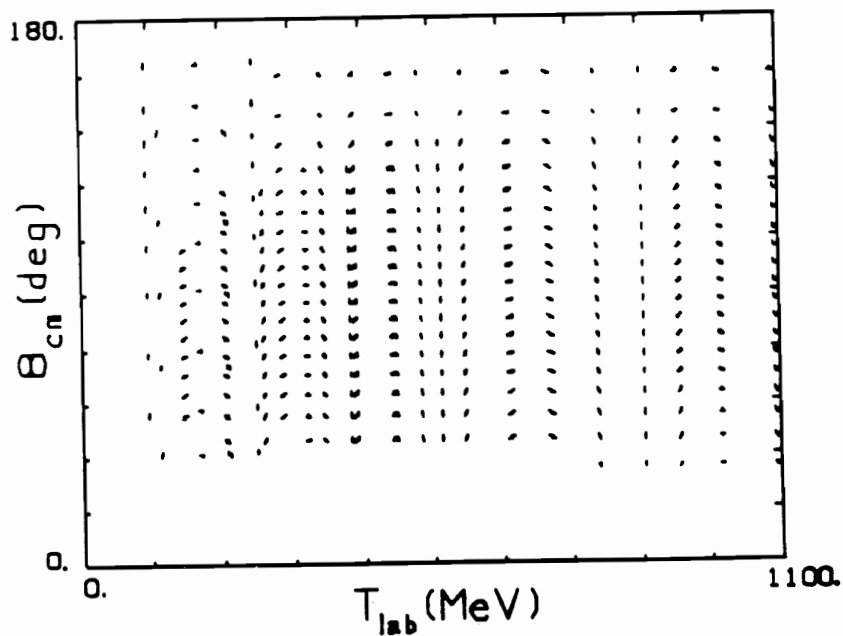


Figure 2-2: Data distribution for $\sigma(\theta)$ of $K^+d \rightarrow K^+np$.

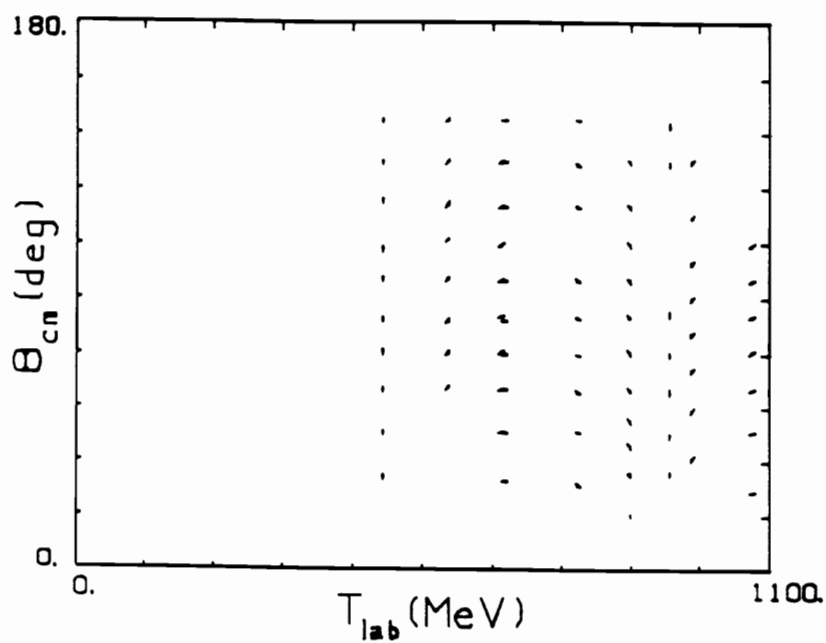


Figure 2-3: Data distribution for $P(\theta)$ of $K^+n \rightarrow K^+n$.

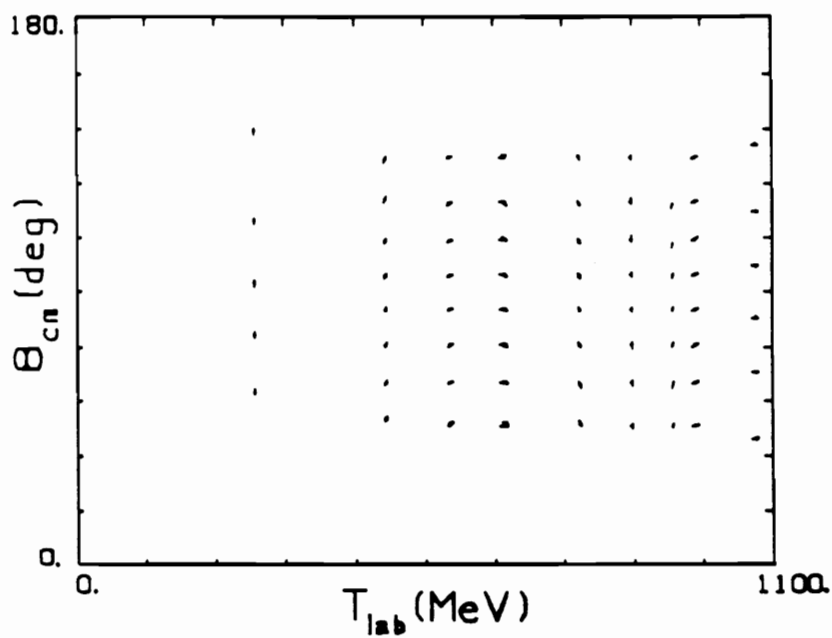


Figure 2-4: Data distribution for $P(\theta)$ of $K^+n \rightarrow K^0p$.

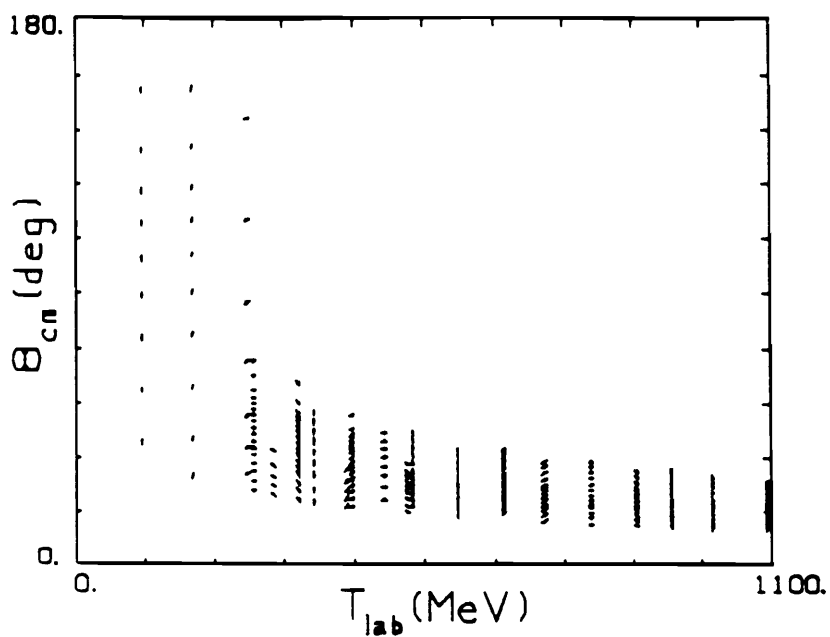


Figure 2-5: Data distribution for $\sigma(\theta)$ of $K^+d \rightarrow K^+d$.

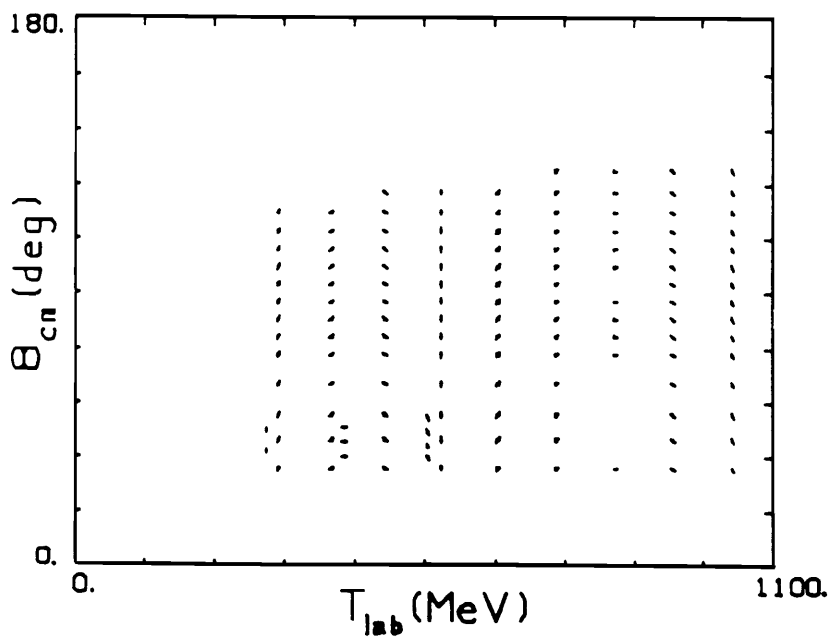


Figure 2-6: Data distribution for $\sigma(\theta)$ of $K_L^0 p \rightarrow K^+ n$.

Chapter 3

Two-Body Theory

The strong T-matrix, T_N , of two-body scattering theory is defined as

$$T_N(\mathbf{k}, \theta) \propto f_N(\mathbf{k}, \theta) + i\vec{\sigma} \cdot \hat{n}g_N(\mathbf{k}, \theta) \quad (3.1)$$

where $f_N(\mathbf{k}, \theta)$ and $g_N(\mathbf{k}, \theta)$ are the non-spin-flip and spin-flip strong amplitudes, and \mathbf{k} and θ are the c.m. momentum and scattering angle, respectively. $\vec{\sigma}$ is the set of Pauli spin matrices and \hat{n} is the unit normal to the scattering plane. This nuclear T-matrix is utilized in the angular momentum representation and is modified to account for electromagnetic effects. The final forms of the nonspin and spin flip amplitudes and their relationship to the observables from two-body scattering are indicated.

3.1 Nuclear Amplitudes

The two-body reactions are described by the non-spin-flip, $f_N(\mathbf{k}, \theta)$, and spin-flip, $g_N(\mathbf{k}, \theta)$, center-of-momentum amplitudes in the angular momentum representation by

$$f_N(\mathbf{k}, \theta) = \frac{\hbar c}{k} \sum_{l=0}^{\infty} [(l+1)T_{l+}(k) + lT_{l-}(k)]P_l(\cos \theta) \quad (3.2)$$

and

$$g_N(\mathbf{k}, \theta) = \frac{\hbar c}{k} \sum_{l=0}^{\infty} [T_{l_+}(\mathbf{k}) + T_{l_-}(\mathbf{k})] P_l^1(\cos \theta) \quad (3.3)$$

where the T-matrix in the angular momentum representation is defined as

$$T_{l_{\pm}}(\mathbf{k}) = \frac{\eta_{l_{\pm}}(\mathbf{k}) \epsilon^{2i\delta_{l_{\pm}}(\mathbf{k})} - 1}{2i} \quad (3.4)$$

and $T_{l_{\pm}}(\mathbf{k})$ refers to $T_{j=l_{\pm}1/2}$ where \mathbf{k} is the center-of-momentum momentum. The dependence of the non-spin-flip and spin-flip amplitudes on \mathbf{k} will be assumed in the remainder of this dissertation. Isospin invariance requires that

$T_{l_{\pm}} \rightarrow T_{l_{\pm}}^1$ for K^+p amplitudes (f_p),

$T_{l_{\pm}} \rightarrow \frac{1}{2}(T_{l_{\pm}}^1 + T_{l_{\pm}}^0)$ for K^+n amplitudes (f_n), and

$T_{l_{\pm}} \rightarrow \frac{1}{2}(T_{l_{\pm}}^1 - T_{l_{\pm}}^0)$ for charge exchange amplitudes (f_x),

where the 1 and 0 superscripts indicate the isospin value.

3.2 Electromagnetic Effects

3.2.1 S-Matrix Product

The electromagnetic effect is included in the total S-matrix in the angular-momentum representation by the product

$$S_{tot} = S_N S_{em} \quad (3.5)$$

where S_N and S_{em} are the nuclear and electromagnetic S matrices, respectively. Thus, the total T-matrix is written as

$$T_{tot} = T_{em} + T_N S_{em} \quad (3.6)$$

where

$$S_{em} = \epsilon^{i(\phi_l + \phi'_l)}. \quad (3.7)$$

and ϕ_l and ϕ'_l are the Coulomb phase shifts for the initial and final channels, respectively. They are [ZA80]

$$\phi_l = \sum_{j=1}^l \tan^{-1} \frac{\eta}{j}, \quad (3.8)$$

where $\eta = q_1 q_2 \alpha c / v_L$, α is $1/137$, v_L is the lab velocity, q_1 and q_2 are the charges of the interacting kaon and nucleon, and $\phi_0 = 0$. T_{em} is produced by nonrelativistic Rutherford scattering [Me70] and the first order α relativistic correction due to the proton Dirac and Pauli form factors. This relativistic electromagnetic correction is taken from Höhler et al. [HK79]. S_{em} is unitary except for the small relativistic contribution, which makes the total S-matrix nearly unitary. Except for the K^+p channel, $\phi_l = \phi'_l = 0$. No relativistic correction is needed for the data contributing to the isoscalar phases due to the roughness in which the K^+n amplitudes are acquired from $K^+d \rightarrow K^+np$ scattering (see next chapter).

3.2.2 Coulomb Barrier

The nuclear T-matrix, T_N , is charge corrected (T_{cc}) for the Coulomb barrier as follows:

$$T_{cc} = \frac{B_l T_N}{1 + i(1 - B_l)T_N} \quad (3.9)$$

where B_l is the Coulomb barrier factor. The Coulomb barrier factors are defined by

$$B_l = B_0 \prod_{j=1}^l \left[1 + \left(\frac{\eta}{j} \right)^2 \right]. \quad (3.10)$$

where

$$B_0 = \frac{2\pi\eta}{e^{2\pi\eta} - 1} \quad (3.11)$$

and η is defined in the previous section. Both B_l and ϕ_l of the previous subsection come from solving the radial wave equation for a Coulomb potential [PB75]. For all cases except the $K^+p \rightarrow K^+p$ reaction, $B_l = 1$, which means that $T_N = T_{cc}$. This is documented further in Arndt et al. [AF85].

3.3 Final Amplitudes

The final forms of the total amplitudes are

$$f_p(\theta) = f_{em} + \frac{\hbar c}{k} \sum_{l=0}^{\infty} \epsilon^{2i\phi_l} [(l+1)(T_{l+})_{cc} + l(T_{l-})_{cc}] P_l(\cos \theta) \quad (3.12)$$

$$g_p(\theta) = g_{em} + \frac{\hbar c}{k} \sum_{l=0}^{\infty} \epsilon^{2i\phi_l} [(T_{l+})_{cc} + (T_{l-})_{cc}] P_l^1(\cos \theta) \quad (3.13)$$

and

$$f_n(\theta) = \frac{\hbar c}{k} \sum_{l=0}^{\infty} [(l+1)(T_{l+})_N + l(T_{l-})_N] P_l(\cos \theta) \quad (3.14)$$

$$g_n(\theta) = \frac{\hbar c}{k} \sum_{l=0}^{\infty} [(T_{l+})_N + (T_{l-})_N] P_l^1(\cos \theta) \quad (3.15)$$

and

$$f_x(\theta) = \frac{\hbar c}{k} \sum_{l=0}^{\infty} [(l+1)(T_{l+})_N + l(T_{l-})_N] P_l(\cos \theta) \quad (3.16)$$

$$g_x(\theta) = \frac{\hbar c}{k} \sum_{l=0}^{\infty} [(T_{l+})_N + (T_{l-})_N] P_l^1(\cos \theta) \quad (3.17)$$

where the proper isospin structure must be utilized. f_{em} is proportional to T_{em} described in section 3.2.1.

3.4 Observables

Possible observables in the KN system consist of measurements both independent and dependent of angle. The most common of the measurements independent of angle is the total cross section:

$$\sigma_{tot} = \frac{4\pi}{k} \text{Im} f(\theta = 0^\circ). \quad (3.18)$$

It is formed of elastic and inelastic contributions:

$$\sigma_{tot} = \sigma_{el} + \sigma_{in} \quad (3.19)$$

The most common measurement of angular observables is the angular distribution of outgoing particles for an unpolarized target:

$$\frac{d\sigma}{d\Omega} = |f(\theta)|^2 + |g(\theta)|^2 \quad (3.20)$$

The polarization, $P(\theta)$, of the recoiling nucleon in the direction perpendicular to the scattering plane is given by

$$\frac{d\sigma}{d\Omega} P(\theta) = 2\text{Im}[f(\theta)g^*(\theta)] \quad (3.21)$$

The polarization can be determined from the asymmetry in a double-scattering experiment. In this case, the initial scattering polarizes the initially unpolarized beam and the differential cross section is measured from the second target. The polarization is determined by

$$P(\theta)P_i = \frac{\frac{d\sigma}{d\Omega}(\theta) - \frac{d\sigma}{d\Omega}(-\theta)}{\frac{d\sigma}{d\Omega}(\theta) + \frac{d\sigma}{d\Omega}(-\theta)}, \quad (3.22)$$

where $P(\theta)$ is the polarization produced by the initial scattering, P_i is the analyzing power of the second scatterer, i.e. the polarization it would produce when scattering an unpolarized beam, and $\frac{d\sigma}{d\Omega}$ is the differential cross section measured from the second target. The polarization can also be measured from the scattering asymmetry off of a polarized target; all recent polarization measurements are made in this way. The spin observables $R(\theta)$ and $A(\theta)$ determine polarization of the recoil nucleon in the scattering plane from transverse and longitudinally polarized targets, respectively. They are

$$\frac{d\sigma}{d\Omega} \begin{pmatrix} R(\theta) \\ A(\theta) \end{pmatrix} = \begin{pmatrix} \cos\theta & \sin\theta \\ -\sin\theta & \cos\theta \end{pmatrix} \begin{pmatrix} |f(\theta)|^2 - |g(\theta)|^2 \\ -2\text{Re}f(\theta)g^*(\theta) \end{pmatrix} \quad (3.23)$$

P , R , and A are related such that $P^2 + R^2 + A^2 = 1$. Other observables exist [Fo88], but are linear combinations or otherwise functions of the observables listed here.

Chapter 4

K^+d Theory

Separate theories describe the inelastic and elastic K^+d scattering. Yet, each of these theories describes the interaction of the kaon and deuteron in terms of two-body elastic K^+N amplitudes. The single-scattering models utilized to describe each of these reactions are called impulse approximations. Single scattering is justified since the distance between the nucleons is relatively large in the deuteron compared to the nucleon size. Also, the strong interaction between the incident kaon and target nucleon is weaker than the pion-nucleon and nucleon-nucleon interactions. In each case before the collision, the target nucleon is motionless.

4.1 K^+d Breakup

The K^+d breakup theory is taken from a publication by K. Hashimoto [Ha84]. In this theory one nucleon in the deuteron undergoes no strong interaction with any other particle and is labelled a spectator. The outgoing spectator emerges with a momentum comparable with the Fermi momentum. This interaction is depicted in Figure 4-1. Other breakup

theories have been developed by Alberi et al. [A172] and Stenger et al. [64S1]. Hashimoto's theory is simplified from Alberi's, yet uses fully relativistic kinematics, unlike Stenger's.

The invariant amplitude to describe the K^+d breakup reaction is

$$T = \sqrt{(16\pi^3 M)}[T_N(\vec{p})\Psi(\vec{q}) + T_N(\vec{q})\Psi(\vec{p})] \quad (4.1)$$

where T_N is the K^+N two-body interaction and Ψ is the S-wave deuteron wave function. T_N is a function of the lab momentum of the interaction nucleon and Ψ is a function of the spectator momentum. T_N is in general unphysical due to the interaction of the off-shell nucleon. Yet, the lab T_N is assumed and is physical near zero spectator momentum, provided the deuteron binding energy and the mass difference between the neutron and proton is neglected. Taking the lab T_N partially justifies omission of the D-wave deuteron wave function. In addition, the D-wave is omitted due to the errors on the breakup data (section 2.1.1) and the inaccuracy with which the experimental K^+N amplitudes are extracted from the breakup data (see following discussion). More accurate measurements may necessitate its inclusion.

The cross section formulae derived from this amplitude are [Ha84]

$$\frac{d\sigma}{d\Omega}(K^+d \rightarrow K^0pp) = (|f_x|^2 + |g_x|^2)[I(\theta) - J(\theta)] + \frac{2}{3}|g_x|^2 J(\theta) \quad (4.2)$$

and

$$\frac{d\sigma}{d\Omega}(K^+d \rightarrow K^+np) = (|f_p|^2 + |g_p|^2)I_n(\theta) + (|f_n|^2 + |g_n|^2)I_p(\theta) + 2Re(f_p^* f_n + \frac{1}{3}g_p^* g_n)J(\theta) \quad (4.3)$$

where f and g are the K^+N two-body elastic amplitudes and $I(\theta)$ and $J(\theta)$ are the inelastic form factors, which for no spectator specification are

$$I(\theta) = K \int \frac{k^2 dk}{\omega} \frac{d^3 p}{E_p} \frac{d^3 q}{E_q} \delta^4(k_0 + P - k - p - q) \frac{\Psi^2(\vec{p}) + \Psi^2(\vec{q})}{2} \quad (4.4)$$

and

$$J(\theta) = K \int \frac{k^2 dk}{\omega} \frac{d^3 p}{E_p} \frac{d^3 q}{E_q} \delta^4(k_0 + P - k - p - q) \Psi(\vec{p})\Psi(\vec{q}) \quad (4.5)$$

where

$$K = \frac{\omega m E}{k^2} \frac{d(\omega + E)}{dk}; \quad E_p = p^2 + m^2; \quad \text{and } \omega = k^2 + \mu^2. \quad (4.6)$$

$I(\theta)$ is the inelastic form factor for the interaction of the K^+ with one nucleon in the deuteron and $J(\theta)$ represents the interference between two two-body interactions. In the non-charge-exchange breakup reaction (Eq. 4.3) the subscript on $I(\theta)$ designates the spectator particle. If no spectator is defined $I_n(\theta) = I_p(\theta) = I(\theta)$. Otherwise, the momentum of the spectator nucleon is constrained.

4.1.1 Cutoffs on the Spectator Momentum

Cutoffs on the spectator momentum arise due to the equipment, primarily liquid deuterium bubble chambers, that are used for measurements. In this chamber the visibility of the outgoing charged nucleon depends upon its momentum. The lower limit of visibility is 100 MeV/c [73G1]. Therefore, a charge-exchange experiment which has one outgoing trace (one prong) will place an upper limit on the spectator momentum of 100 MeV/c. If two traces are seen (two prongs) then the lower momentum cutoff is 100 MeV/c. For the experiments with a lower momentum cutoff an upper cutoff consistent with the impulse approximation is specified; this ensures a low momentum transfer event. For $K^+d \rightarrow K^+np$ the prongs are due to the $\tau(\pi^-\pi^+\pi^+)$ decay, a signature of the K^+ , and the proton. Thus, only one or two prongs may arise. In the very forward region where a minimal, if any, trace is available, the K^+d coherent(elastic) scattering contaminates the scattering for the noncharge-exchange breakup reaction[5,6].

Graphs of the form factors calculated from our vectorized code appear in Figures 4-2-4-5. General features include the angular and energy independence of $I_p(\theta)$ except at extremely forward angles. In contrast, $J(\theta)$ is both energy and angular dependent. $I_n(\theta)$ of $K^+d \rightarrow K^+np$ has been omitted since its magnitude at the graphed energies is negligible except at extremely forward angles ($\cos \theta \geq 0.9$). At these energies, its magnitude is comparable to the $J(\theta)$ for the cut $100 < p_L < 250$ MeV/c where p_L is the momentum of

the spectator in the lab. $J(\theta)$ for the cut $100 < p_L < 250$ MeV/c on $K^+d \rightarrow K^+np$ is omitted since it is smaller than $J(\theta)$ for the cut $0 < p_L < 100$ MeV/c. As can be seen, the cutoffs reduce the contribution of the amplitudes to the cross section. In each case where a cutoff is utilized in the theory, the cutoff is on the proton momentum which has a lesser momentum than the nonspectator nucleon.

In $K^+d \rightarrow K^+np$ experiments the spectator is almost always the proton since this choice suppresses the K^+p amplitudes. The $K^+d \rightarrow K^+p(n)$ data (parenthesis denote the spectator) is omitted since the two-body elastic K^+p data determine the elastic K^+p amplitudes much more accurately. The K^+p amplitudes are relatively well defined by the elastic K^+p reaction. Emphasis on K^+n amplitudes for the $K^+d \rightarrow K^+n(p)$ reaction is reflected in our calculated $I_n(\theta)$ since it is negligible on the scale of the $I_p(\theta)$. The cutoffs for all K^+d breakup experiments ensure a low momentum transfer and are given in Table 4-1.

4.1.2 Scaling of Inelastic Form Factors

The experimenters scale the cross section data acquired from cutoffs to their nonconstrained values. To do this they scale the angular distribution to the unconstrained total cross section. Likewise, in our model we must scale the cutoff cross section. We scale the cutoff cross sections by

$$\frac{I_p(\theta) \text{ no cut}}{I_p(\theta) \text{ cut}}$$

at $\theta_{cm} = 90^\circ$. One can see in the graphs of the form factors that the experiments with cutoffs of 100 to 250 MeV/c must be scaled by nearly four while other cutoff cross section data will be scaled less. A graph of the scaled $I_p(\theta)$ form factor versus the no-cutoff $I_p(\theta)$ is shown in Figure 4-6. Note the angular distribution evident in the scaled form factor. The scaling is done at $\theta_{cm} = 90^\circ$ in order to reduce the overall deviation of the scaled $I_p(\theta)$ from the no-cutoff $I_p(\theta)$. Since scaling the cross section is equivalent mathematically to scaling the form factors, the ratio of $I_n(\theta)/I_p(\theta)$ and $J(\theta)/I_p(\theta)$ is maintained.

4.1.3 Electromagnetic Corrections

The two-body charge-exchange and K^+n elastic amplitudes for the K^+d breakup reactions have the same electromagnetic corrections as their respective two-body reactions. The K^+p elastic amplitudes are not charge corrected for the Coulomb barrier due to the inability of the code in the searching procedure to distinguish between the K^+p and K^+n amplitudes of the $K^+d \rightarrow K^+np$ reaction. Since I could either treat the K^+p or K^+n amplitudes correctly, I chose to treat the K^+n properly since these amplitudes define many of the $K^+d \rightarrow K^+n(p)$ reactions. Also, the overwhelming amount of K^+p elastic reaction data will select the proper K^+p amplitudes.

4.1.4 Cutoffs on Individual Experiments

In all of the $K^+d \rightarrow K^0p(p)$ experiments, a momentum constraint is placed on the spectator proton. Also, each of the nonspectator protons has a higher momentum than the spectator. The actual values for the momentum cutoffs on the spectator are given in Table 4-1. Each of the cross sections measured for this reaction has been scaled to an unconstrained cross section, which was measured either in the same or another experiment.

To determine the $K^+d \rightarrow K^+n(p)$ cross section, the $K^+d \rightarrow K^+p(n)$ and $K^+d \rightarrow K^+d$ contributions to the cross section must be removed from the measurement. Since the neutron is not detected and the charge of the proton and deuteron are the same, this distinction is not trivial. The spectator is the proton and for the most part K^+n amplitudes remain once the $K^+d \rightarrow K^+n(p)$ is isolated.

Giacomelli et al. [73G1, 73G2] make their measurement in a deuterium bubble chamber. They suppress K^+p amplitudes and the $K^+d \rightarrow K^+d$ contribution by selecting only events for which the momentum of the proton is less than the momentum of the neutron, in addition to placing limits on the proton momentum given in Table 4-1. They scale to an

unconstrained cross section. Our form factors verify that the choice of $p_{\text{proton}} < p_{\text{neutron}}$ effectively suppresses the K^+p amplitudes. The value of $I_n(\theta)/I_p(\theta)$ for the cuts of 0 to 100 MeV/c are $\ll 1\%$ and for 100 to 250 MeV/c are $< 5\%$. The $J(\theta)/I_p(\theta)$ are slightly higher in each case.

The Rutherford group [75D1] uses an "effective momentum cut" of 0 to 280 MeV/c on their selection of events. They detect the charged particle by scintillation counters and spark chambers. The means by which they remove K^+p amplitudes and the $K^+d \rightarrow K^+d$ contribution, beyond placing a momentum cut on the proton, is unclear. The data are for the most part consistent with Giacomelli et al.

Glasser et al. [77G1] select all events in a deuterium bubble chamber for which their spectator proton has momentum greater than 100 MeV/c [Sn89]. An upper momentum cut of 250 MeV/c has been applied since our form factors require an upper cut and this choice saturates them. Also, as in the Rutherford data, their means of removing $K^+p \rightarrow K^+p$ amplitudes is unclear. No scaling of their data is indicated, yet the magnitude of their cross sections is consistent with other unconstrained cross sections. A hump arises in this data set at one energy, which disagrees with the Rutherford data [75D1].

Adams et al. [75A2] report measurements of K^+n elastic cross sections at 180° from a measurement of $K^+d \rightarrow K^+n(p)$. They do not describe the technique by which the elastic cross sections are acquired, yet the general magnitude of the cross sections are consistent with the extrapolated values from Giacomelli et al. measurements.

Stenger et al. [64S1] measure a combination of $K^+d \rightarrow K^+np$ and $K^+d \rightarrow K^+d$ cross section data. The $K^+d \rightarrow K^+d$ contribution is indicated to be small and the data are fitted with $K^+d \rightarrow K^+np$ with no spectator momentum cuts.

The consistency of all these data will be reviewed in the solution chapter.

Table 4-1: Cutoffs.

$K^+d \rightarrow K^0pp$	
Short Reference	Cutoff (MeV/c)
61S2	None
69R1	0 to 300
71H1	None
72G2	0 to 250
73B5	100 to 250
75D1	None
77G1	None
77S1	0 to 250
$K^+d \rightarrow K^+np$	
64S1	None
73G1	100 to 250
73G2	0 to 100
75D1	0 to 280
77G1	100 to 250

4.2 K^+d Coherent Scattering

A fixed-scatterer single-scattering impulse approximation is extracted from the double scattering Glauber theory of Hashimoto [Haa83] to describe the $K^+d \rightarrow K^+d$ reaction. Hashimoto's work follows that of Bertocchi and Capella [BC67] and Alberi and Bertocchi [AB69]. The calculation is done in the Breit or "brick wall" frame [Hag63] and is well suited for measuring the applicability of the theory. The Glauber theory is limited to low momentum transfer. The frame and single-scattering reaction used in our theory are described in Figures 4-7 and 4-8 where \vec{n} and \vec{m} are momenta of the K^+ and deuteron in the Breit frame.

We chose to represent the reaction by single scattering because of the large errors on the differential cross section data. According to graphs of $\sigma(\theta)$ of Hashimoto [Had83] at $p_L \geq 900$ MeV/c, many of the single-scattering contributions from a fit of his model without $K^+d \rightarrow K^+d$ data fall within or slightly outside the errors at the forward angles where the data exist. Also, Ferrari [Fe59] estimates the effect of multiple scattering in the impulse approximation at $T_L=100$ MeV to be less than 10% on the cross sections. According to graphs of the impulse approximation presented in a publication of a relativistic Faddeev calculation by Garcilazo [Ga88], only for differential cross section data where $p_L \leq 587$ MeV/c and $\theta_{lab} \geq 70^\circ$ does the Faddeev calculation improve on the impulse approximation. These $K^+d \rightarrow K^+d$ cross section data are the only data away from the forward angle at any energy and come from a single experiment. Yet, $K^+d \rightarrow K^0pp$ and $K^+d \rightarrow K^+np$ [77G1] data sample this kinematic region and provide isoscalar determinations. These $K^+d \rightarrow K^+d$ data where the Faddeev calculation improves on the impulse approximation consist of only eleven measurements, or about 5% of the $K^+d \rightarrow K^+d$ data base. As can be seen from their respective works, the Faddeev calculation and Hashimoto [Had83] depart in their predictions of differential cross section from the impulse approximation in regions where no data exist.

For single scattering the amplitude for the $K^+d \rightarrow K^+d$ reaction is

$$T = 2 \int d^3k \Psi(-\frac{1}{2}\vec{m} - \vec{k}) T_N \Psi(\frac{1}{2}\vec{m} - \vec{k}) \quad (4.7)$$

where Ψ is the full deuteron wave function and T_N is the K^+N amplitude. Since T_N varies little with respect to k in comparison to the remainder of the integrand, T_N is removed from the integration and evaluated where the remainder of the integrand is maximum. Then

$$T = 2T_N \phi(-\vec{m}) \quad (4.8)$$

where ϕ is the elastic deuteron form factor and is evaluated at the incoming deuteron momentum. Since

$$\phi(\vec{q}) = \int d^3r |\Phi(\vec{r})|^2 e^{i(\vec{q}\cdot\vec{r})}, \quad (4.9)$$

the radial S and D deuteron wave function, $\Phi(\vec{r})$, is supplied where \vec{q} and \vec{r} are the three-momentum transfer and radial coordinate.

The elastic form factors calculated from our vectorized code are shown in Figure 4-9. These vary much more dramatically with energy and angle than their inelastic counterparts. In fact, the D-wave contribution to the deuteron wave function is included solely due to the logarithmic variation of the elastic form factors.

The single-scattering formula for the differential cross section is

$$\frac{d\sigma}{d\Omega} = \left(\frac{p_{K^+d}}{p_{K^+n}}\right)^2 (|f_p + f_n|^2 (\phi_s^2 + \phi_q^2) + \frac{2}{3} |g_p + g_n|^2 \phi_m^2) \quad (4.10)$$

where ϕ_s, ϕ_q, ϕ_m are the spherical, quadrupole, and magnetic form factors, respectively. The coefficient $\left(\frac{p_{K^+d}}{p_{K^+n}}\right)^2$ [75M1] is in the center-of-momentum of each system and converts the differential cross section from the center-of-momentum angle of the final interacting kaon nucleon frame to the center-of-momentum of the kaon deuteron system.

4.2.1 Electromagnetic Corrections

The direct Coulomb contribution, f_{em} (Eq. 3.12), utilizes the mass of the deuteron instead of the nucleon mass. Otherwise, the K^+n elastic amplitudes are identical to their respective

two-body reactions. The K^+p elastic amplitudes are not charge corrected for the Coulomb barrier. These amplitudes are restricted in the same manner as those of the $K^+d \rightarrow K^+np$. The effect of the non-charge correction of the K^+p amplitudes in the $K^+d \rightarrow K^+d$ and $K^+d \rightarrow K^+np$ will be discussed in chapter 6 where the solution is discussed.

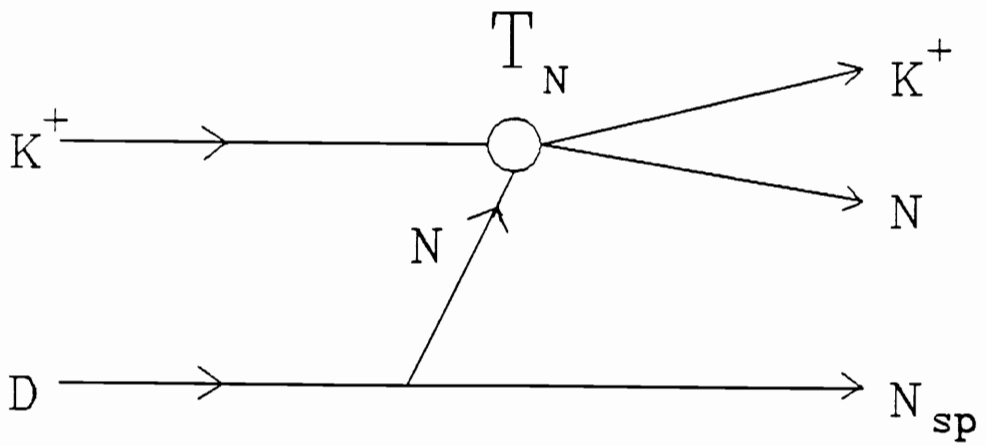


Figure 4-1: K^+ deuteron breakup diagram.

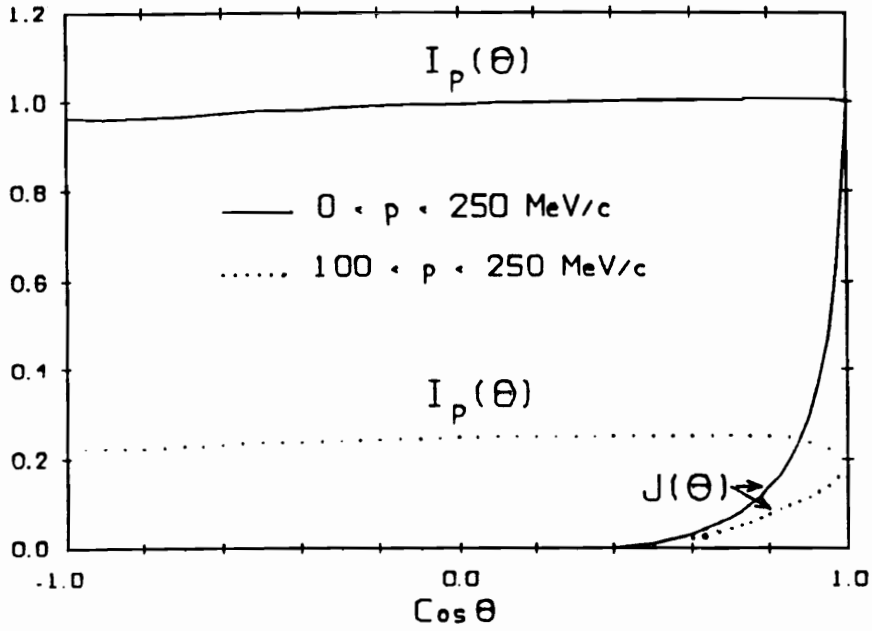


Figure 4-2: Deuteron form factor for $K^+d \rightarrow K^0pp$ at an incident lab energy of 363 MeV.

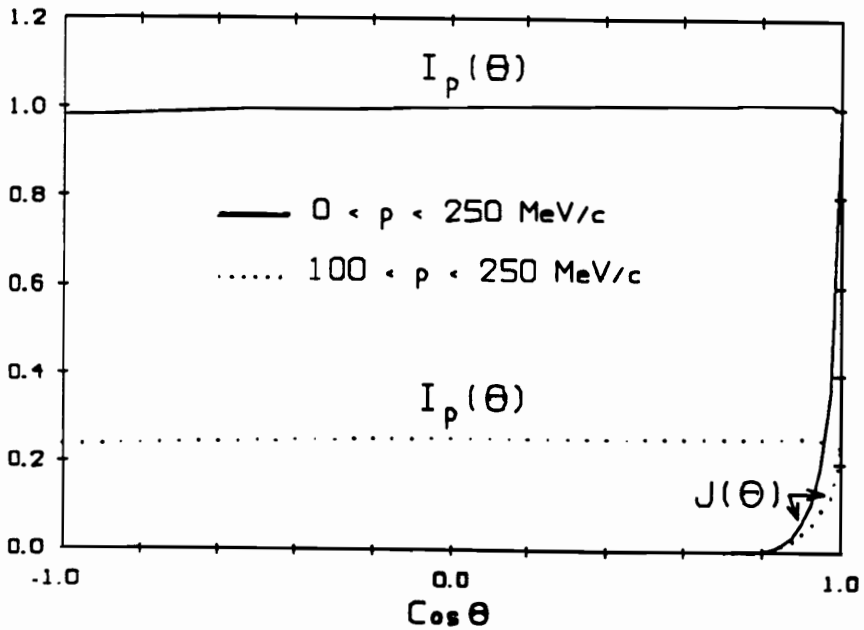


Figure 4-3: Deuteron form factor for $K^+d \rightarrow K^0pp$ at an incident lab energy of 1085 MeV.

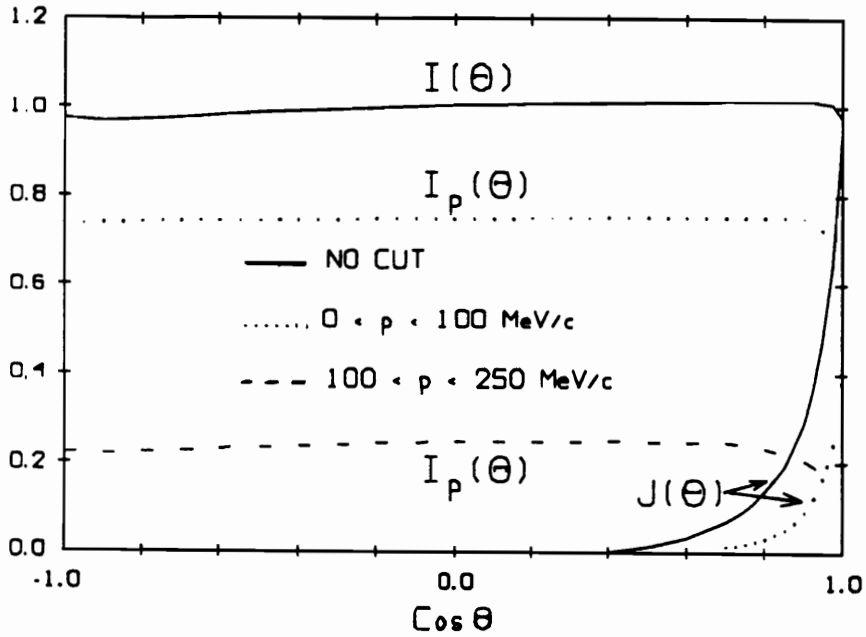


Figure 4-4: Deuteron form factor for $K^+d \rightarrow K^+np$ at an incident lab energy of 363 MeV.

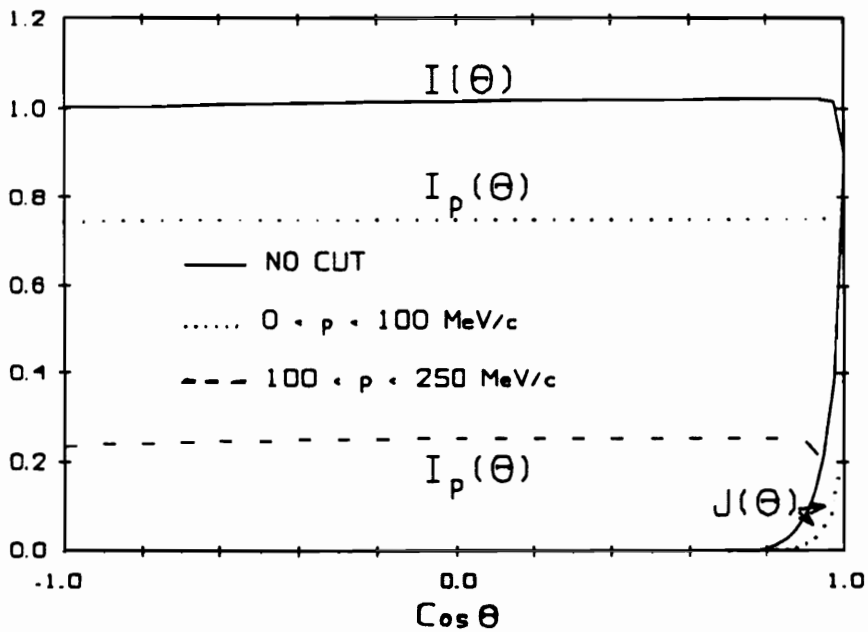


Figure 4-5: Deuteron form factor for $K^+d \rightarrow K^+np$ at an incident lab energy of 1085 MeV.

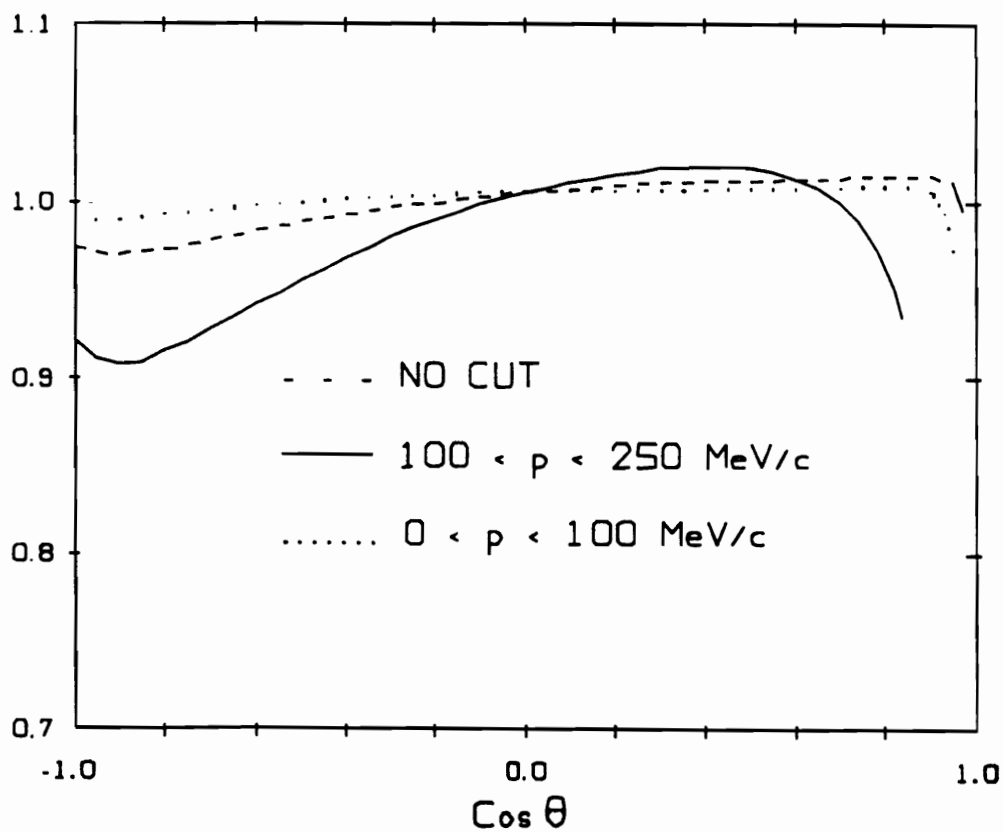


Figure 4-6: Scaled $I_p(\theta)$ for $K^+d \rightarrow K^0pp$ at an incident lab energy of 363 MeV.

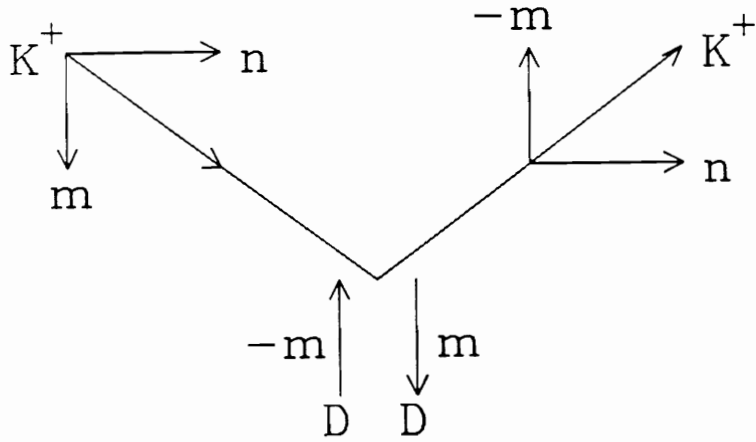
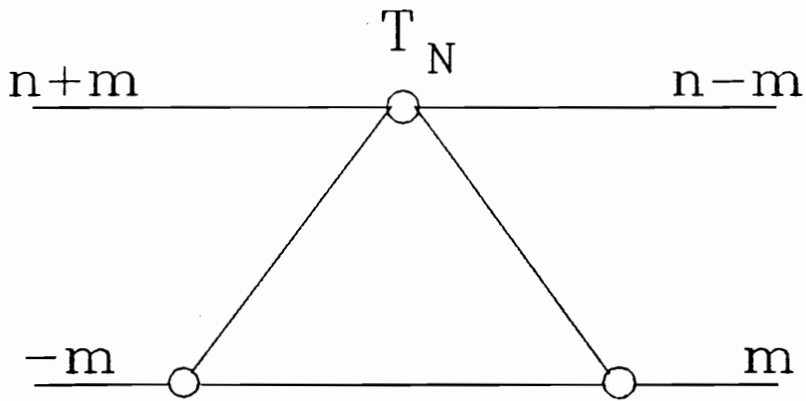


Figure 4-7: Breit frame dynamics.

Figure 4-8: Diagram for $K^+d \rightarrow K^+d$ scattering.

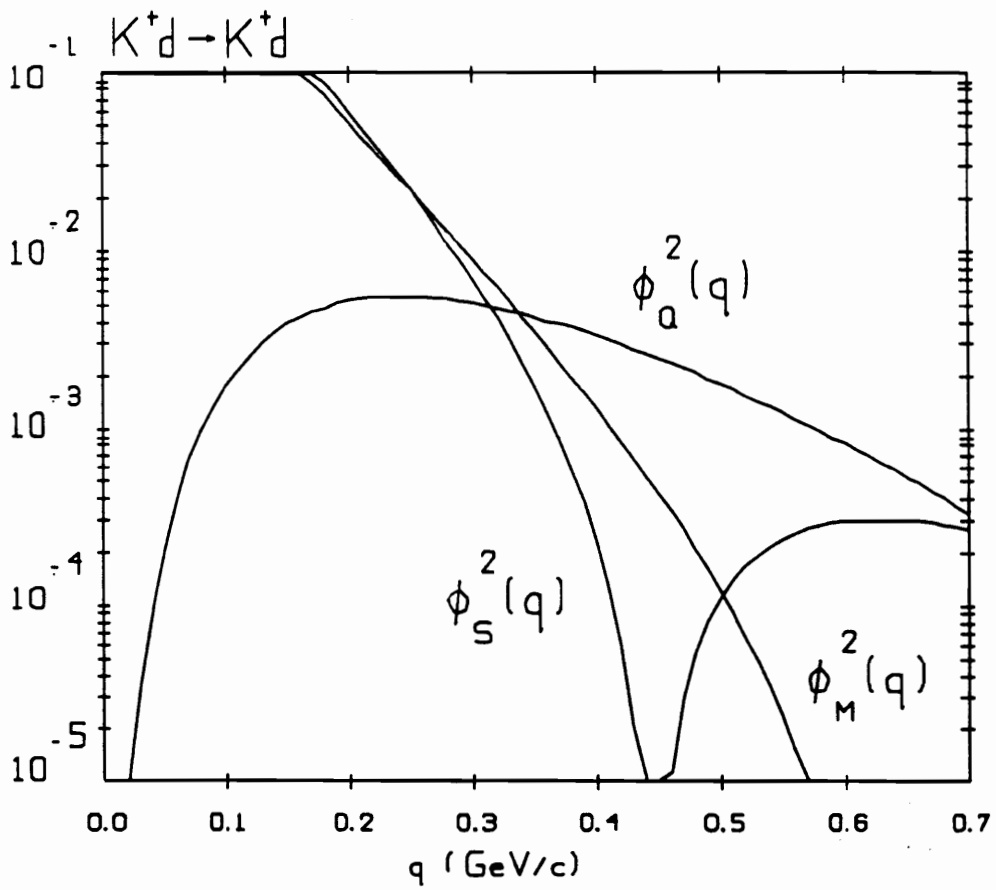


Figure 4-9: $K^+d \rightarrow K^+d$ form factors.

Chapter 5

The Partial-Wave Analysis

The partial-wave analysis couples two complementary techniques of analysis to produce the most physically sensible, accurate solution. The first technique, the single-energy or energy-independent analysis, approximates linearity of the phases and absorption parameters within a small energy bin of data. This analysis provides for small structure, including bogus structure due to unknown systematic errors, in its solution. The second technique, the energy-dependent analysis, provides a smooth solution, perhaps missing some small structure. The two techniques are used iteratively to make sure that the energy-dependent solution contains all required structure. The final single-energy solutions are useful to indicate the accuracy of a solution.

5.1 χ^2 Determination

Each of these analyses depends upon minimizing χ^2 to determine a solution. The formula for χ^2 is [AM66]

$$\chi^2(\vec{p}) = \sum_{j=1}^{N_E} \left[\sum_{i=1}^{N_D} \left(\frac{\alpha^j \theta^i(\vec{p}) - \theta_{exp}^i}{\Delta \theta_{exp}^i} \right)^2 + \left(\frac{\alpha^j(\vec{p}) - 1}{\Delta \alpha_{exp}^j} \right)^2 \right], \quad (5.1)$$

where

$\theta^i(\vec{p})$ = value of observable predicted by the set of variable parameters \vec{p} ,

θ_{exp}^i = experimental value of observable,

$\Delta\theta_{exp}^i$ = experimental standard deviation (statistical error),

$\alpha^j(\vec{p})$ = normalization parameters determined from \vec{p} ,

$\Delta\alpha_{exp}^j$ = normalization or experimental systematic error,

N_D = number of data per experiment and

N_E = number of experiments.

Since χ^2 is taken to be quadratic near the minimum, both first-order and second-order derivatives are required in the minimization process. The normal parameter step (Δp) to minimize χ^2 is [AM66]

$$\Delta p_j = - \left(\frac{\partial^2 \chi^2}{\partial p_j \partial p_k} \right)^{-1} \left(\frac{\partial \chi^2}{\partial p_k} \right) \quad (5.2)$$

where

$$-\frac{1}{2} \frac{\partial \chi^2}{\partial p_k} = \sum_{j=1}^{N_E} \left[\sum_{i=1}^{N_D} \frac{\alpha^j}{\Delta\theta_{exp}^i} \frac{\partial \theta^i(p)}{\partial p_k} \left(\frac{\theta_{exp}^i - \alpha^j \theta^i(p)}{\Delta\theta_{exp}^i} \right) \right] \quad (5.3)$$

and

$$\frac{1}{2} \frac{\partial^2 \chi^2}{\partial p_k \partial p_l} = \sum_{j=1}^{N_E} \left[\sum_{i=1}^{N_D} \frac{\alpha^j}{\Delta\theta_{exp}^i} \frac{\partial \theta^i(p)}{\partial p_k} \frac{\alpha^j}{\Delta\theta_{exp}^i} \frac{\partial \theta^i(p)}{\partial p_l} \right] \quad (5.4)$$

The search ideally continues until the first order derivative becomes small. Both sets of parameters \vec{p} and α^j are determined by fitting the data. This determination is simplified since α^j can be expressed analytically as a function of \vec{p} [AM66]; and thus can be determined from specified \vec{p} by analytic techniques. Generally, parameters whose errors are larger than their values are removed from the search.

5.2 Energy-Dependent Parametrization

This energy-dependent parametrization is used since it is an efficient parametrization. The parametric freedom is incorporated at the level of the K-matrix. The K-matrix is real and symmetric. Its form is

$$\begin{pmatrix} K_e & K_o \\ K_o & K_i \end{pmatrix} \quad (5.5)$$

where K_e and K_o have initial K^+N elastic channels, K_o and K_i have final inelastic channels, and K_i and K_e have inelastic initial and elastic K^+N final channels, respectively. The inelasticity of the isovector and isoscalar channels are provided by the $K^+\Delta$ and $K^{+\ast}(892)N$ final states, respectively. Coupling between the K^+N and the inelastic channels is shown in Table 5-1.

Each of the elements of the K-matrix is expanded in terms of functions of energy. Specifically,

$$K_e = p_1 + p_2z + p_3z^2 + p_4z^3$$

$$K_o = p_6z + p_7z^2$$

and

$$K_i = p_8 + p_9z$$

with $z=(W_{cm} - W_{th})/1000$ where W_{cm} is the center-of-momentum energy and W_{th} is the center-of-momentum threshold energy for the elastic cut. The unit of W is MeV. W is scaled by 1000 in order to reduce numerical error by providing a comparable range ($10^{-2} - 10^2$) for the parameters. Both K_o and K_i are equal to zero at the elastic threshold.

Inelastic K-matrix contributions are needed to describe elastic scattering since the nuclear elastic T-matrix is

$$(T_e)_N = \frac{ImC_e\tilde{K}}{1 - C_e\tilde{K}} \quad (5.6)$$

Table 5-1: Coupling Between K^+N and Inelastic Channels.

K^+N	$K^+\Delta$	K^+^*N
S_{I1}	D_{11}	S_{01}
P_{I1}	P_{11}	P_{01}
P_{I3}	P_{13}	P_{03}
D_{I3}	S_{13}	S_{03}
D_{I5}	D_{15}	D_{05}
F_{I5}	P_{15}	P_{05}
F_{I7}	F_{17}	F_{07}
G_{I7}	D_{17}	D_{07}
G_{I9}	D_{19}	D_{09}

where

$$\tilde{K} = K_e + \frac{C_i K_0^2}{1 - C_i K_i} \quad (5.7)$$

C_i and C_e are the inelastic and elastic parts of the Chew-Mandlestam matrix [ET80, AR85]. The Chew-Mandlestam matrix is a diagonal matrix whose elements are dispersion integrals of phase space factors. It contains the appropriate unitary cuts. Its form is

$$C_l = \int_0^1 dx \frac{x^{l+\frac{1}{2}}}{x - x'} \quad (5.8)$$

where $x' = (W_{cm} - W_{th})/(W_{cm} - W_s)$

and W_{cm} = total center-of-momentum energy,

W_{th} = total threshold center-of-momentum energy

= $M_N + M_K$ for the elastic channel

= $M_\Delta + M_K$ for the isovector inelastic channel

= $M_N + M_{K^*}$ for the isoscalar inelastic channel,

W_s = subtraction point

= $M_N + M_K - 150$ MeV for the elastic channel

= $M_N + M_K + 140$ MeV for either inelastic channel

and

$M_N=938.256$ MeV, $M_K=493.67$ MeV, $M_\Delta=1232.0 - i 51.0$ MeV and

$M_{K^*}=892.0 - i 25.65$ MeV.

Unitarity can be violated slightly beneath the pion-production threshold. In this case, the real part of the K-matrix is taken to construct a unitary T-matrix [Fo88]. This technique has changed from the previous K^+p analysis [AR85].

5.3 Energy-Independent Parametrization

The parameters for the energy-independent parametrization are the phases (δ) and absorption parameters, $\rho \equiv \cos \eta$. These are taken to be linear within an energy bin of the data base. Specifically,

$$\delta = \delta_B + \frac{\partial \delta}{\partial T_B}(T_B - T) \quad (5.9)$$

and

$$\rho = \rho_B + \frac{\partial \rho}{\partial T_B}(T_B - T), \quad (5.10)$$

where T is the lab energy of the incident K^+ and the B subscript indicates that the value is evaluated at the bin energy. The energy derivatives are taken from the energy-dependent analysis. Possible small structures in the phases and absorption parameters are allowed since only the data within the bin affects these values. The parametric errors from the energy-independent parametrization provide the errors in this analysis.

Chapter 6

The Solution

6.1 Isoscalar Solution

Two different techniques are used to find isoscalar energy-dependent solutions up to an incident lab kinetic energy of 1100 MeV. The first technique involves initializing to the single-energy solutions of Hashimoto [Ha84], and Martin and Oades [MO80]. The two single-energy solutions guarantee two independent starting points since they differ greatly. For these cases the K-matrices of the single-energy solutions were calculated and fitted since these values can be fitted easily and simply with the K-matrix initializer. The K-matrix initializer provides several choices of forms, including resonance behavior. The solution acquired from the initialization to the single-energy solution of Martin and Oades will be referred to as solution A; the corresponding solution derived from Hashimoto's single-energy solution will be referred to as solution B.

After searching these initializations to a statistical minimum, parameters which were not used in the search to fit the data were tested. These parameters were started at values which would not alter the current solution. A decrease in χ^2 of 25 was generally required in

order to justify the addition of parameters to those provided in the original initialization. During the searching process, any parameter whose error exceeded its value was removed.

The solutions were then revised by allowing experimental normalizations to vary. Searching with normalization errors changes the partial-wave amplitudes minimally in comparison with the statistical search. Solution A has a χ^2 of 1.96 per data point and used 29 parameters to describe partial-waves through G-waves. Solution B has a χ^2 of 1.89 and also uses 29 parameters for waves through G-waves. Figures 6-1 through 6-4 show the initialization to Hashimoto's larger isoscalar partial-wave amplitudes and the B isoscalar solution (Solution C, see below, is essentially the same as solution B, so only one of our two solutions is shown in Figures 6-1 through 6-4).

The second technique for finding the isoscalar energy-dependent solution consists of utilizing our energy-dependent parametrization to fit successively larger bins of data, starting from zero lab kinetic energy, until the entire energy range is covered. This solution will be referred to as solution C. For example, I started with a bin from 0 to 150 MeV, fitted it, and then added the next bin of width 100 MeV onto it. Each bin typically varies from an energy width of 50 to 100 MeV and consists of approximately 70 to 150 data. The elastic parameters were searched until pion production ensued, at which point parameters which couple in the inelastic contribution were searched. The solution acquired from this technique closely matches solution B. χ^2 per data point of each solution agreed to 0.01. Twenty-nine parameters are used, also. Solutions B and C will be replaced by solution C alone.

At this point, the bins for finding the single-energy solutions for the energy-dependent solutions of A and C were selected. The bins were chosen to coincide with those of a previous isovector analysis [AR85]. This choice is valid since the isoscalar $\Re T$ and $\Im T$ appear linear from the graphs within the regions of each bin. The phases and absorption parameters, ρ , for fitting the data bins were selected if they produced partial-wave amplitudes such that

$$0.5(2J + 1)\Im mT_l > 0.014 \quad \text{or} \quad 0.5(2J + 1)(\Im mT_l - |T|^2) > 0.014 \quad (6.1)$$

where the former and latter relations are proportional to the elastic and inelastic cross sections, respectively. Once a bin at a lower energy is searched, the next higher bin is searched. Partial-wave amplitudes which are important for a bin at a lower energy were retained for the next higher energy bin. The number of parameters in each bin range from a low of 3(solution A) or 4(solution C) for the 125-175 MeV bin to a high of 14(solution A) or 15(solution C) for the 950-1100 MeV bin. The partial-wave amplitudes are too small (Eq. 6.1) at the lowest bin energy.

The single-energy solutions and energy-dependent solutions for the P_{03} of solutions A and C are very close. Each of these single-energy solutions deviated significantly from their respective energy-dependent solutions (see Figures 6-7 and 6-16). The single-energy solutions of the P_{03} cannot be fitted well with our energy-dependent parametrization due to the excessive scatter at low energy of the single-energy solutions. The deviation of the single-energy solutions is probably mostly noise.

6.2 Combined Isoscalar and Isovector Solution

Partial-wave amplitudes from an isovector analysis which extends to an incident lab kinetic energy of 2650 MeV [AR85] were then added to the isoscalar amplitudes obtained in this work. The combined isoscalar and isovector data base was searched statistically and then with the normalization variation allowed. Sixty-three isovector parameters composing partial-waves up to J-waves, and twenty-nine isoscalar parameters composing partial-waves up to G-waves fitted the combined data base. The final χ^2 per data point for the isoscalar and isovector energy-dependent solution A is 1.88 and 1.35, respectively. The corresponding χ^2 for the isoscalar and isovector energy-dependent solution C is 1.87 and 1.35, respectively. The previous isovector and isoscalar energy-dependent solutions changed very little. The isovector single-energy solution, with its more abundant data base, exhibited smaller errors than did the isoscalar single-energy solution.

The effect in χ^2 due to improperly charge correcting the K^+p amplitudes was checked here. (The charge correction is discussed in sections 4.1.3 and 4.2.1.) The χ^2 per data point of $K^+d \rightarrow K^+np$ and $K^+d \rightarrow K^+d$ changes for each solution by 3 % and 8 % , respectively when the K^+p amplitudes are properly charge-corrected and the K^+n improperly. These percentages in variation of χ^2 are larger than the true errors on χ^2 . The $K^+d \rightarrow K^+d$ data comprise 4 % of the data base. All other reactions are properly charge-corrected. A future analysis with a larger, more accurate data base will benefit from correcting the charge correction of the K^+p amplitudes.

Data whose standard deviations were greater than 3σ were pruned from the data base. Approximately fifty-five data were pruned for solutions A and C. Nearly all of the pruned data were the same in each case. The solutions were again searched to a χ^2 minimum. The final χ^2 dropped to nearly 1.21 per data point for solution A and C. The energy-dependent solutions remained essentially the same. A new combined single-energy solution was found with the errors on some of the isoscalar solutions growing larger. The progression of χ^2 per data point for the energy-dependent solutions for each set of data is reviewed in Table 6-1. No data are indicated for solution A until pruning since the data base for solutions A and C are identical until then.

Graphs of the real and imaginary parts of the T-matrix versus incident lab kinetic energy of the K^+ for solution A and C are given in Figures 6-5 through 6-22, respectively. As indicated in section 5.3, the single-energy solutions provide the errors on the T-matrix. The isovector phases are presented only once in Figures 6-23 through 6-31 since they are nearly identical for both solutions. The final isoscalar solutions are very similar with exception of the P_{01} and D_{03} waves. Solution C exhibits a decreasing $\Im m T$ after $T_{lab}=770$ MeV, whereas in solution A it increases. In both isoscalar solutions, the $L=J-\frac{1}{2}$ real partial wave amplitudes are negative, while the $L=J+\frac{1}{2}$ are positive. Since the sign of the $\Re e T$ indicates the sign of the phase shift, the $L=J-\frac{1}{2}$ partial wave amplitudes provide repulsive potential effects and the $L=J+\frac{1}{2}$ attractive. This isoscalar trend of attractiveness and repulsiveness agrees with the single-energy solutions of Hashimoto, and Martin and Oades, with exception

Table 6-1: Progression of χ^2 per data point for each data base.

		Solution C		Solution A	
		χ^2	no. of data	χ^2	no. of data
single	I=0	1.89	1746	1.98	
combined	I=0	1.87	1746	1.88	
	I=1	1.35	3663	1.35	
	total	1.50	5409	1.52	
pruned	I=0	1.41	1692	1.44	1688
	I=1	1.12	3606	1.12	3606
	total	1.21	5298	1.22	5294

of the G_{09} wave of Martin and Oades. No similar trend is currently or has previously been observed in the isovector waves.

Argand diagrams which display $\Im T$ versus $\Re T$ are shown for the larger partial-waves in Figures 6-32 through 6-33 and Figures 6-35 through 6-36. Argand diagrams for the smaller isovector partial-waves are shown in Figures 6-34 and 6-37.

The unitarity circle where $\Im T = |T|^2$ borders the diagram. Thus, the departure of the Argand diagram from the unitarity circle is a measure of the inelasticity of a partial-wave amplitude. In this analysis, P_{01} , D_{03} , P_{11} , S_{11} , D_{13} , and P_{13} show the most inelasticity.

Fits to the isovector and isoscalar σ_{tot} and σ_{in} are shown for solutions A and C in Figures 6-38 through 6-41. The departure of the $K^+p \rightarrow K^+p$ solution from the σ_{in} is an indication of the inconsistency of the σ_{in} with the remainder of the data base.

6.3 Resonances

A resonance is the meta-stable state which forms upon the collision of the incident and target particles. A time delay occurs in the outgoing state due to the lifetime of the resonance. A resonance is characterized by its mass, width, pole position, and angular momentum state. The mass is identified as the center-of-mass energy at which the peak delay of the outgoing particles occurs. The width is related to its lifetime. The pole position provides real and imaginary values related to the mass and width of a resonance providing the pole is close enough to the physical region to cause variation in the scattering amplitudes.

A resonance is normally suggested by the appearance of specific structure in an observable. The angular momentum states are then investigated by reviewing Argand diagrams. Counter-clockwise motion in the Argand diagram is suggestive of resonances. Yet, these structures alone do not prove the existence of a resonance. Once these resonance-like fea-

tures are noted, the characteristics of the suspected resonance are fitted by the Breit-Wigner form and the pole position determined.

A more rigorous test is the analysis of the complex plane. In this analysis the energy-dependent parametrization is analytically continued by letting the center-of-mass energy become complex. A full review of the consequences on our parametrization can be found in John Ford's dissertation [Fo88]. Poles of the T-matrix determine resonances and nearby zeros can suppress or enhance their effect. The location of these entities within the multi-sheeted complex plane determine their effect. If a pole or zero is shielded from the physical region by the inelastic cut (due to $K^+\Delta$ for $I=1$, K^+N for $I=0$), then its effects will be suppressed.

Each of the partial-wave amplitudes which display the counter-clockwise looping behavior have poles, i.e. Z^* resonances, associated with their behavior. These partial waves are the P_{01} , D_{03} , P_{11} , P_{13} , and D_{15} . The topology in the complex plane of these partial waves is shown in Figures 6-42 through 6-48. The locations of the poles and zeros and their residues are tabulated in Table 6-2.

Theories also predict resonance poles for the K^+N system. In fact, de Swart et al. [deS80] apply the spherical MIT bag [DeG75] to predict the ground state $l = 0^- q^4\bar{q}$ multiplet. The states in this multiplet are divided into a total angular momentum of $\frac{1}{2}$, $\frac{3}{2}$, and $\frac{5}{2}$ and parity equal to minus one. The $J = \frac{1}{2}$ states couple to the K^+N S wave channel; the $J = \frac{3}{2}$ and $\frac{5}{2}$ states couple to the K^+N D wave channel. Thus, the $J = \frac{3}{2}$ poles are expected to occur at a lower energy than predicted by theory due to the coupling of the K^+N D-waves to their respective S-wave inelastic channels. Roiesnel [Ro79] also uses a spherical bag and predicts poles for the S-wave K^+N system by applying the P-matrix formalism of Jaffe and Low [JL79]. Lomon [Lo88] finds S-wave resonances by using the Cloudy Bag Model (CBM) for the internal dynamics and a meson exchange potential for the coupled hadronic channels.

Orbitally excited states of the $q^4\bar{q}$ system are calculated with a stringlike bag [deS80]. The

Table 6-2: Poles and Zeroes.

PWA	Status	Solution C				Solution A			
		position(MeV)		Residue		position(MeV)		Residue	
		Re W	-Im W	r(MeV)	$-\phi(\text{deg})$	Re W	-Im W	r(MeV)	$-\phi(\text{deg})$
P_{01}	Pole	1545	177	122	112	1674	194	31	37
	Zero	N/A				1634	222		
D_{03}	Pole	1767	160	33	147	1834	29	9	-69
	Zero	1674	119			N/A			
P_{11}	Pole	1729	113	10	164	1730	114	9	165
	Zero	1747	91			1747	89		
P_{13}	Pole	1812	123	20	64	1810	124	20	63
	Zero	1785	210			1784	213		
D_{15}	Pole	2092	255	18	93	2072	258	19	99
	Zero	1920	26			1926	30		

lowest excitations are the P-wave and F-wave. Nakajima et al. [Na82] fitted their T-matrix resonance amplitudes with a Breit-Wigner formula and a smooth background. All of the previously mentioned resonance masses are given in Table 6-3. Each of the resonance masses are labelled with a reference except those from de Swart et al. [deS80].

The P-matrix results of Corden et al. [Co82] are not presented since poles are found for S and P-waves (using a spherical bag) even though the partial-wave amplitudes are not indicative of resonances. A comparison of the results from this analysis and those of other works is made in section 7.1.

6.4 Scattering Lengths

Previous partial-wave analyses and theoretical studies have calculated isoscalar and isovector scattering lengths for the states $J=L+\frac{1}{2}$ and $J=L-\frac{1}{2}$ which can be compared with this analysis. Most recently, an effective Lagrangian approach which utilizes t-channel σ , ρ , and ω exchanges, and u-channel λ and Σ exchange has been developed [Coh89]. Several values for the coupling g_p^2 , the product $g_{\omega NN}g_{\omega KK}$, and the σ mass were used to calculate sixty scattering lengths for the full model. A second Lagrangian model which uses the t-channel ρ and ω , u-channel λ , and iterative box diagrams with a ΔK intermediate state and ρ exchange has been developed [BH85]. This group also calculates scattering lengths by substituting σ exchange for the group of iterative box diagrams. The form factor for this model was adjusted by fitting the phase shifts of Hashimoto. In a later publication [BH89], they utilize the same t-channel and iterative box diagrams as before, yet add $KK^*\pi$, $KK^*\rho$, $KN\Sigma$, and KNY^* vertices in addition to higher order diagrams involving N, Δ , K, and K^* intermediate states. Finally, three analyses have their scattering lengths extracted in a compilation [DW82]. No scattering lengths from works earlier than 1975 were used. All of these results, in addition to those from this analysis, are tabulated in Table 6-4. Specifically, Table 6-4 shows the scattering lengths a_{0+} , a_{1+} , and a_{1-} (where the subscript refers

Table 6-3: Theoretical Poles.

	Z_1^* (GeV)	Z_0^* (GeV)
S_1	1.78 [Ro79]	$1.705 \pm .01$ [Ro79]
	2.2-2.25 [Lo88]	1.95 [Lo88]
	1.89,2.13	1.70
P_1	1.9	1.72
		1.778 [Na82]
P_3	1.9	1.72
	1.931 [Na82]	
D_3	1.80, 2.16	1.99
		1.907 [Na82]
D_5	2.16	
F_5	1.9	

to $L_{\pm\frac{1}{2}}$) for both isoscalar and isovector states. First appear the scattering lengths obtained from my solutions C and A. Next, the minimum and maximum scattering lengths from the first Lagrangian approach [Coh89] are shown. The values from the second [BH85] and third [BH89] Lagrangian approaches follow. Finally, the results from the other analyses [Cu76, Ma76, 75M1] are shown. A comparison of the results from this analysis and those of other works is made in section 7.1.

6.5 Comparison of observables from each solution

Solutions A and C differ slightly from one another with the major difference being in the P_{01} and D_{03} partial waves. Figures 6-49 through 6-58 show comparisons of the observables versus the incident lab kinetic energy. The greater difference in the solutions is revealed by the spin observables in Figures 6-50 and 6-51 and Figures 6-53 and 6-54. These differences between the solutions A and C are allowed by the large errors in the polarization measurements.

Table 6-4: Scattering Lengths.

	$a_{0+}(fm)$		$a_{1-}(fm^3)$		$a_{1+}(fm^3)$	
	I=1	I=0	I=1	I=0	I=1	I=0
Solution C	-0.33	0.00	-0.13	0.12	0.05	-0.11
Solution A	-0.33	0.00	-0.14	0.00	0.05	-0.11
Lagrangian I(min) [Coh89]	-3.40	0	-0.294	-0.202	-0.236	-0.261
Lagrangian I(max)	-3.21	0	-0.057	0.031	0.000	-0.045
Lagrangian II [BH85]	-0.224	0.008				
Lagrangian II (σ)	0.096	0.568				
Lagrangian III [BH89]	-0.04	-0.28				
Analysis I [Cu76]	-0.28		-0.038		0.019	
Analysis II [Ma76]	-0.33	0.02				
Analysis III [75M1]	-0.32	-0.035	-0.032	0.086	0.021	-0.019

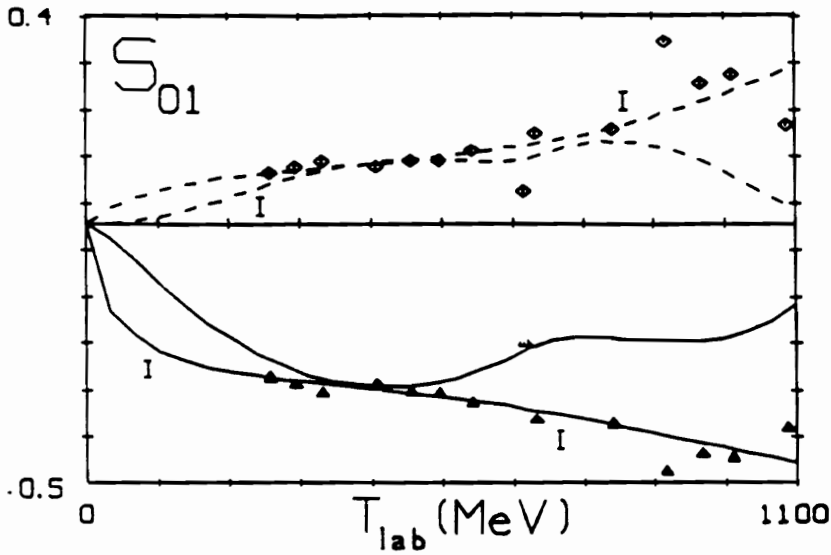


Figure 6-1: Initialization to Hashimoto's S_{01} single-energy solution and solution B versus T_{lab} . Triangles and diamonds represent the $\Re T$ and $\Im T$, respectively, of Hashimoto. The initialization is denoted by I and the B isoscalar solution is unmarked.

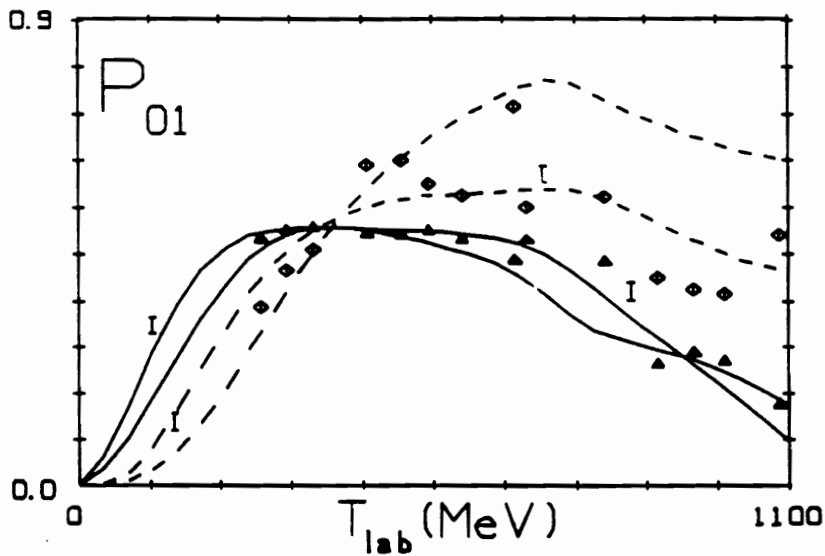


Figure 6-2: Initialization to Hashimoto's P_{01} single-energy solution and solution B versus T_{lab} . For further information, see the comments in the caption of Figure 6.1.

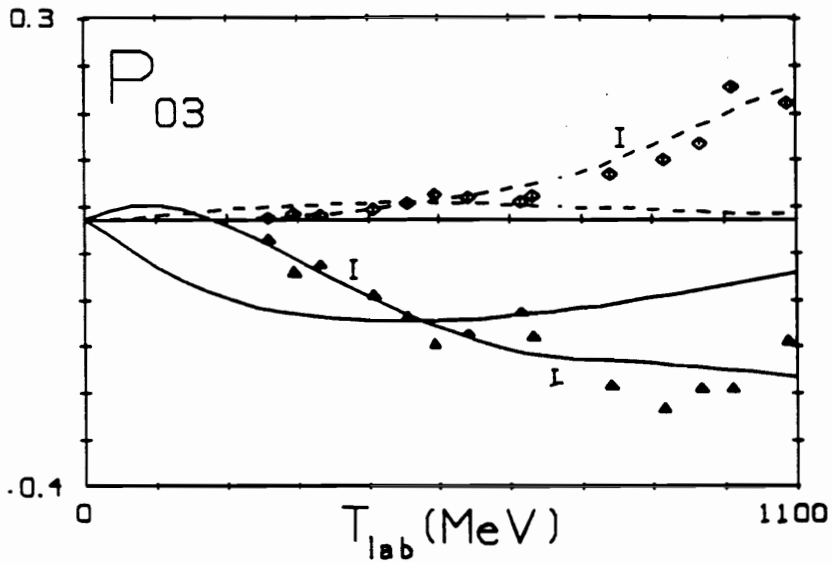


Figure 6-3: Initialization to Hashimoto's P_{03} single-energy solution and solution B versus T_{lab} . For further information, see the comments in the caption of Figure 6.1.

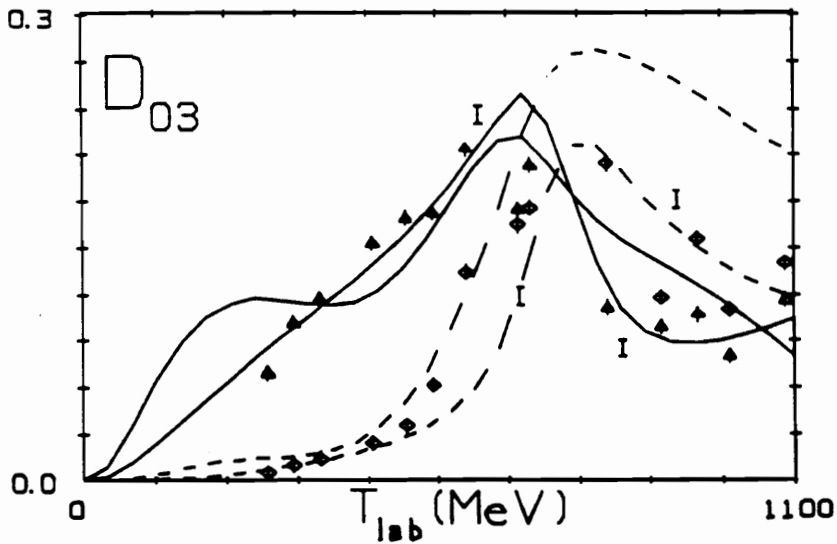


Figure 6-4: Initialization to Hashimoto's D_{03} single-energy solution and solution B versus T_{lab} . For further information, see the comments in the caption of Figure 6.1.

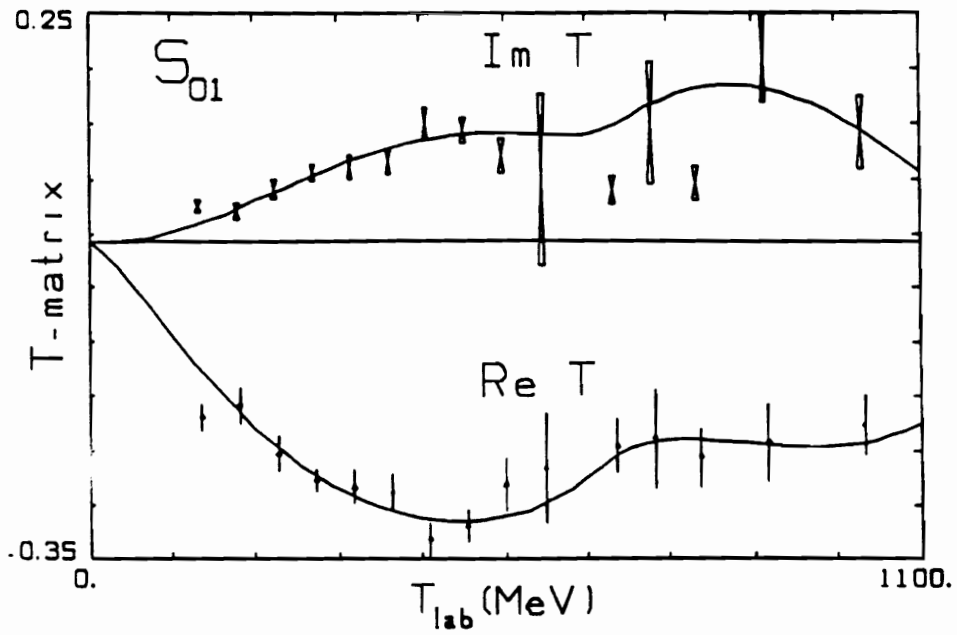


Figure 6-5: S_{01} T-matrix for solution A versus T_{lab} .

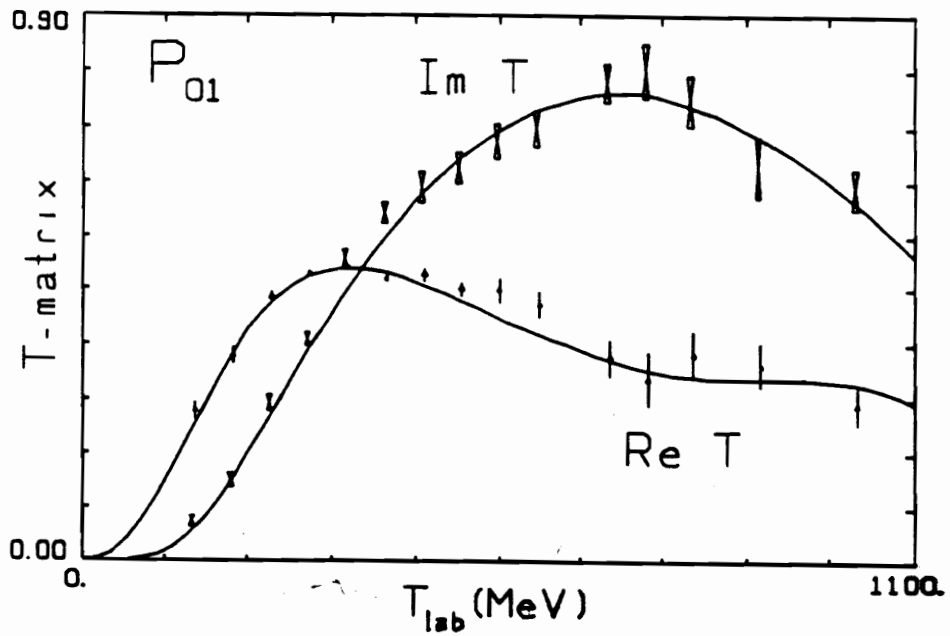


Figure 6-6: P_{01} T-matrix for solution A versus T_{lab} .

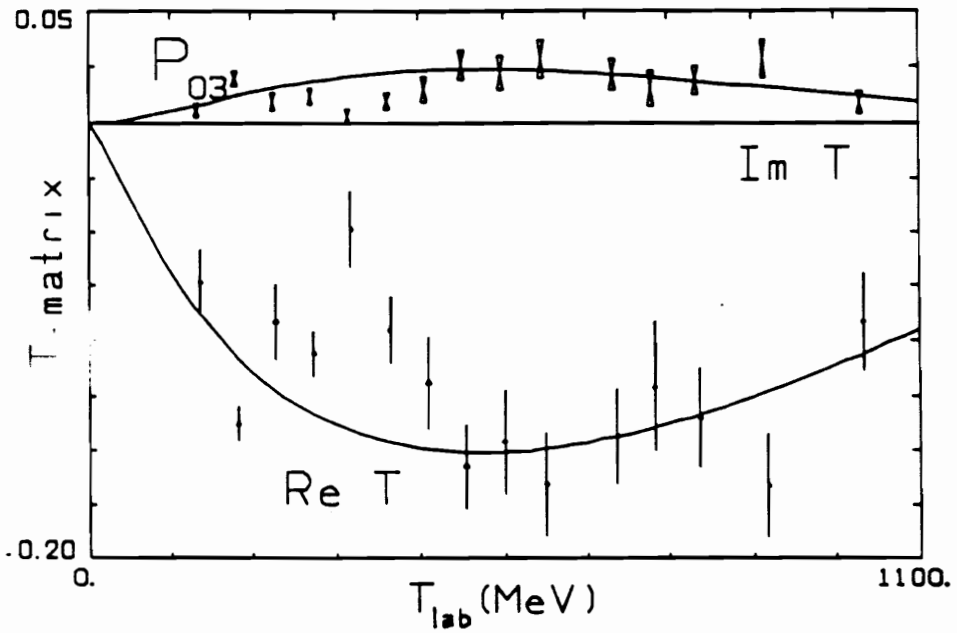


Figure 6-7: P_{03} T-matrix for solution A versus T_{lab} .

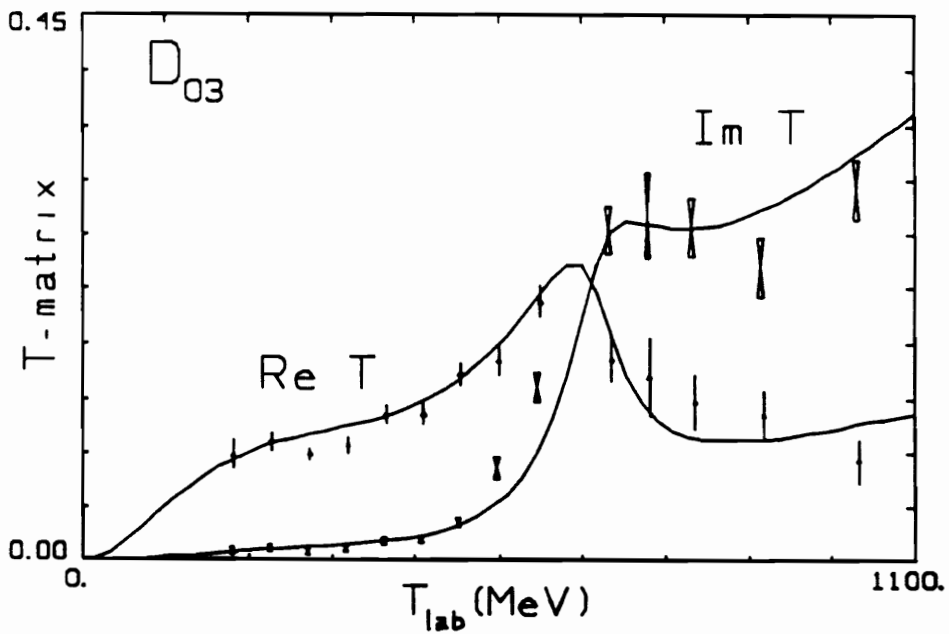


Figure 6-8: D_{03} T-matrix for solution A versus T_{lab} .

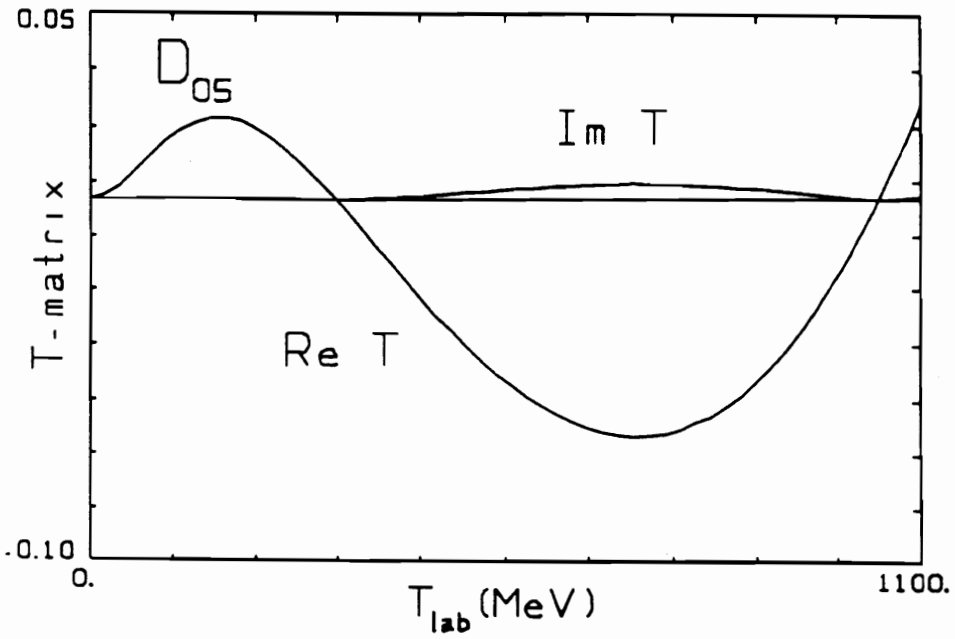


Figure 6-9: D_{05} T-matrix for solution A versus T_{lab} .

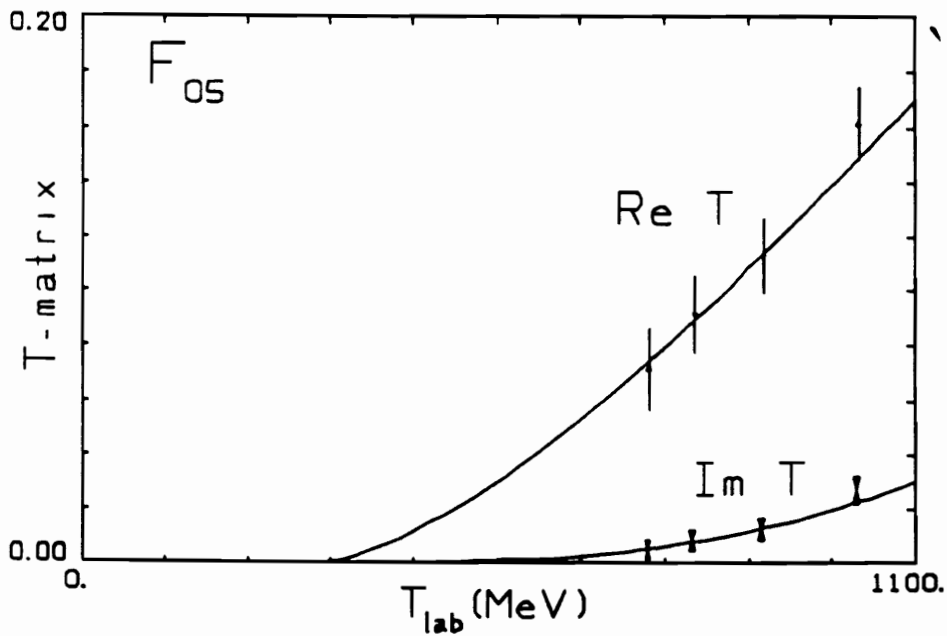


Figure 6-10: F_{05} T-matrix for solution A versus T_{lab} .

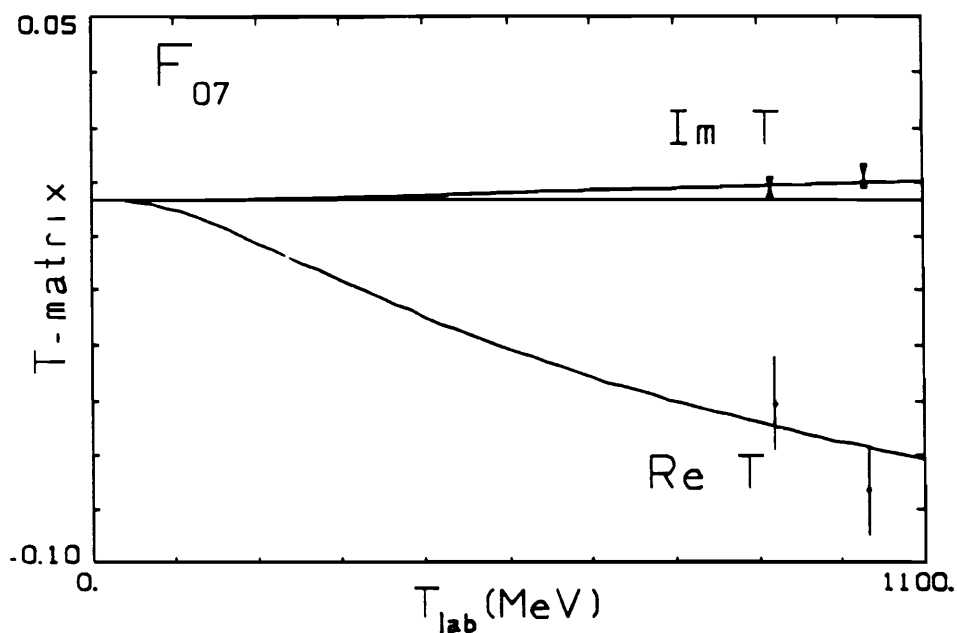


Figure 6-11: F_{07} T-matrix for solution A versus T_{lab} .

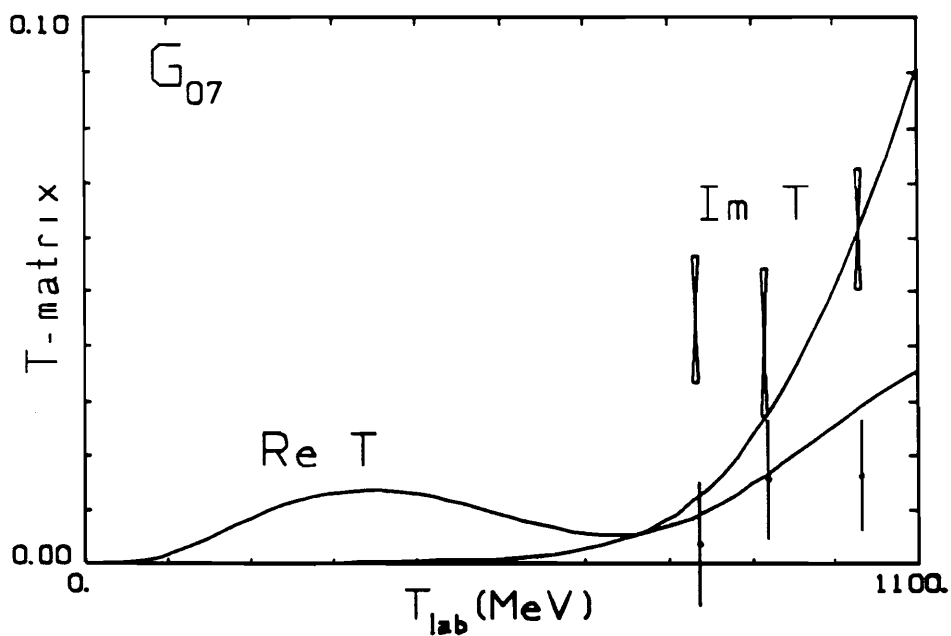


Figure 6-12: G_{07} T-matrix for solution A versus T_{lab} .

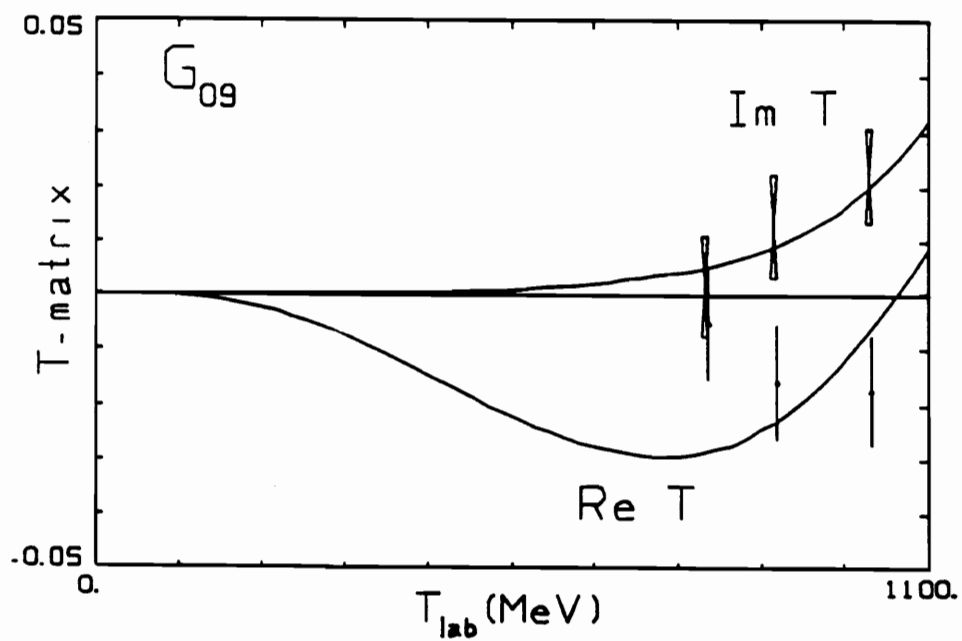


Figure 6-13: G_{09} T-matrix for solution A versus T_{lab} .

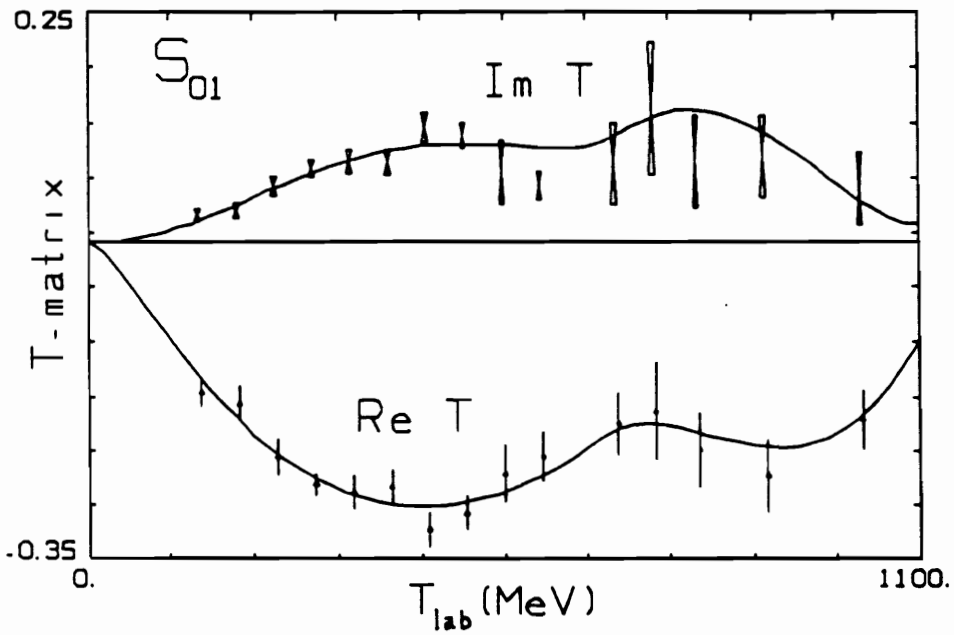


Figure 6-14: S_{01} T-matrix for solution C versus T_{lab} .

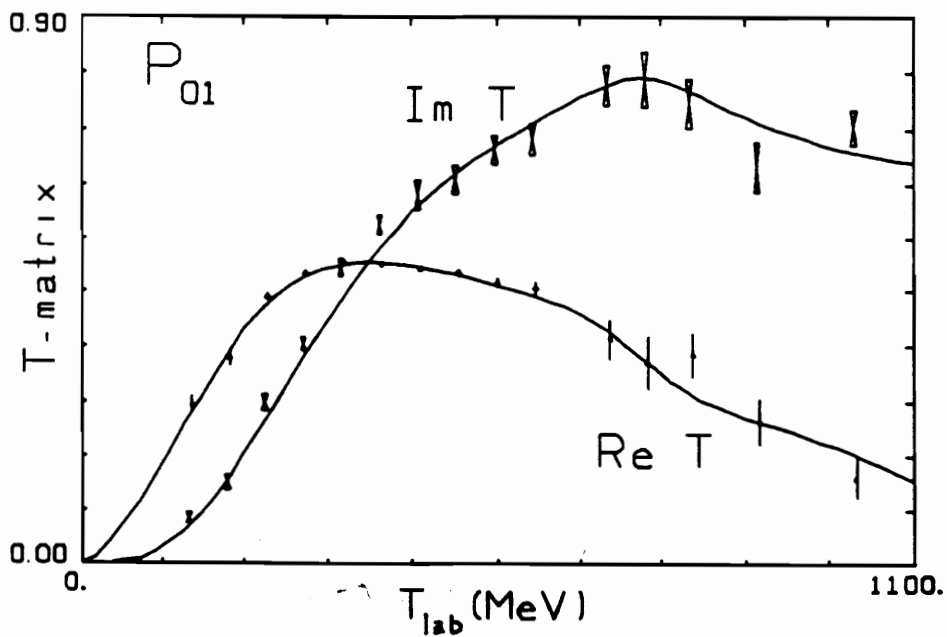


Figure 6-15: P_{01} T-matrix for solution C versus T_{lab} .

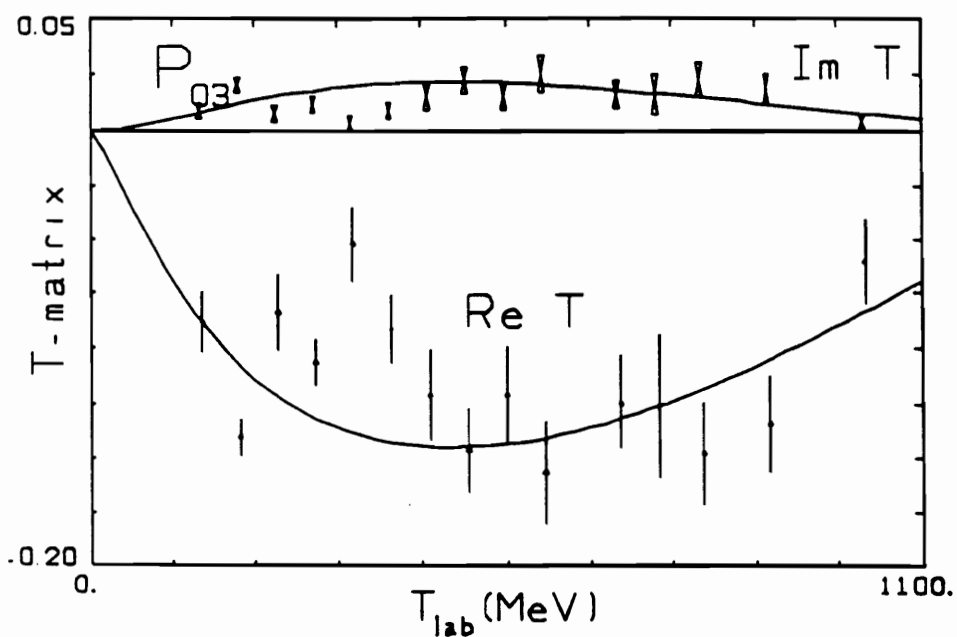


Figure 6-16: P_{03} T-matrix for solution C versus T_{lab} .

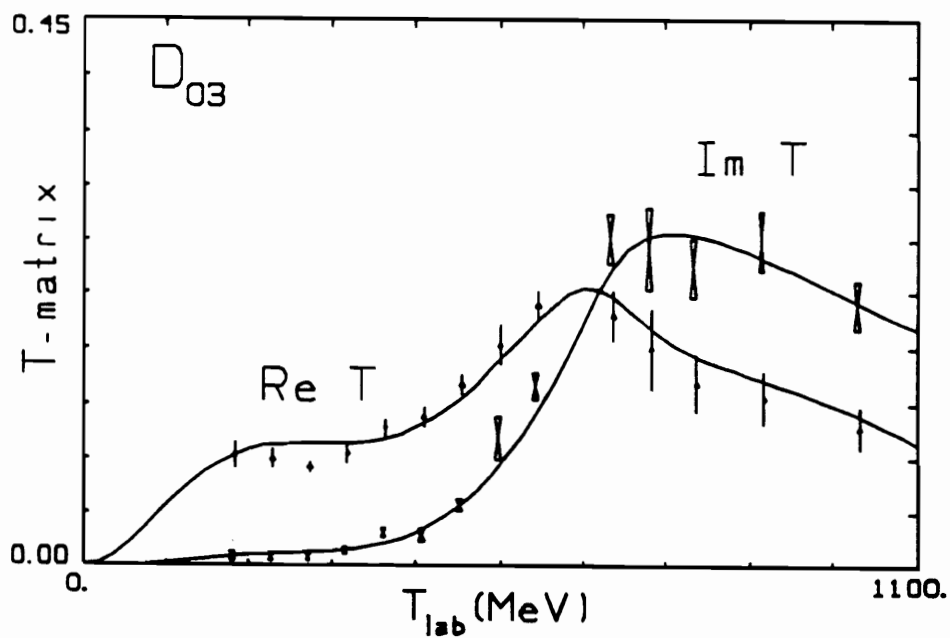


Figure 6-17: D_{03} T-matrix for solution C versus T_{lab} .

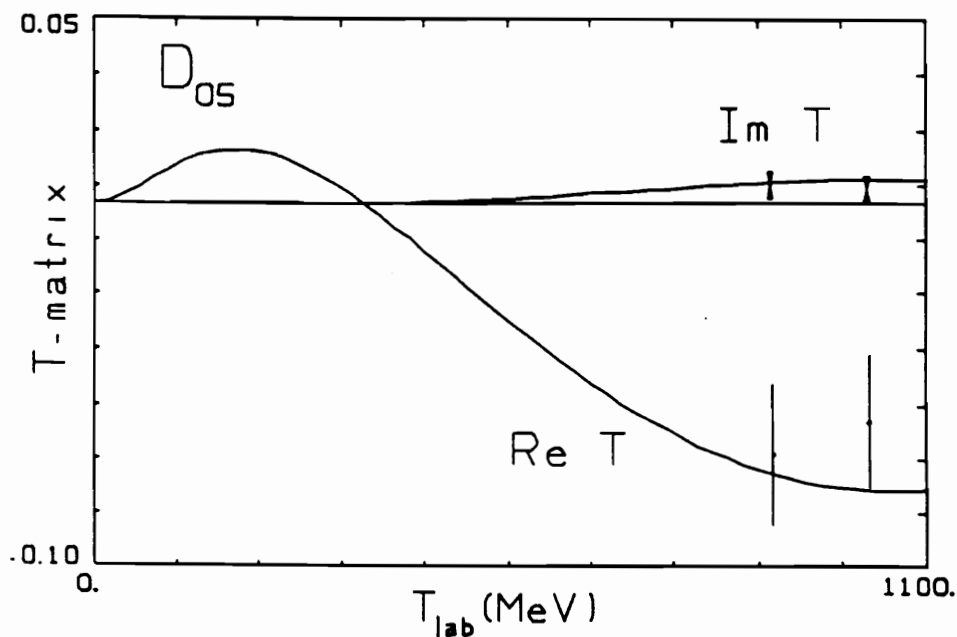


Figure 6-18: D_{05} T-matrix for solution C versus T_{lab} .

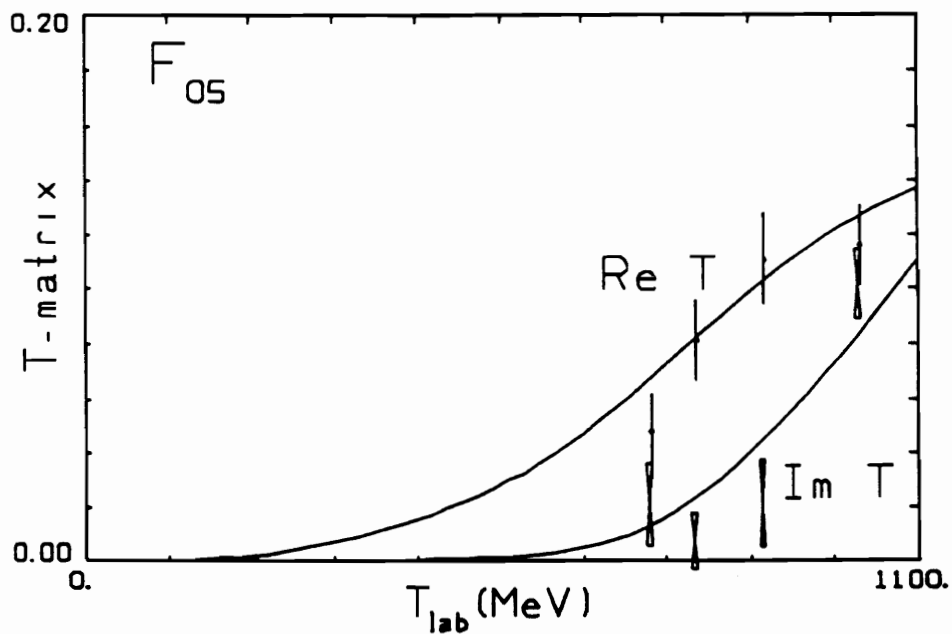


Figure 6-19: F_{05} T-matrix for solution C versus T_{lab} .

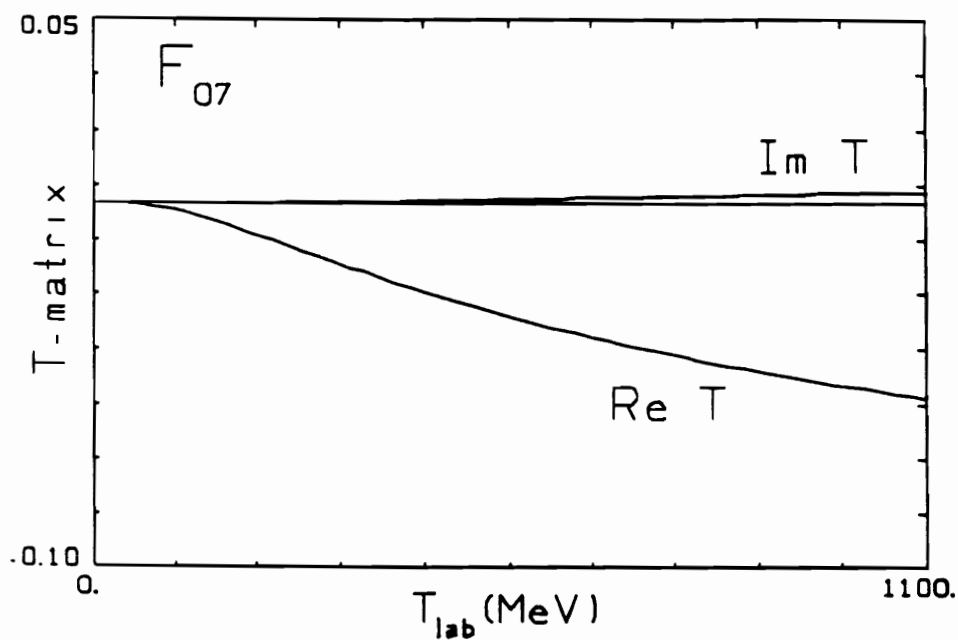


Figure 6-20: F_{07} T-matrix for solution C versus T_{lab} .

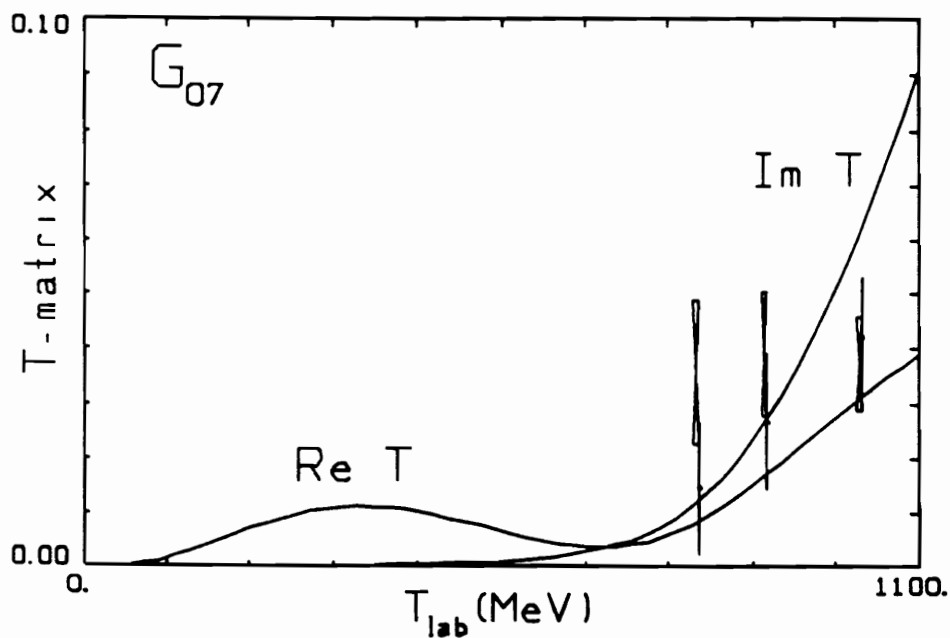


Figure 6-21: G_{07} T-matrix for solution C versus T_{lab} .

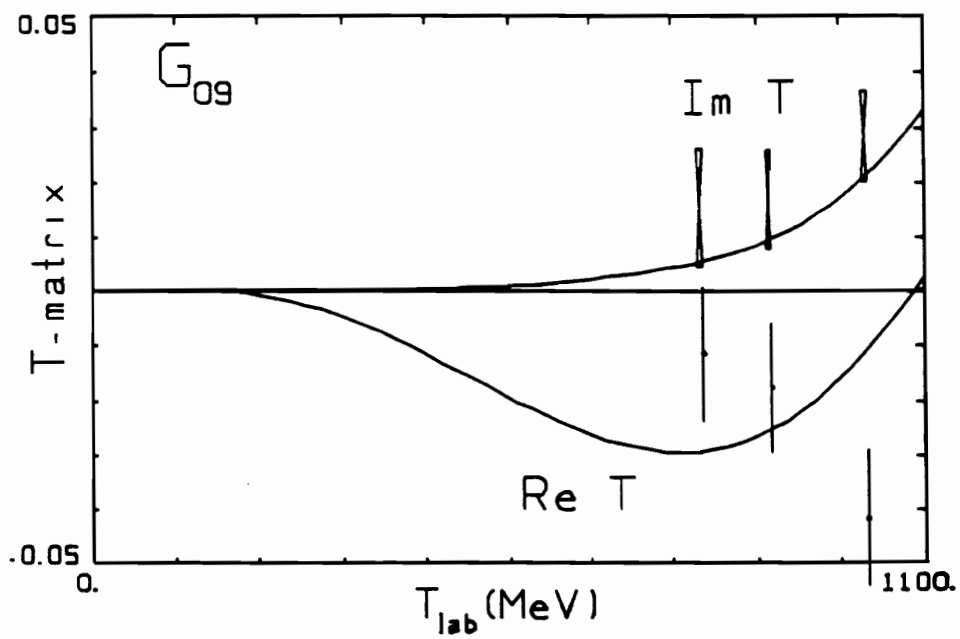


Figure 6-22: G_{09} T-matrix for solution C versus T_{lab} .

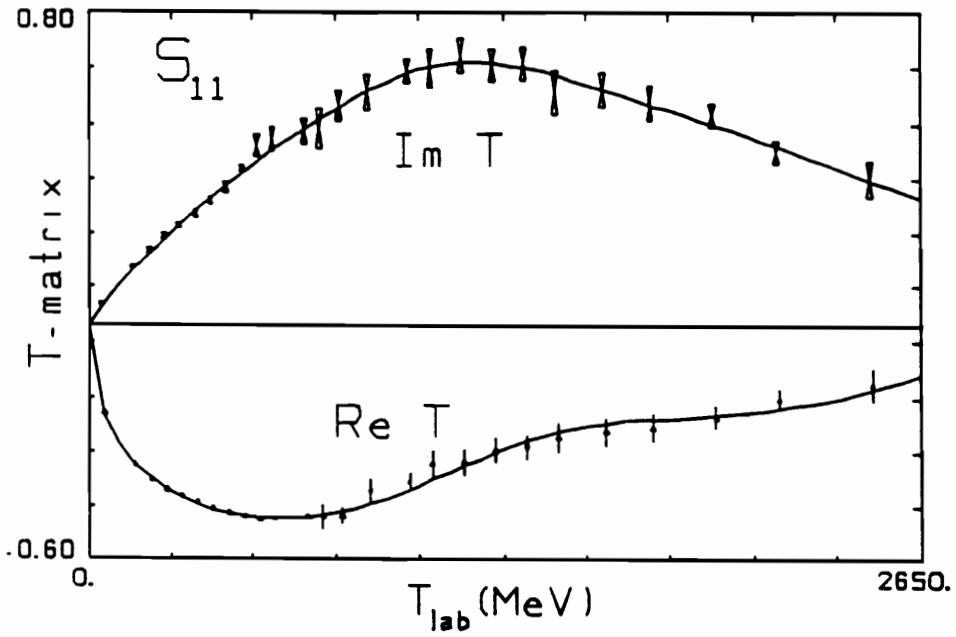


Figure 6-23: S_{11} T-matrix versus T_{lab} .

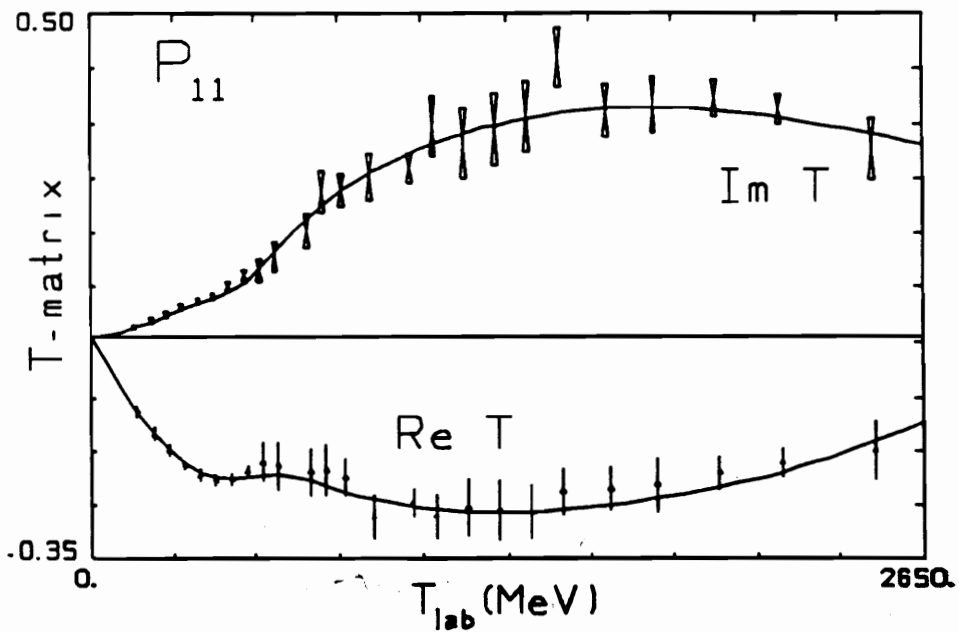


Figure 6-24: P_{11} T-matrix versus T_{lab} .

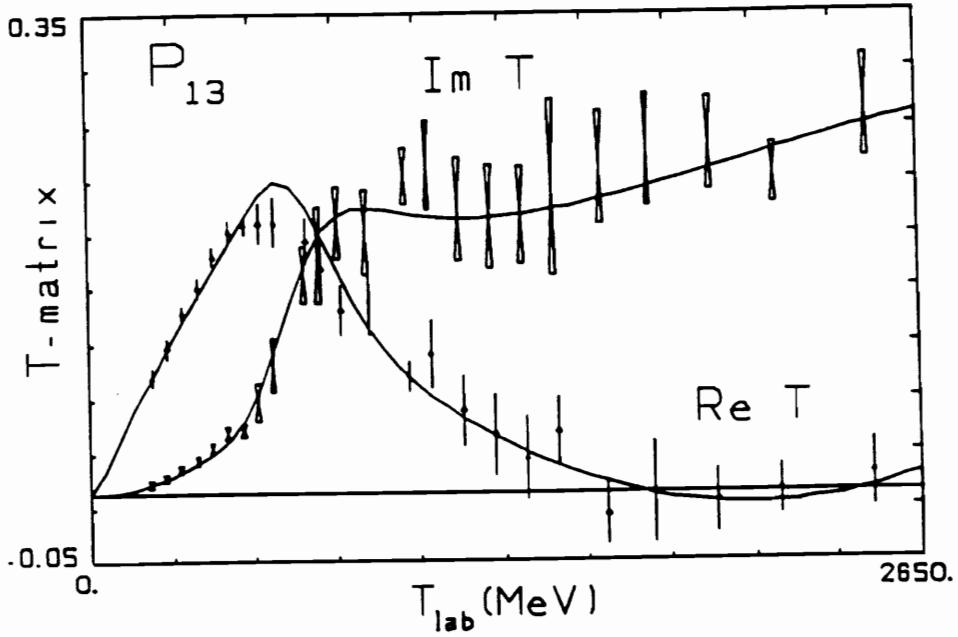


Figure 6-25: P_{13} T-matrix versus T_{lab} .

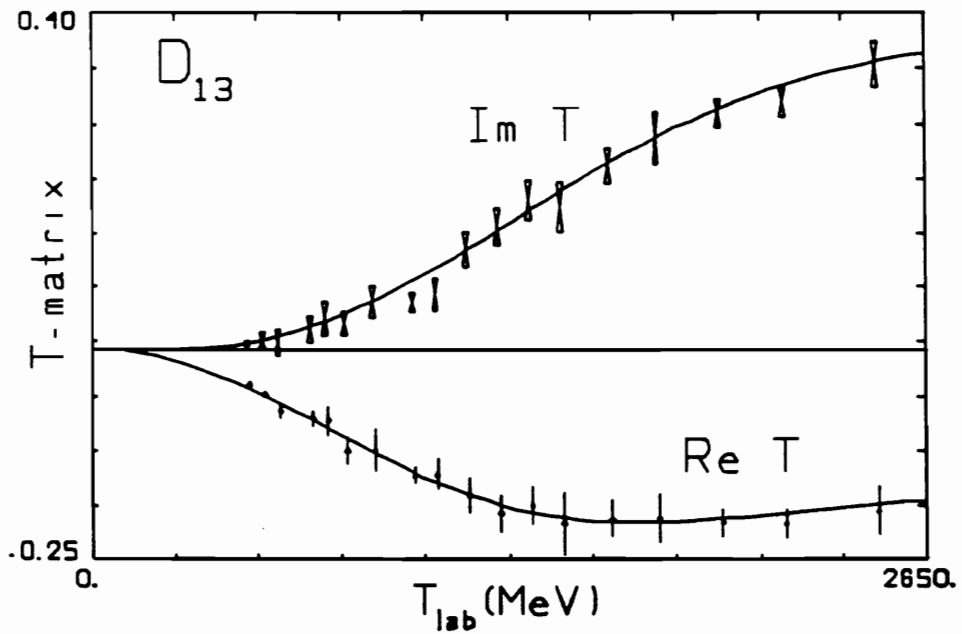
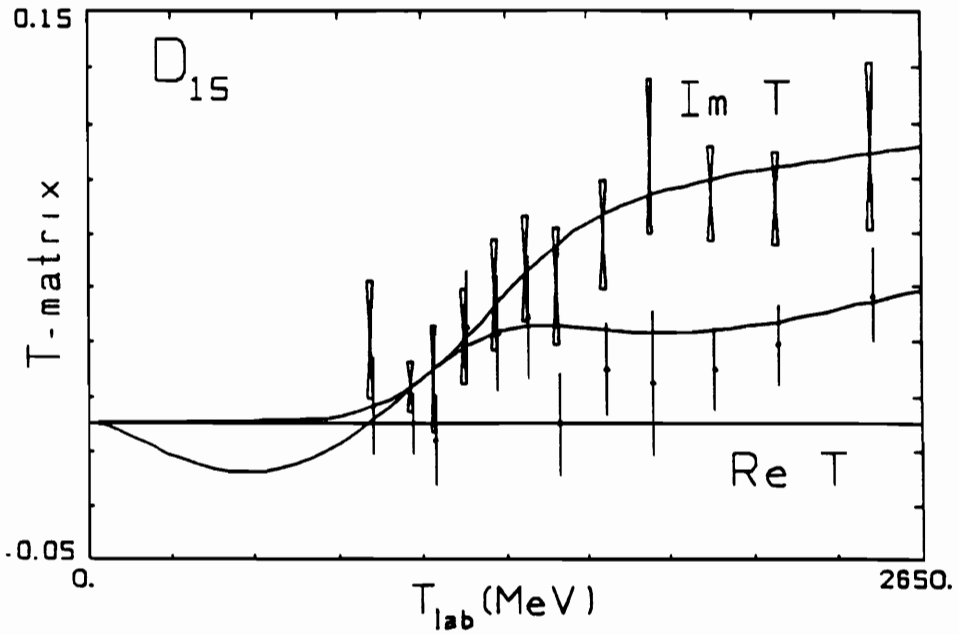
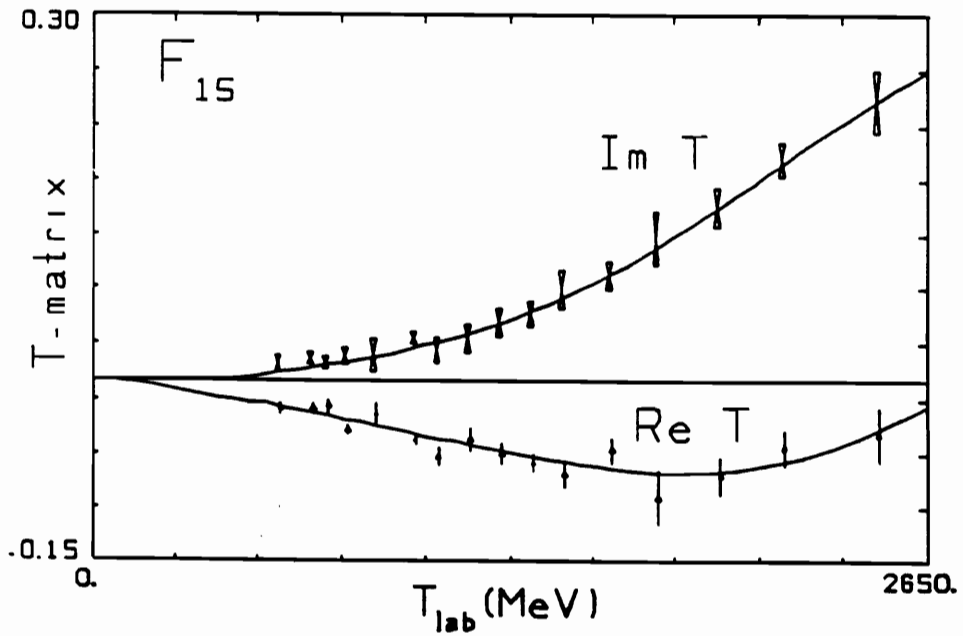
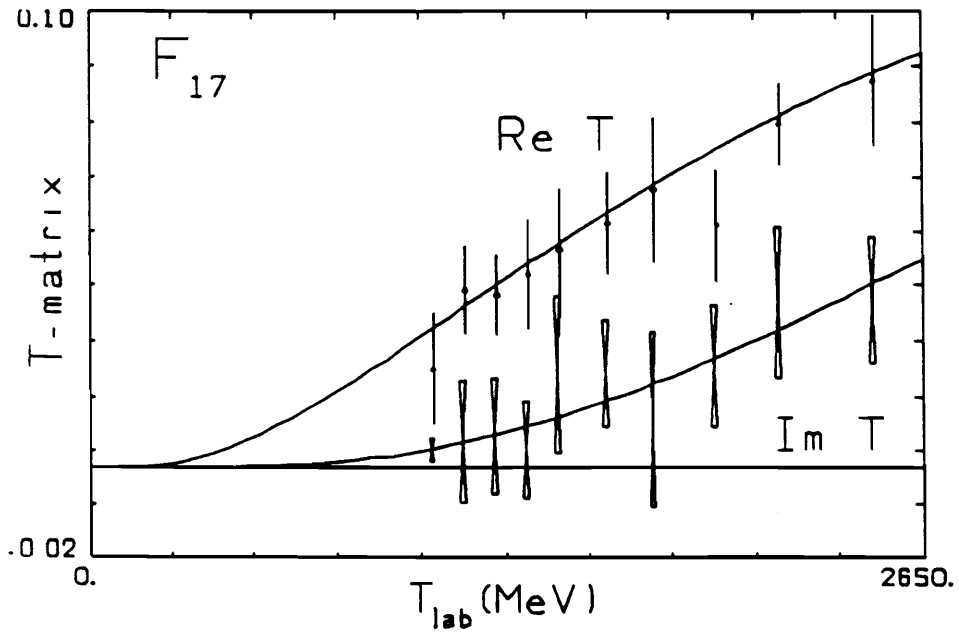
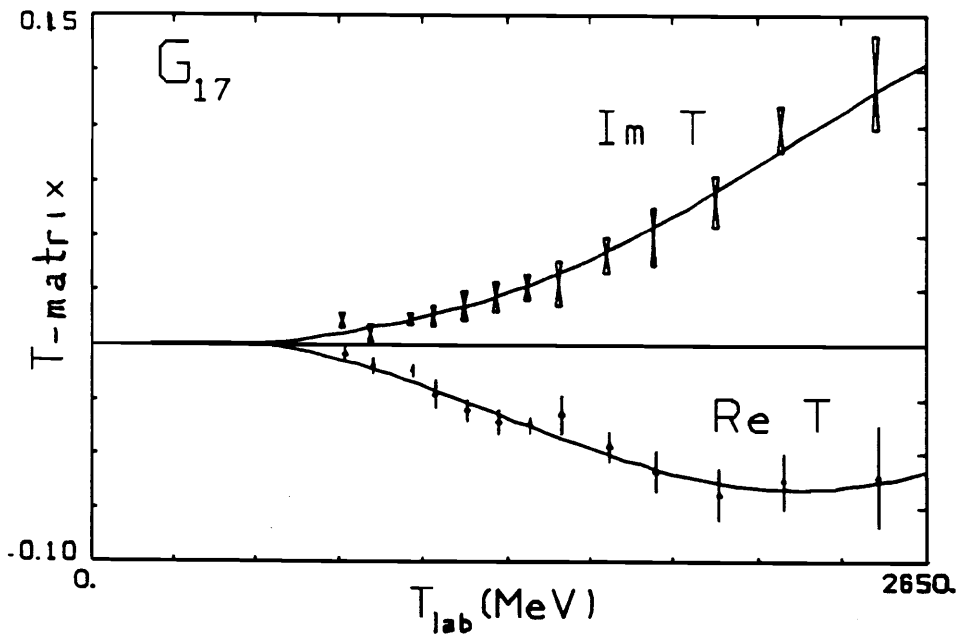


Figure 6-26: D_{13} T-matrix versus T_{lab} .

Figure 6-27: D_{15} T-matrix versus T_{lab} .Figure 6-28: F_{15} T-matrix versus T_{lab} .

Figure 6-29: F_{17} T-matrix versus T_{lab} .Figure 6-30: G_{17} T-matrix versus T_{lab} .

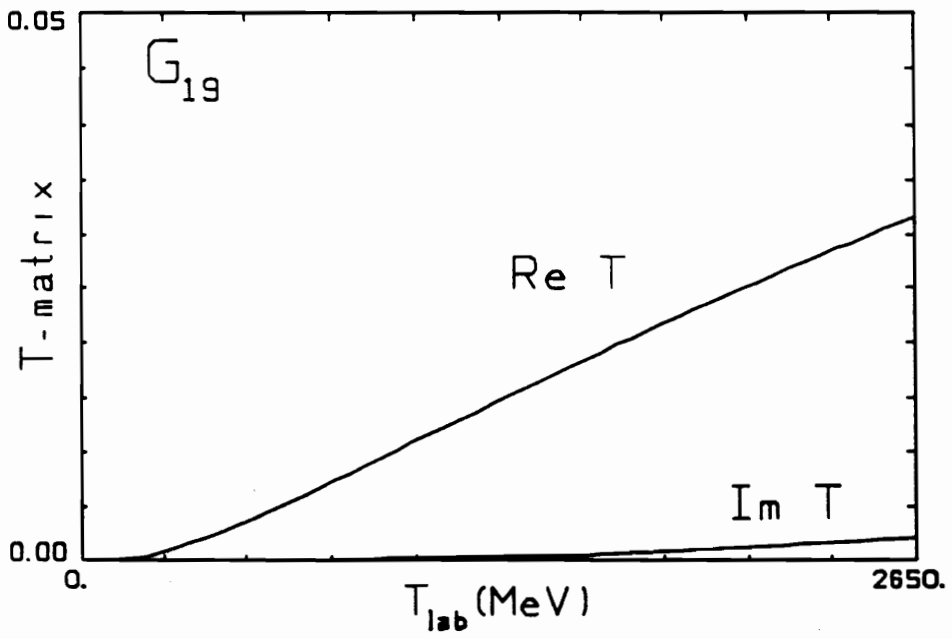


Figure 6-31: G_{19} T-matrix versus T_{lab} .

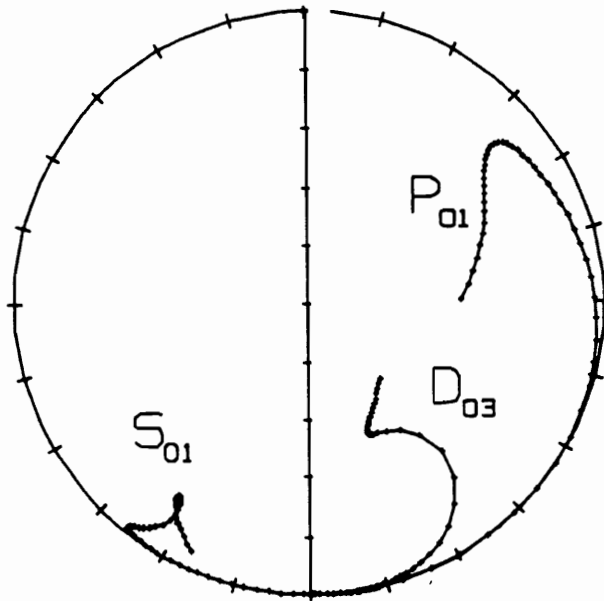


Figure 6-32: Argand diagrams of larger isoscalar partial-waves for solution A.

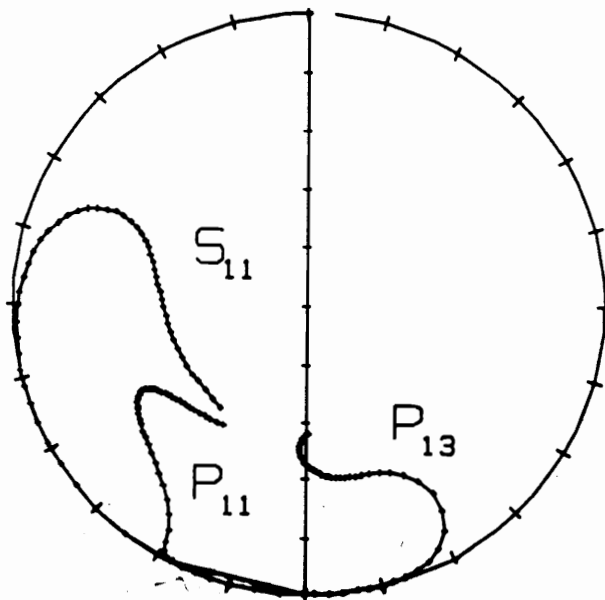


Figure 6-33: Argand diagrams of larger isovector partial-waves for solution A.

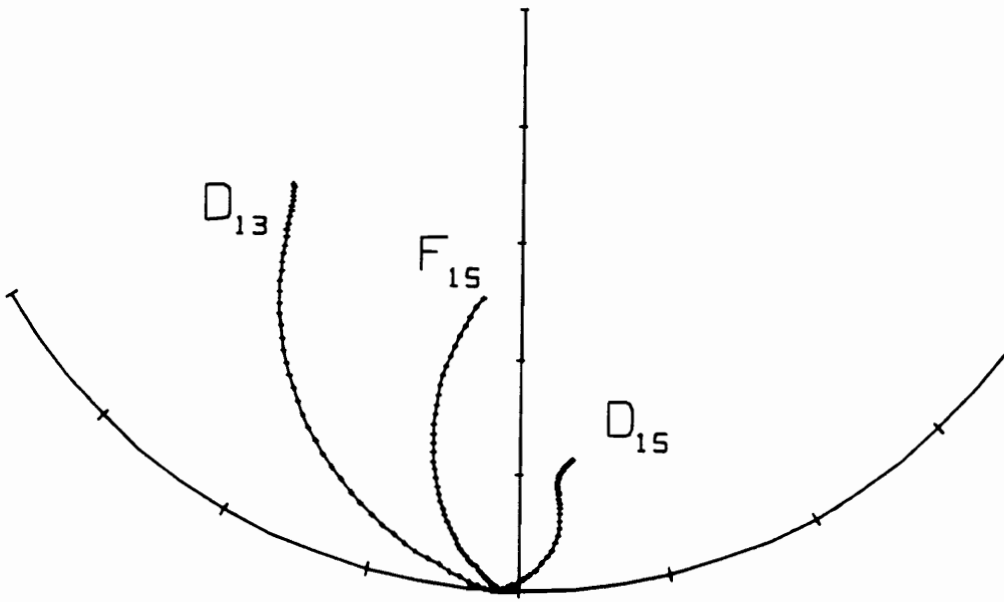


Figure 6-34: Argand diagrams of smaller isovector partial-waves for solution A.

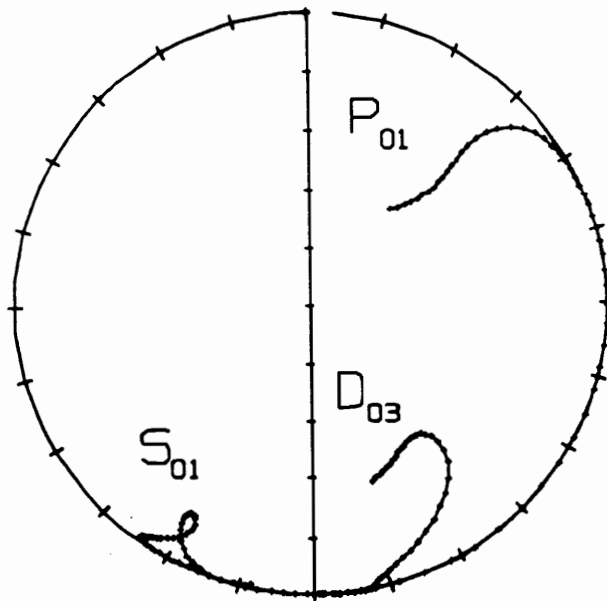


Figure 6-35: Argand diagrams of larger isoscalar partial-waves for solution C.

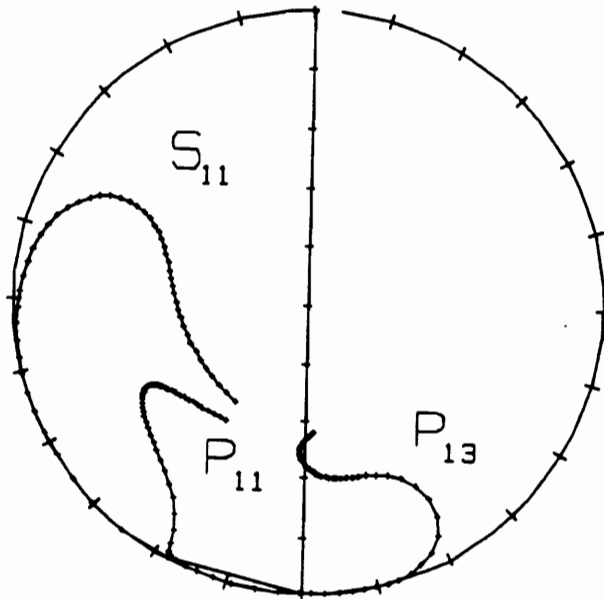


Figure 6-36: Argand diagrams of larger isovector partial-waves for solution C.

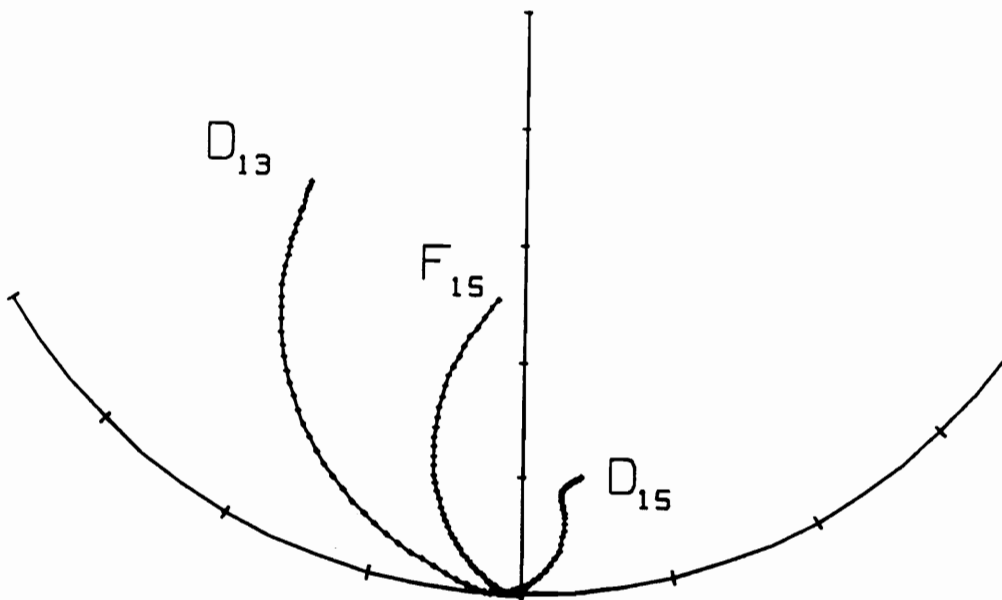


Figure 6-37: Argand diagrams of smaller isovector partial-waves for solution C.

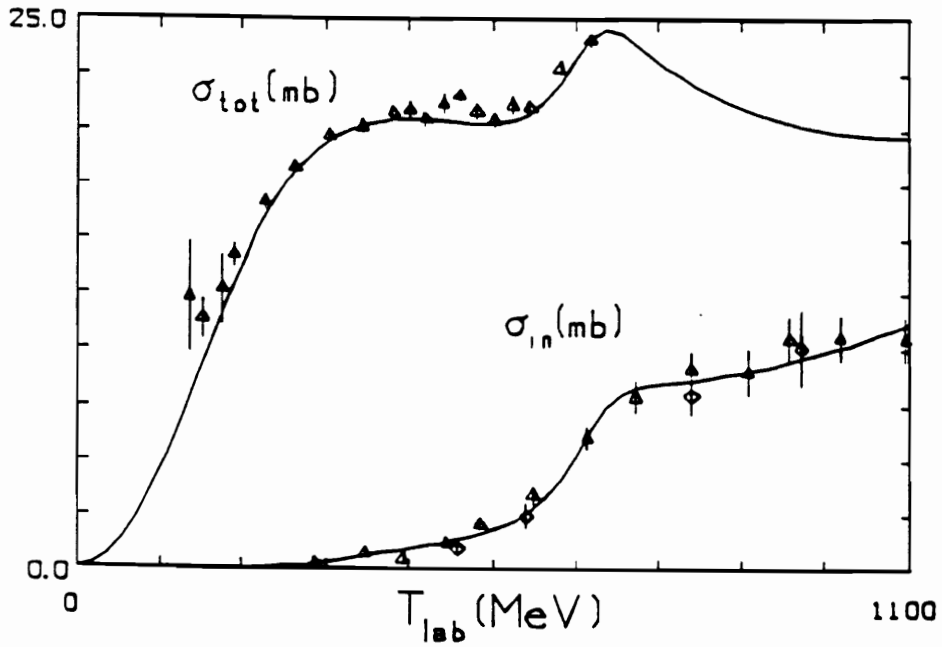


Figure 6-38: Isoscalar cross sections of solution A versus T_{lab} .

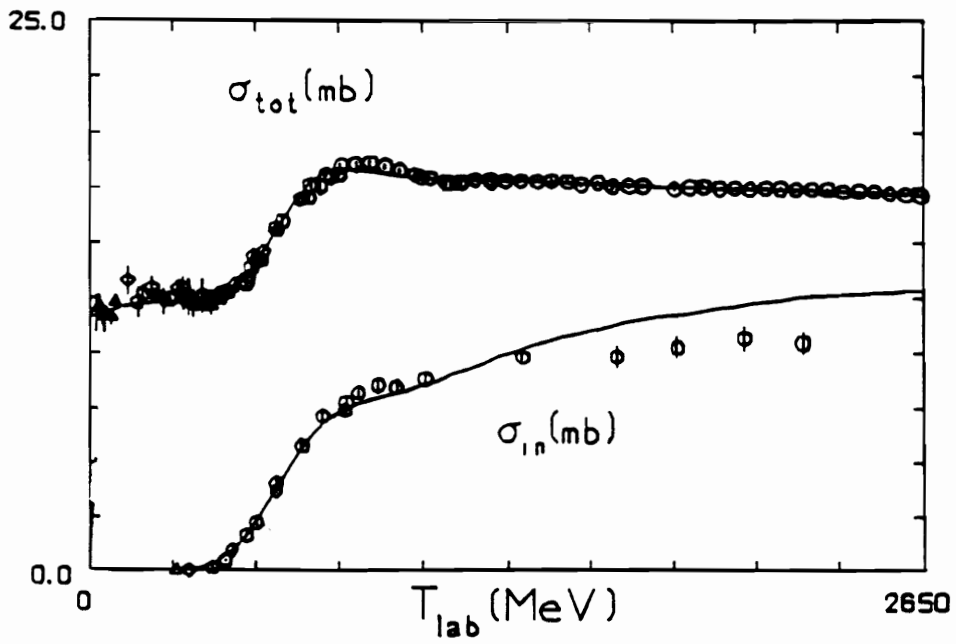


Figure 6-39: Isovector cross sections of solution A versus T_{lab} .

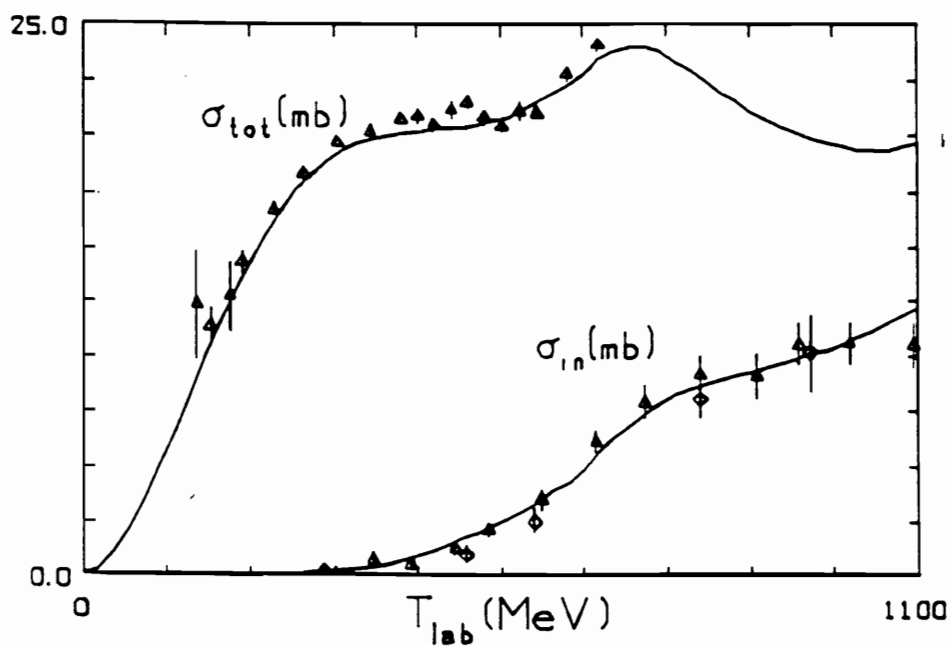


Figure 6-40: Isoscalar cross sections of solution C versus T_{lab} .

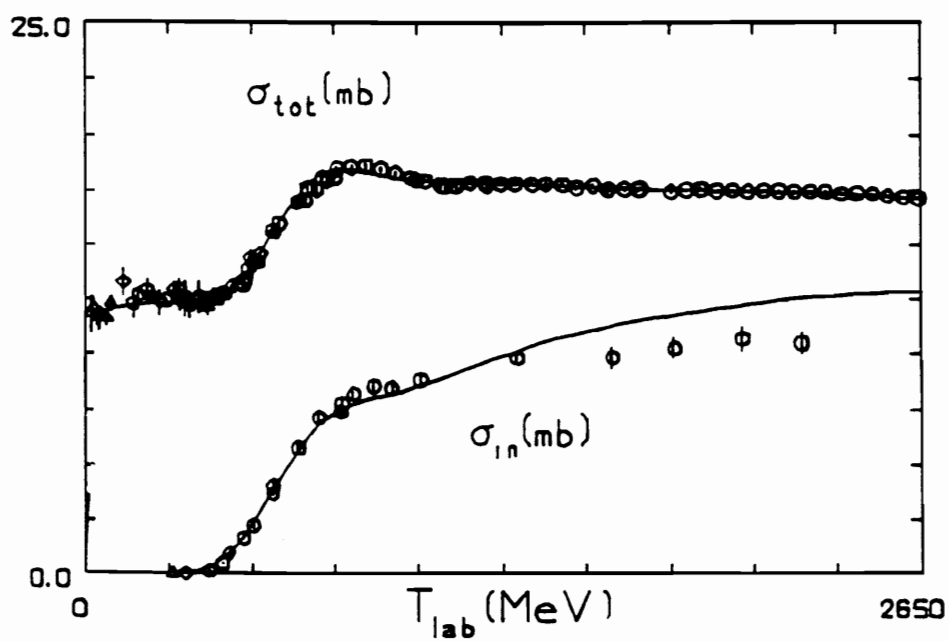


Figure 6-41: Isovector cross sections of solution C versus T_{lab} .

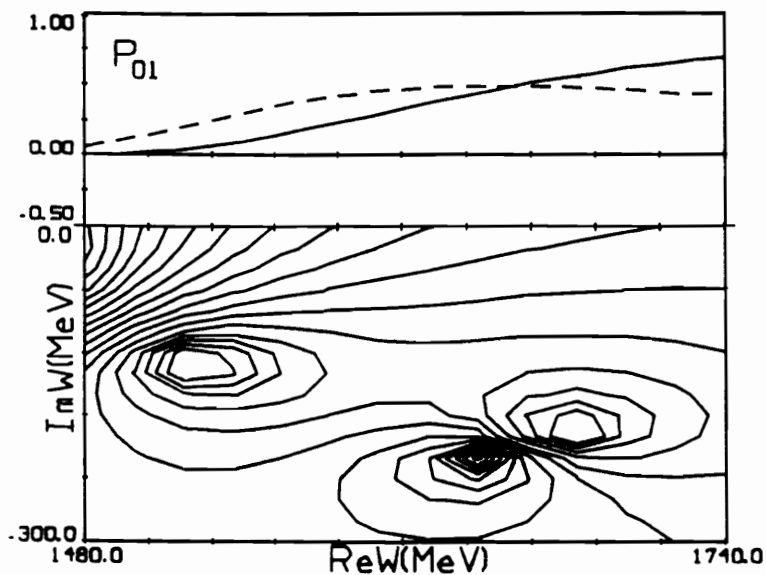


Figure 6-42: Complex plane contour plot of P_{01} for solution A versus W_{cm} . See Table 6.2 for the locations of poles and zeros in the complex plane.

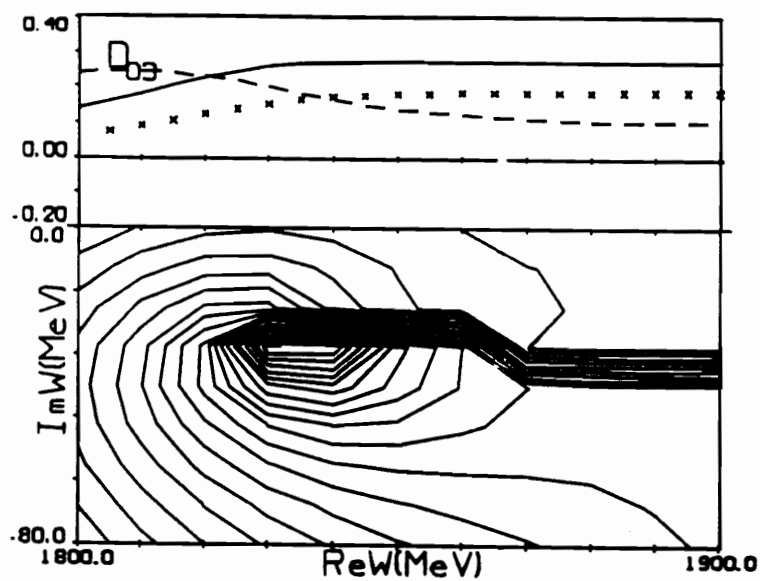


Figure 6-43: Complex plane contour plot of D_{03} for solution A versus W_{cm} . The set of parallel lines indicates the branch cut. See Table 6.2 for the locations of poles and zeros in the complex plane.

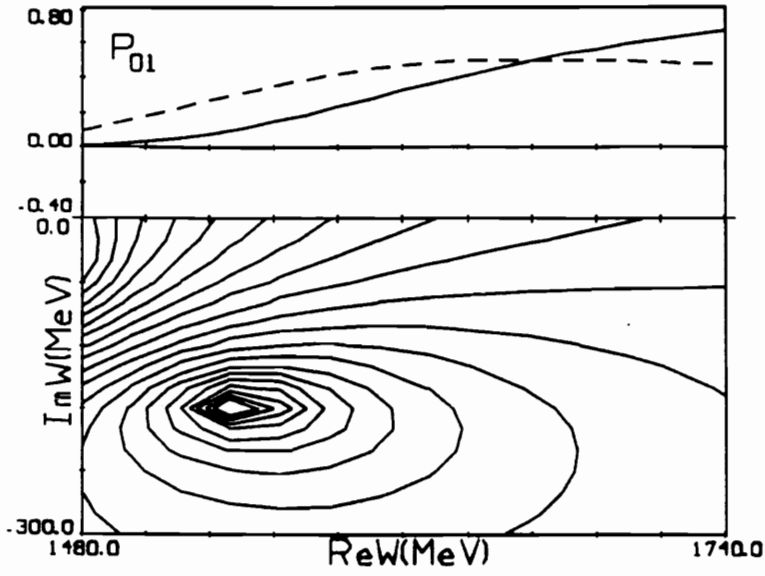


Figure 6-44: Complex plane contour plot of P_{01} for solution C versus W_{cm} . See Table 6.2 for the locations of poles and zeros in the complex plane.

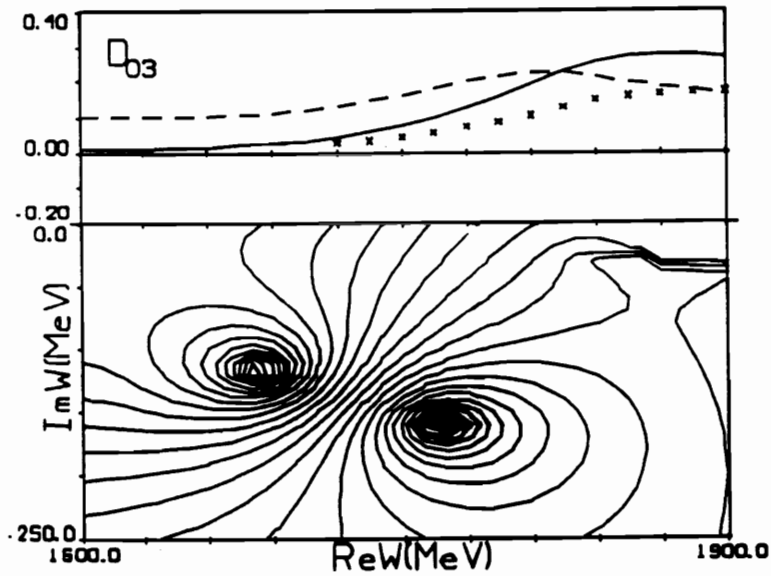


Figure 6-45: Complex plane contour plot of D_{03} for solution C versus W_{cm} . See Table 6.2 for the locations of poles and zeros in the complex plane.

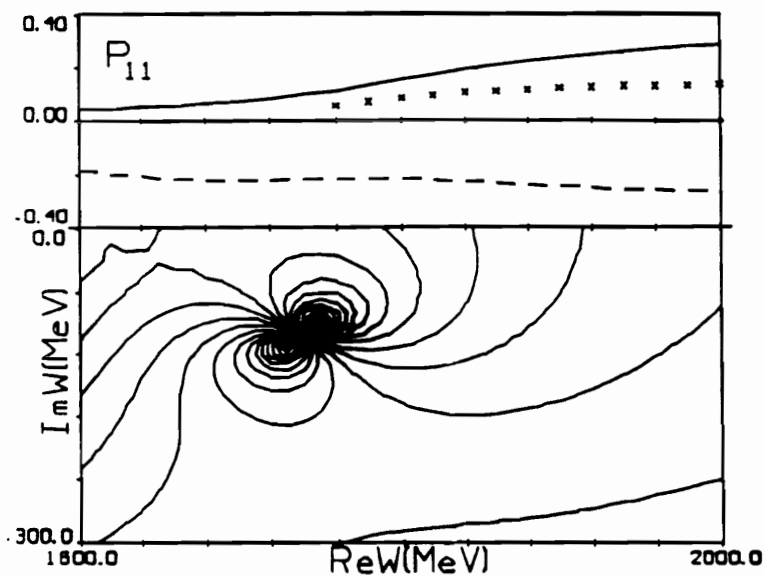


Figure 6-46: Complex plane contour plot of P_{11} for solution C versus W_{cm} . See Table 6.2 for the locations of poles and zeros in the complex plane.

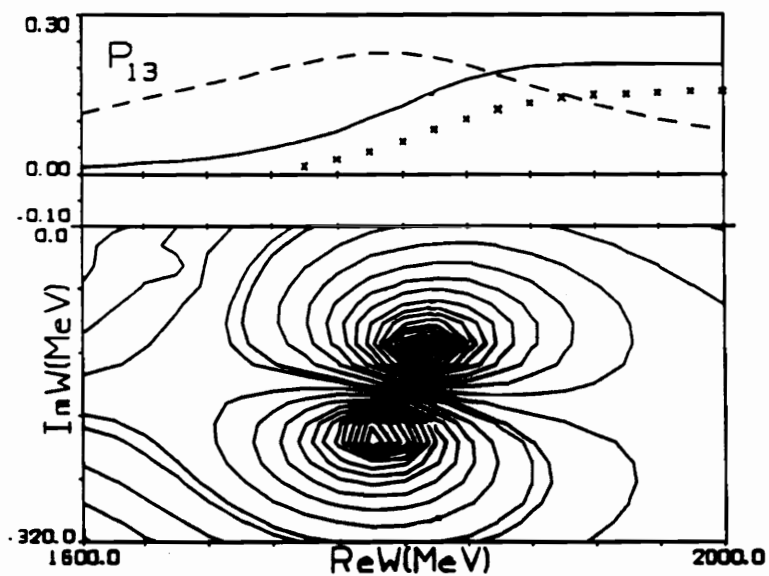


Figure 6-47: Complex plane contour plot of P_{13} for solution C versus W_{cm} . See Table 6.2 for the locations of poles and zeros in the complex plane.

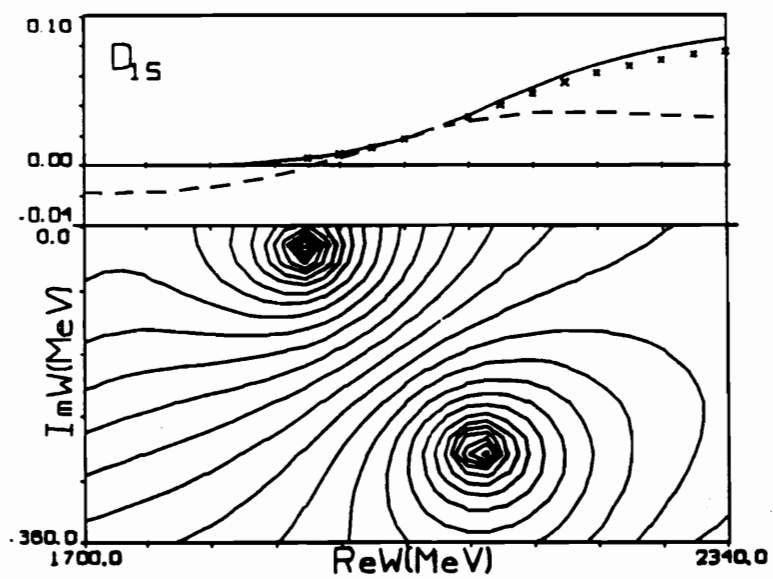


Figure 6-48: Complex plane contour plot of D_{15} for solution C versus W_{cm} . See Table 6.2 for the locations of poles and zeros in the complex plane.

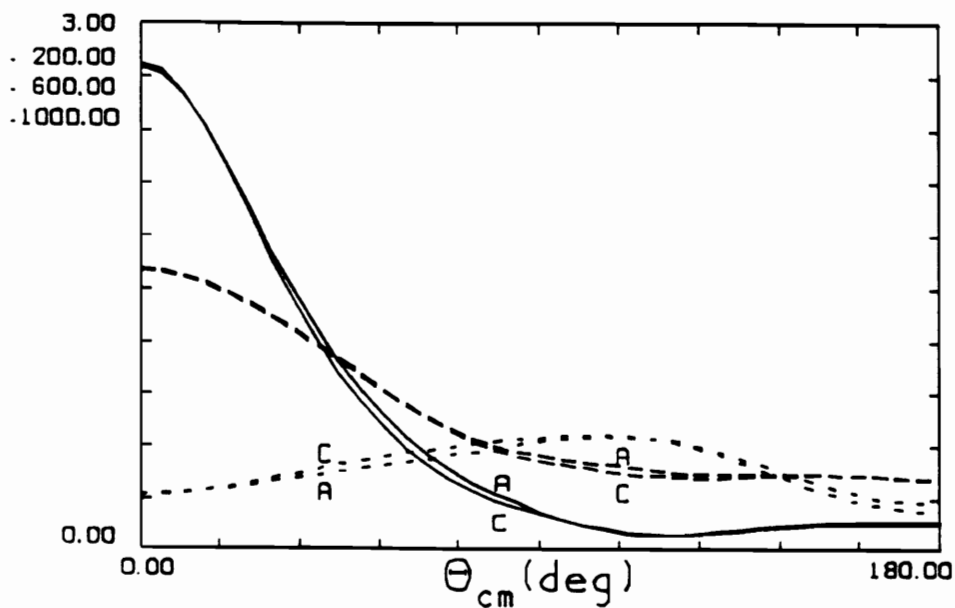


Figure 6-49: $\sigma(\theta)$ of $K^+n \rightarrow K^+n$ for solutions A and C. The solid line indicates $T_{lab} = 1000$ MeV; the longer dash in the dashed line indicates the higher energy.

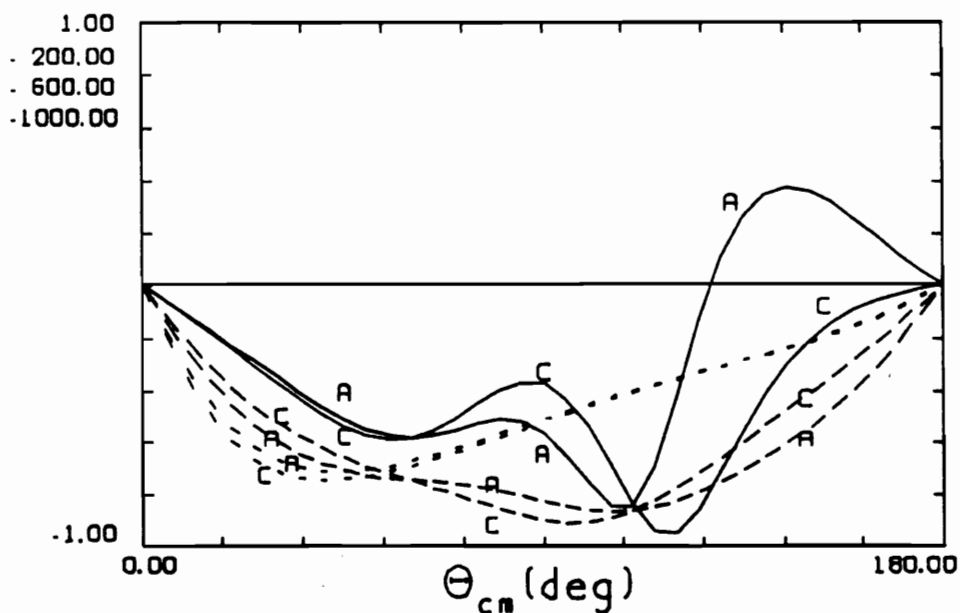


Figure 6-50: $P(\theta)$ of $K^+n \rightarrow K^+n$ for solutions A and C. The solid line indicates $T_{lab} = 1000$ MeV; the longer dash in the dashed line indicates the higher energy.

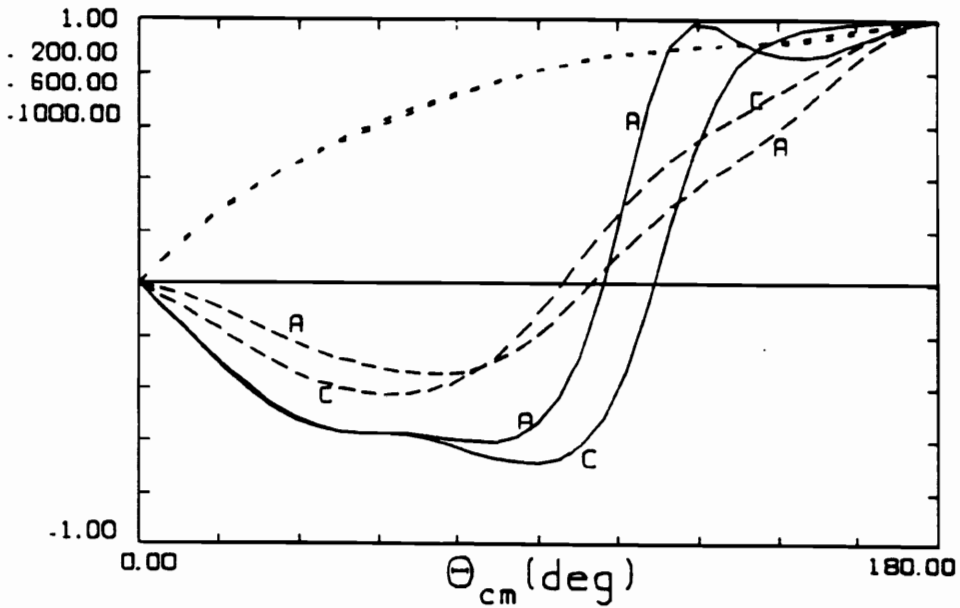


Figure 6-51: $R(\theta)$ of $K^+n \rightarrow K^+n$ for solutions A and C. The solid line indicates $T_{lab} = 1000$ MeV; the longer dash in the dashed line indicates the higher energy.

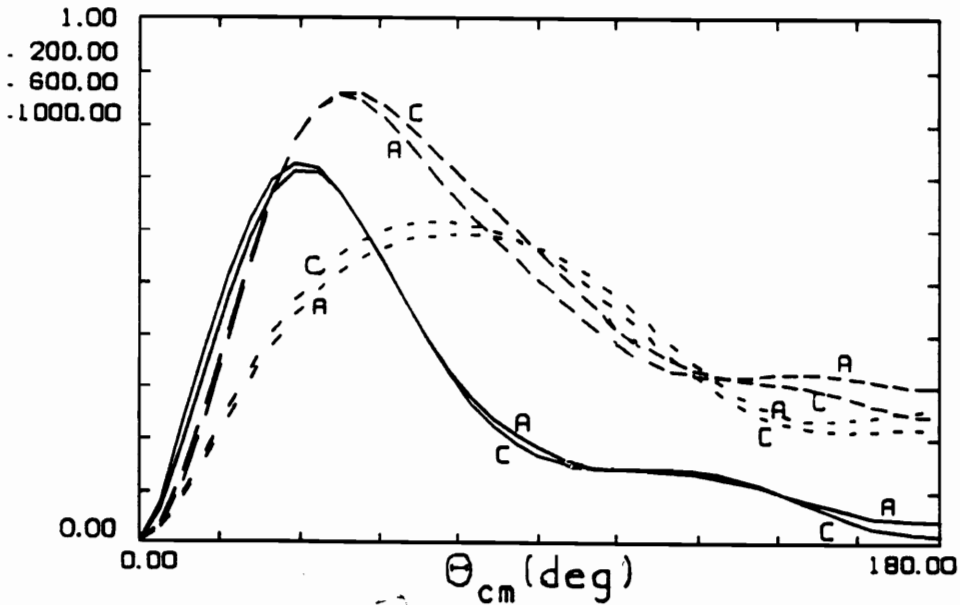


Figure 6-52: $\sigma(\theta)$ of $K_L^0 p \rightarrow K^+n$ for solutions A and C. The solid line indicates $T_{lab} = 1000$ MeV; the longer dash in the dashed line indicates the higher energy.

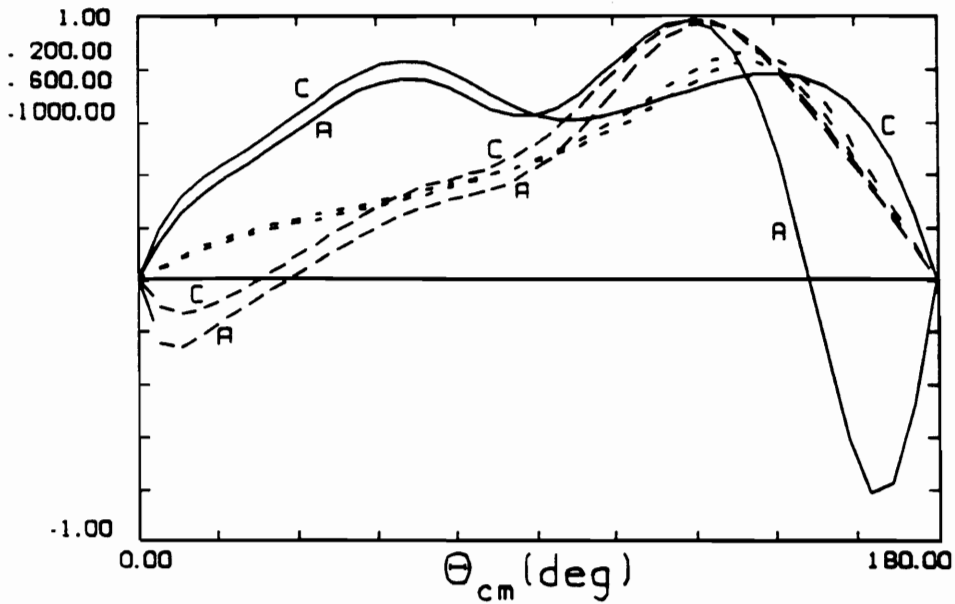


Figure 6-53: $P(\theta)$ of $K^+n \rightarrow K^0p$ for solutions A and C. The solid line indicates $T_{lab} = 1000$ MeV; the longer dash in the dashed line indicates the higher energy.

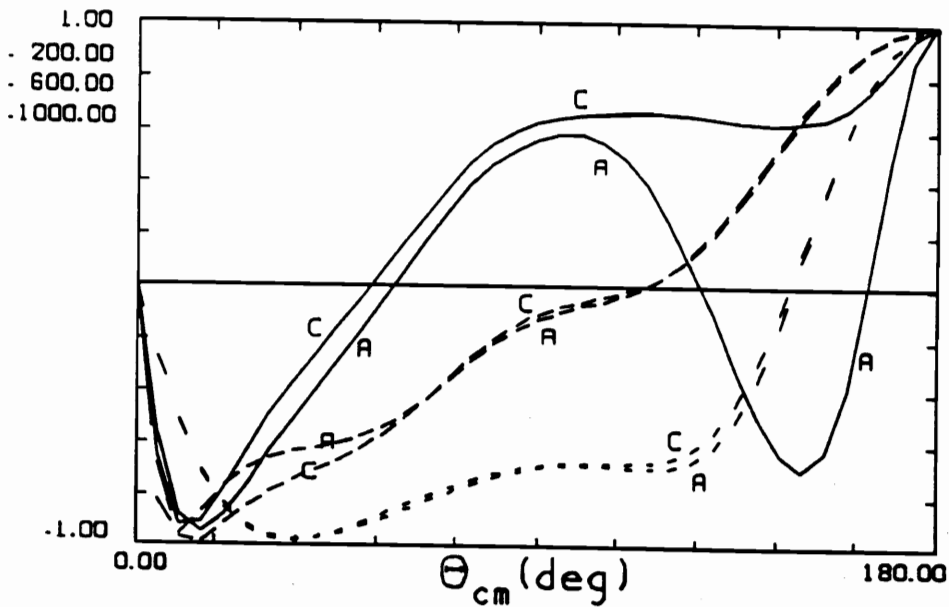


Figure 6-54: $R(\theta)$ of $K^+n \rightarrow K^0p$ for solutions A and C. The solid line indicates $T_{lab} = 1000$ MeV; the longer dash in the dashed line indicates the higher energy.

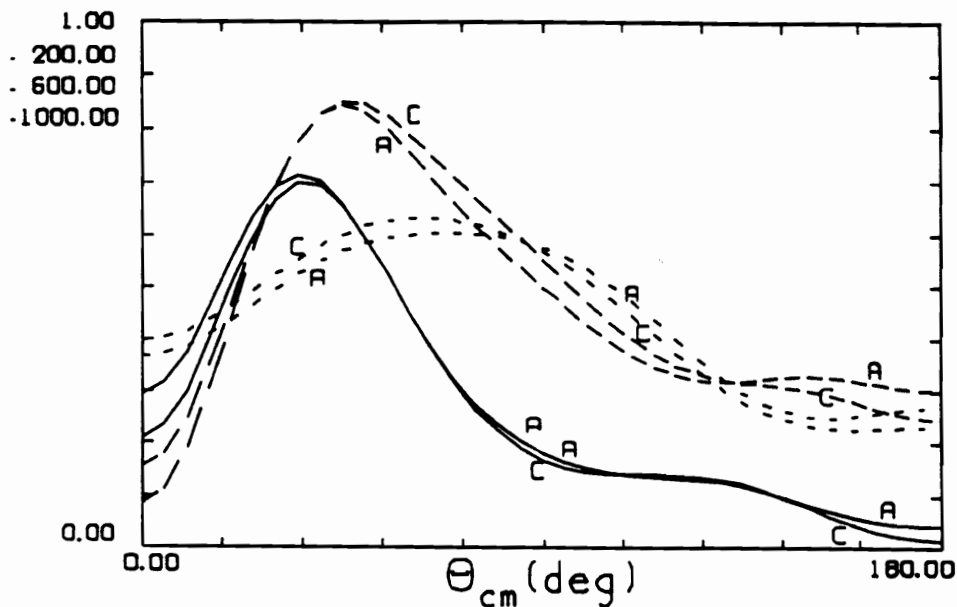


Figure 6-55: $\sigma(\theta)$ of $K^+d \rightarrow K^0pp$ with no momentum cuts for solutions A and C. The solid line indicates $T_{lab} = 1000$ MeV; the longer dash in the dashed line indicates the higher energy.

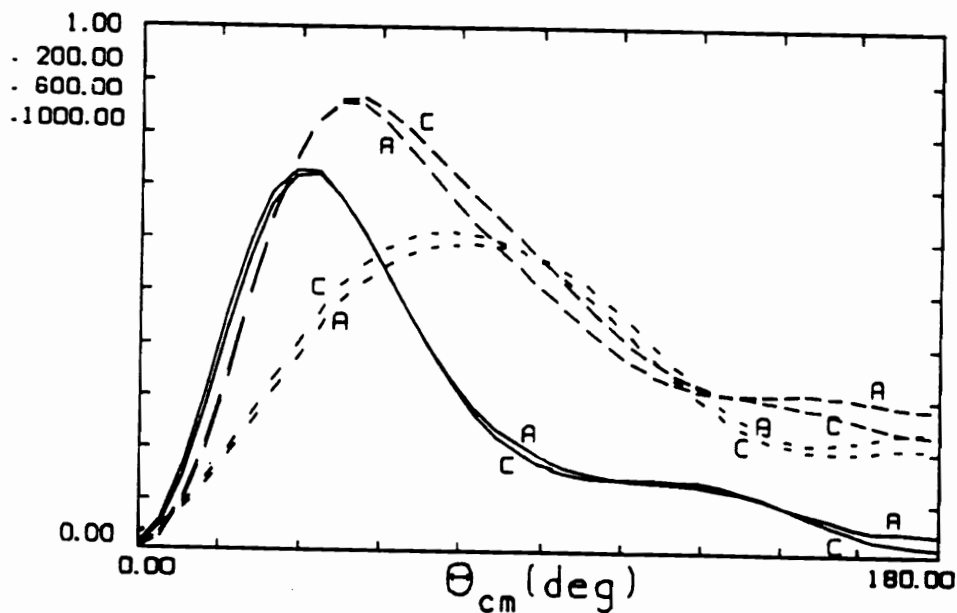


Figure 6-56: $\sigma(\theta)$ of $K^+d \rightarrow K^0p(p)$ with momentum cuts of 100 and 250 MeV/c for solutions A and C. The solid line indicates $T_{lab} = 1000$ MeV; the longer dash in the dashed line indicates the higher energy.

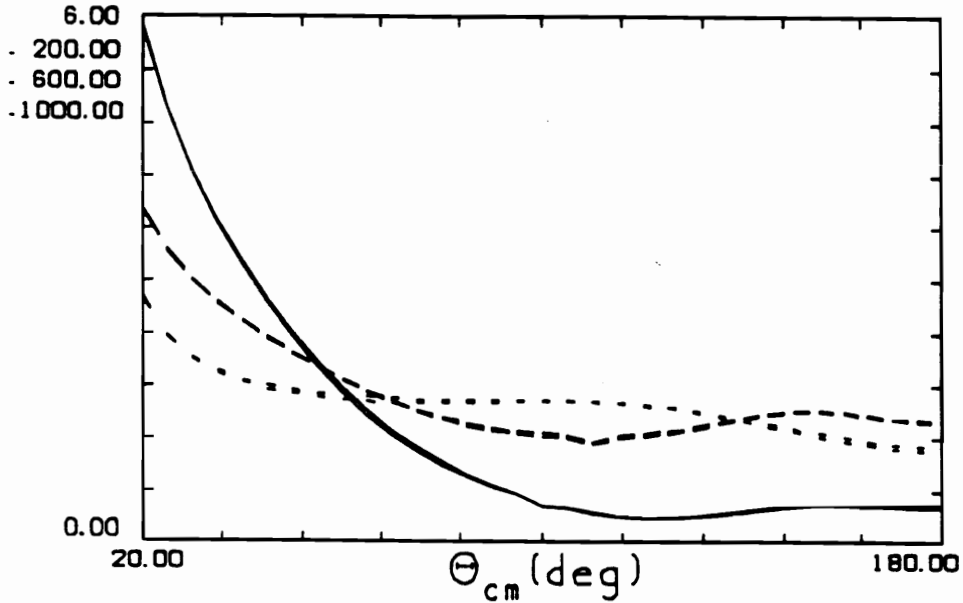


Figure 6-57: $\sigma(\theta)$ of $K^+d \rightarrow K^+np$ with no momentum cuts for solutions A and C. The solid line indicates $T_{lab} = 1000$ MeV; the longer dash in the dashed line indicates the higher energy.

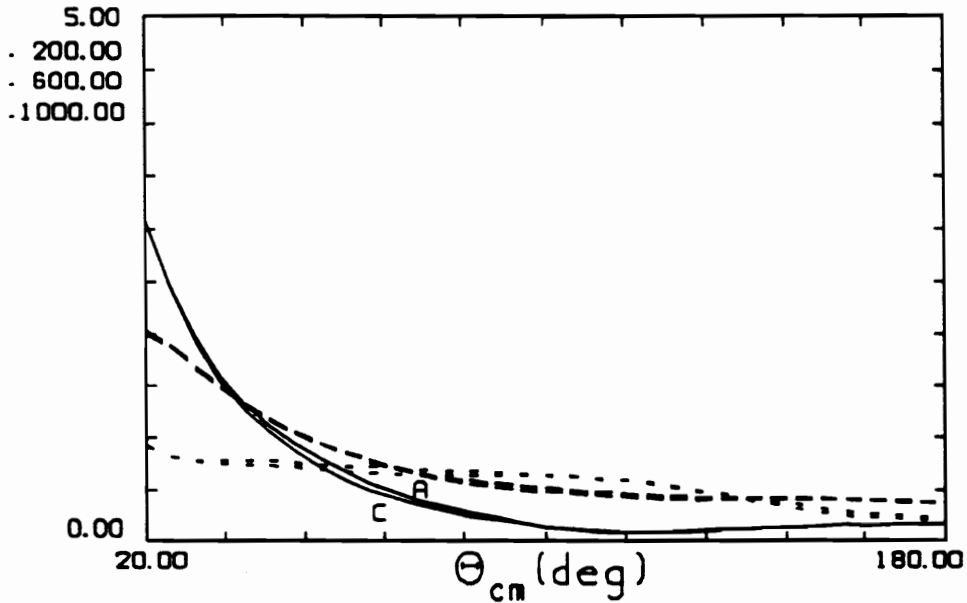


Figure 6-58: $\sigma(\theta)$ of $K^+d \rightarrow K^+n(p)$ with momentum cuts of 100 and 250 MeV/c for solutions A and C. The solid line indicates $T_{lab} = 1000$ MeV; the longer dash in the dashed line indicates the higher energy.

Chapter 7

Conclusions and Recommendations

7.1 Conclusions

The isoscalar states in the K^+N scattering reaction follow a trend. The $l=j+\frac{1}{2}$ states produce an attractive potential effect and the $l=j-\frac{1}{2}$ a repulsive potential effect. Broad motion in the counterclockwise direction is recorded in the P_{01} , D_{03} , and P_{13} argand diagrams. Resonance poles are found for each of these partial-waves. In addition, resonance poles are found in the P_{11} and D_{15} states, which corresponds to the tighter counterclockwise motion in those argand diagrams.

Theories produce mass values for resonance poles. Yet, of these theories, only one [deS80] predicts resonance poles for an orbital angular momentum greater than zero, and it predicts pole masses different from the real part of the pole positions in this analysis. The theory also predicts resonance poles in the S_{01} , S_{11} , P_{03} , D_{13} , and F_{15} . Therefore, the prediction of the theory as a whole comes into question. The analysis by Nakajima et al. [Na82] also produces

broad counterclockwise motion in the P_{01} , D_{03} , and P_{13} waves. Yet, the masses which he determines from a Breit-Wigner fit with a smooth background must be extracted to the pole positions. The scattering lengths of the theories and this analysis differ. The S-wave scattering lengths are all relatively close except for those of the Lagrangian I [Coh89] and Lagrangian II(σ) [BH85] techniques. For the P-wave scattering lengths, a larger deviation is observed between the other predictions and those of this analysis.

7.2 Recommendations

More data contributing to the isoscalar partial-waves need to be measured. As evident from the data distributions, large kinematic regions are unrepresented. Most noticeable is the lack of polarization of both $K^+n \rightarrow K^+n$ and $K^+n \rightarrow K^0p$ reactions. In Figures 6-50 and 6-53 for $K^+n \rightarrow K^+n$ and $K^+n \rightarrow K^0p$ respectively, it is shown that the polarization from solutions A and C disagree considerably at the highest lab energy of 1000 MeV and at angles away from forward scattering. In Figure 6-50 a difference of 0.3 or greater exists in the c.m. angle of 120-160°. The maximum deviation is 0.8 at nearly 135°. In Figure 6-53 this difference exists between 145° and 175° and has a maximum of 1.4 at 165°.

No data exist for $R(\theta)$, and as shown in Figures 6-51 and 6-54 for $K^+n \rightarrow K^+n$ and $K^+n \rightarrow K^0p$ respectively, the disagreement for these observables at 1000 MeV in solutions A and C are large also. For example, from 100° to 125° for $K^+n \rightarrow K^+n$ and from 120° to 170° for $K^+n \rightarrow K^0p$ a difference of 0.3 or greater exists. The maximum difference for $K^+n \rightarrow K^+n$ is nearly 0.7 at approximately 120° and for $K^+n \rightarrow K^0p$ it is 1.35 at 150°.

Much more data have been measured for the differential cross sections. As shown in Figures 6-49, 6-55, and 6-56-6-58, the solutions for these observables agree much more closely. In all but $K^+d \rightarrow K^+np$ the maximum deviation in the two solutions occurs at 600 MeV. For $K^+d \rightarrow K^+np$ the maximum occurs at 1000 MeV. In Figure 6-52 for $K_L^0p \rightarrow K^+n$ $\sigma(\theta)$ a difference of 0.04 mb exists in the angular region of 65° to 100° and 160° to 180°. In

Figure 6-55 for $K^+d \rightarrow K^0pp$ the angular range of 65° to 105° and 160° to 180° also shows this difference. Figure 6-58 for $K^+d \rightarrow K^+n(p)$ shows a difference of 0.06 mb within 45° to 60° . A difference of 0.04 exists from 30° to 75° .

Measurements which would exploit these deviations in addition to other differences shown in Figures 6-49-6-58 would distinguish between solutions A and C, as well as better define the final solution.

Bibliography

- [AB69] G. Alberi and C. Bertocchi, *Nuovo Cimento* 58A, 285 (1969).
- [AI72] G. Alberi et al., Istituto Nazionale di Fisica Nucleare Report INFN/AE-72/3, 1972 (unpublished).
- [AF85] R.A. Arndt, J.M. Ford and L.D. Roper, *Phys. Rev.* D32, 1085 (1985).
- [AM66] R.A. Arndt and M.H. MacGregor in *Methods in Computational Physics*, (Ed. by B. Alder) Vol. 6, p.253-295, Academic Press, New York, 1966.
- [AR85] R.A. Arndt and L.D. Roper, *Phys. Rev.* D31, 2230 (1985).
- [BC67] C. Bertocchi and A. Capella, *Nuovo Cimento* 51A, 369 (1967).
- [BH85] R. Büttgen, K. Holinde, and J. Speth, *Phys. Lett.* 163B, 305 (1985).
- [BH89] R. Büttgen, K. Holinde, and J. Speth, *Nuovo Cimento* 102, 247 (1989).
- [Co82] M.J. Cordon et al., *Phys. Rev.* D25, 720 (1982).
- [Coh89] Joseph Cohen, *Phys. Rev.* C39, 2285 (1989).
- [Cu76] R.E. Cutkosky et al., *Nucl. Phys.* B102, 139 (1976).
- [deS80] J.J. deSwart, P.J. Mulders and L.J. Somers, in *Baryon 1980*, Proceedings of the IVth International Conference of Baryon Resonances, Toronto, edited by N. Isgur (University of Toronto Press, Toronto, 1981)

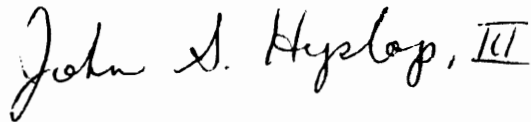
- [DeG75] T. DeGrand, R.L. Jaffe, K. Johnson and J. Kiskis, Phys. Rev. D12, 2060 (1975).
- [DW82] Carl B. Dover and George E. Walker, Phys. Rep. 89, 1 (1982).
- [FT80] B.J. Edwards and G.H. Thomas, Phys. Rev. D22, 2772 (1980); J.L. Basdevant and E.L. Berger, Phys. Rev. D19, 239 (1979).
- [Fe59] E.M. Ferreira, Phys. Rev. 115, 1727 (1959).
- [Fo88] John M. Ford, Ph.D. dissertation, Department of Physics, Virginia Tech (1988).
- [Ga88] H. Garcilazo, Phys. Rev C37, 2022 (1988).
- [Hag63] R. Hagedorn, *Relativistic Kinematics* (W.A. Benjamin, Inc., New York, 1963), pp.61, 65-67.
- [Ha83] K. Hashimoto, Phys. Rev. C27, 1572 (1983).
- [Had83] K. Hashimoto, dissertation, Department of Nuclear Engineering, Kyoto University, Japan (1983).
- [Ha84] K. Hashimoto, Phys. Rev. C29, 1377 (1984).
- [HK79] G. Höhler, F. Kaiser, R. Koch and E. Pietarinen, *Handbook of Pion-Nucleon Scattering* (Fachinformation-Szentrum, Karlsruhe, Germany) *Physics Data*, Vol. 12-1, 1979.
- [JL79] R.L. Jaffe and F.E. Low, Phys. Rev. D19, 2105 (1979).
- [Lo88] Earle L. Lomon, at the 8th International Symposium on High Energy Spin Physics, University of Minnesota, September 1988.
- [Ma76] A.D. Martin, Phys. Lett. 65B, 346 (1976).
- [Me70] E. Merzbacher, *Quantum Mechanics*, Wiley, 1970, pp. 245-249.

- [MO80] B.R. Martin and G.C. Oades, in *Baryon 1980, Proceedings of the IVth International Conference of Baryon Resonances*, Toronto, edited by N. Isgur (University of Toronto Press, Toronto, 1981).
- [Na82] K. Nakajima et al., *Phys. Lett.* **112B**, 80 (1982).
- [PB75] M.A. Preston and R.K. Bharduri, *Structure of the Nucleus*, Addison-Wesley Publishing Co., 1975, pp. 639-742.
- [Ro79] C. Roiesnol, *Phys. Rev.* **D20**, 1646 (1979).
- [Sn89] G. Snow, Private Communication.
- [ZA80] V.S. Zidell, R.A. Arndt and L.D. Roper, *Phys. Rev.* **D21**, 1225 (1980).
- [61S2] W. Slater et al., *Phys. Rev. Lett.* **7**, 378 (1961).
- [64S1] V.J. Stenger et al., *Phys. Rev.* **134B**, 1111 (1964).
- [69R1] A.K. Ray et al., *Phys. Rev.* **183**, 1183 (1969).
- [70A1] R.J. Abrams et al., *Phys. Rev.* **D1**, 1917 (1970).
- [70C1] R.L. Cool et al., *Phys. Rev.* **D1**, 1887 (1970).
- [71B2] A.A. Hiratta et al., *Nucl. Phys.* **B33**, 525 (1971).
- [71H1] A.A. Hirata et al., *Nucl. Phys.* **B30**, 157 (1971).
- [71M1] G.W. Meisner and F.S. Crawford, *Phys. Rev.* **D3**, 2553 (1971).
- [72G1] G. Giacomelli et al., *Nucl. Phys.* **B37**, 577 (1972).
- [72G2] G. Giacomelli et al., *Nucl. Phys.* **B42**, 437 (1972).
- [73B5] P. Lugaesi-Serra et al., *Istituto Nazionale di Fisica Nucleare preprint*, INFN/AE-73/9 (1973), unpublished.

- [73C1] A.S. Carroll et al., Phys. Lett. 45B, 531 (1973).
- [73G1] G. Giacomelli et al., Nucl. Phys. B56, 346 (1973).
- [73G2] G. Giacomelli et al., Istituto Nazionale di Fisica Nucleare preprint, INFN/AE-73/4 (1973), unpublished.
- [74G1] G. Giacomelli et al., Nucl. Phys. B68, 285 (1974).
- [75A2] U. Adams et al., Nucl. Phys. B87, 41 (1975).
- [75D1] C.J.S. Damerell et al., Nucl. Phys. B94, 374 (1975).
- [75M1] B.R. Martin, Nucl. Phys. B94, 413 (1975).
- [75S1] M. Sakitt, J. Skelly, J.A. Thompson, Phys. Rev. D12, 3386 (1975).
- [76E2] R.M. Edelstein et al., Phys. Rev. D14, 702 (1976).
- [77A1] J.C.M. Armitage et al., Nucl. Phys. B123, 11 (1977).
- [77G1] R.G. Glasser et al., Phys. Rev. D15, 1200 (1977).
- [77S1] M. Sakitt, J. Skelly, and J. Thompson, Phys. Rev. D15, 1846 (1977).
- [80R1] A.W. Robertson et al., Phys. Lett. 91B, 465 (1980).
- [80W1] S.J. Watts et al., Phys. Lett. 95B, 323 (1980).
- [82K1] K. Nakajima et al., Phys. Lett. 112B, 75 (1982).

Vita

- **Name:** John S. Hyslop, III



- **Date of Birth:** June 17, 1957

- **Education**

- ▷ **Ph.D. Physics** 1990, Virginia Polytechnic Institute and State University, Blacksburg, Virginia.
- ▷ **M.S. Physics** 1984, Virginia Polytechnic Institute and State University, Blacksburg, Virginia.
- ▷ **Coursework in M.S.E.E. program** 1980, Georgia Institute of Technology, Atlanta, Georgia.
- ▷ **B.S. Dual major: Physics and Physics-Engineering** 1979
Washington and Lee University, Lexington, Virginia.

- **Work Experience**

- ▷ **Aerospace Engineer**, Sounding Rocket Division, Goddard Space Flight Center / Wallops Flight Center, NASA, Wallops Island Virginia, 12/80 - 9/82.

- **Talks and Publications**

- ▷ *An Analysis of K^+N Scattering*, invited talk given at the International Conference of Particles and Nuclei (PANIC XII), Massachusetts Institute of Technology, Cambridge, Massachusetts, June 1990.
- ▷ *Isoscalar Characteristics of the K^+N Scattering System to 1100 MeV*, paper contributed to the International Conference of Particles and Nuclei (PANIC XII), J.S. Hyslop, R.A. Arndt and L.D. Roper, Massachusetts Institute of Technology, Cambridge, Massachusetts, June 1990.
- ▷ *Nucleon-Nucleon Partial Wave Analysis to 1100 MeV*, R.A. Arndt, J.S. Hyslop and L.D. Roper, Physical Review D35, 128 (1987).

- **Honors**

- ▷ Selected for Professional Internship Program at NASA GSFC/WFF
- ▷ Member of $\Sigma\Pi\Sigma$, physics honor society